3DP

A control system model for combined DP station keeping and active roll reduction

R.G. de Jong

Technische Universiteit Delft

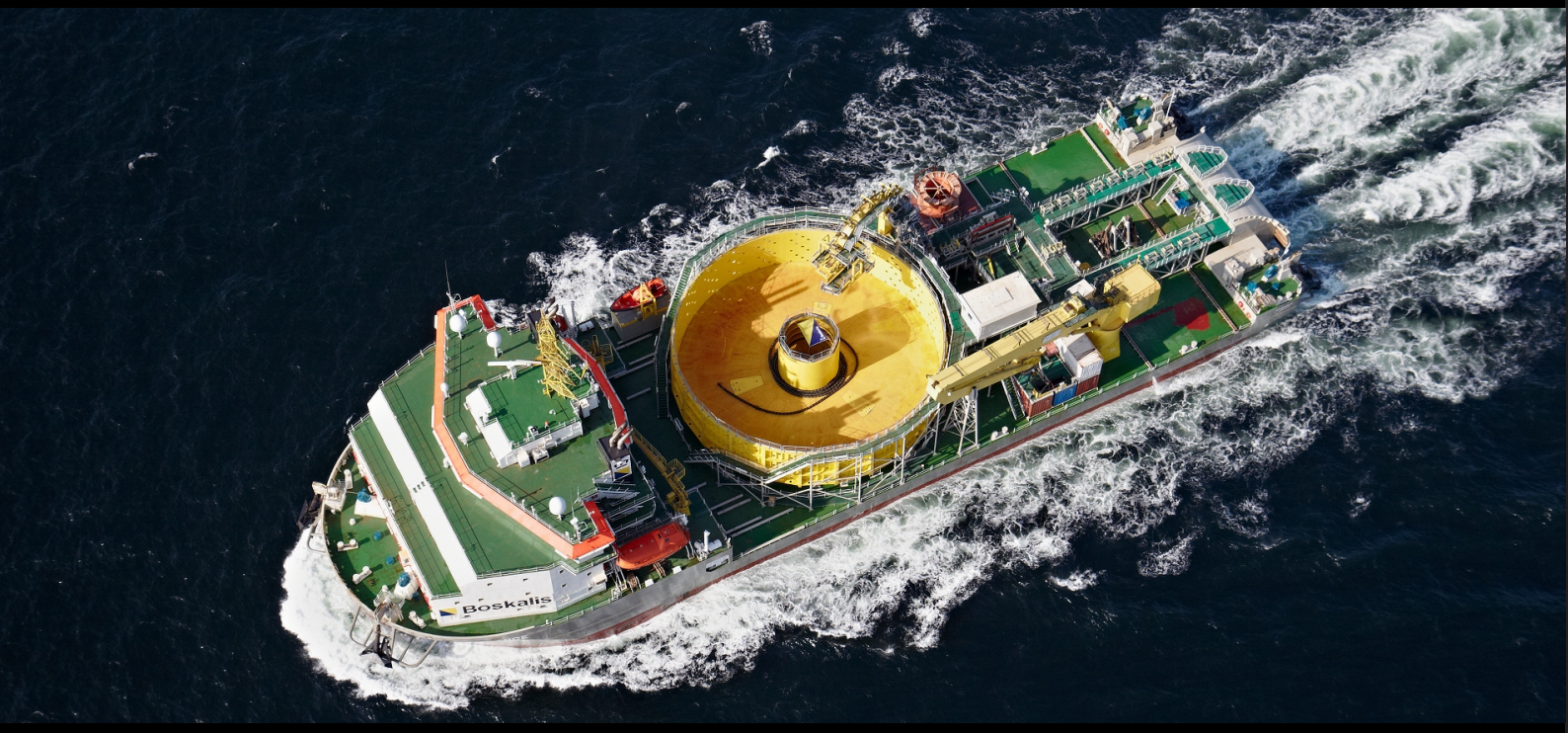

TU Delft

Boskalis

3DP

A control system model for combined DP station keeping and active roll reduction

by

R.G. de Jong

to obtain the degree of Master of Science
at the Delft University of Technology,
to be defended publicly on Thursday July 5, 2018 at 14.00

Student number: 4195647
Project duration: October 2, 2017 – 5 July 2018
Thesis committee:

Prof. dr. ir. A. P. van 't Veer,	TU Delft, chair
Dr. ir. P. R. Wellens,	TU Delft, daily supervisor
Prof. dr. ir. J. W. van Wingerden,	TU Delft
Dr. ir. M. Godjevac,	TU Delft
Ir. T. G. Vos,	Boskalis
Ir. R. Beindorff,	Boskalis

TU Delft

Preface

This thesis is the final deliverable in my pursuit of a master's degree in Ship Hydromechanics at Delft University of Technology. During the thesis research, I tried to develop a control system that enables a ship to reduce its roll motion during Dynamic Positioning operations. The research combined my interest in ship motions, thrusters and control systems. I enjoyed working on it for the past 8 months and I am happy with the end result. I could not have done it without the help and support of several people and I would like to thank them for their contributions.

First of all, I would like to thank Thijs Vos and Ruud Beindorff for their unrelenting enthusiasm, support and for giving me the freedom to conduct the research according my own ideas.

Furthermore, Peter Wellens and Helio Bailly Guimaraes, thanks for teaching and inspiring me during the final years of my education. You somehow always succeeded in feeding my curiosity and enthusiasm.

Last but not least, I would like to thank my family, Barbara, my friends and in particular Roel and Casper for the good times both offshore and onshore.

R.G. de Jong
Papendrecht, June 2018

Abstract

During DP operations in beam seas, the cable-lay vessel *Ndurance* experiences significant roll motions that decrease the operability. This research aims to evaluate the possibility of reducing the ship roll motion during DP operations by active control of the thrusters.

A vessel time domain model is constructed based on Cummins' equation. The convolution term is evaluated by using a state-space representation. Since no viscous effects are included when diffraction analysis is used, the viscous roll damping due to eddy making and skin friction are calculated in the frequency domain by using empirical models. The viscous roll damping term in the time domain model is subsequently determined by tuning a quadratic roll velocity coefficient in the time domain model until the roll RAO matches the frequency domain roll RAO with viscous damping included.

A dynamic thruster model has been applied to the thrusters installed at the *Ndurance*. An empirical estimate of the added rotational inertia of the entrained water in the thruster has been included for conservatism. To include the effect of both negative and positive thruster inflow velocities, a four-quadrant model has been used to calculate the thrust and torque characteristics of the thrusters.

A DP system model has been constructed consisting out of a Kalman filter, PID controller and a thrust allocation algorithm. The DP system model is merged with the vessel time domain model and is subsequently subjected to first- and second-order wave forces, current forces and wind forces. The model results are compared to time domain DP simulations conducted by MARIN.

In order to achieve combined DP station keeping and active roll reduction a new control model is developed. The model is referred to as 3DP (3-dimensional DP). The control system model is based on a hierarchical controller structure, consisting of high-level motion controllers and low-level azimuth angle and shaft speed controllers. The high-level motion controller consists out of a combination of a roll controller and a conventional DP controller. Both controller commands are merged by application of proposed allocation matrices. The merged controller commands are subsequently used as setpoint for the low-level shaft speed controller. The azimuth angle of the thrusters used to counteract the environmental loads in the surge direction is controlled by a proportional controller. The azimuth angle controller is implemented to achieve both maximum roll reduction and sufficient station keeping ability.

Multiple simulations have been carried out with both the DP and the 3DP control model. From the results of these simulations can be concluded that the proposed 3DP control model enables the possibility of thruster induced roll reduction. The maximum roll reduction is achieved during sea states with low to moderate significant wave heights and wave periods in the natural frequency range. During these conditions, the roll reduction is around 0.5° roll RMS. From this result is concluded that the 3DP model is able to decrease the roll motion to a significant extent. The effect of thruster induced roll reduction onto the station keeping performance of the ship is also investigated. From these results can be concluded that the DP footprint of the vessel increases with a maximum of 1 meter when the 3DP model is applied. The DP station keeping capability results showed that the vessel is limited to a beam current velocity of 0.9 m/s. The power consumption of the thrusters is calculated according the simulation results. It is concluded that the 3DP control system consumes roughly 10 times more power than the conventional DP system. Also, the workability increase has been calculated when the 3DP model is used. For beam waves this resulted in a yearly workability increase of 5.2%. The workability increase averaged over every environmental direction is 2.0%.

It is recommended that the 3DP control model is used as a back-up instrument to reduce the roll motion of the vessel during critical offshore operations, like tool over-boardings or cable pull-ins. In this way, the operational use of the system is limited to short periods of time and the wear and tear and increased fuel consumption of the thrusters is of minimal nature.

Nomenclature

COG - Centre of Gravity

DOF - Degrees of Freedom

DP - Dynamic Positioning

IRF - Impulse Response Function

QTF - Quadratic Transfer Function

RAO - Response Amplitude Operator

RMS - Root Mean Square

RPM - Rounds Per Minute

RRR - Relative Roll Reduction

SS - State-Space

TF - Transfer Function

VFD - Variable Frequency Drive

WD - Water Depth

List of Symbols

Greek Symbols

η	vessel motion vector	[m] or [rad]
η_{RMS}	root mean square values of motion vector	[m] or [rad]
ϵ	phase angle	[rad]
ϕ	roll amplitude	[rad] or [deg]
ψ	yaw amplitude	[rad] or [deg]
θ	pitch amplitude	[rad] or [deg]
ω	wave frequency or propeller angular velocity	[rad/s]
ω_N	cut-off wave frequency	[rad/s]
κ	state-space convolution representation	[-]
ξ	wave amplitude	[m]
τ	motion controller command	[RPM]
τ_ϕ	roll controller command	[RPM]
τ_{DP}	DP controller command	[RPM]
τ_{azi}	azimuth controller command	[deg]
τ_s	shaft speed controller command	[Nm]
β	hydrodynamic pitch angle	[deg]
μ	environmental direction	[deg]
ρ	sea water density	[kg/m^3]
ρ_a	air density	[kg/m^3]

Roman Symbols

$\mathbf{A}_\infty$	infinite frequency added mass matrix	[kg] or [kgm^2]
$\mathbf{A}_{ss}$	state-space system matrix	[-]
$\mathbf{A}(\omega)$	hydrodynamic added mass matrix	[kg] or [kgm^2]
A_L	lateral wind area	[m^2]
A_T	frontal wind area	[m^2]
b	required forces and moments in the horizontal plane	[kN] or [kNm]
$\mathbf{B}_{ss}$	state-space input matrix	[-]
$\mathbf{B}(\omega)$	hydrodynamic damping matrix	[kg/s] or [kgm^2/s]
B_{bk}	bilge keel roll damping coefficient	[kgm/s rad]
B_e	eddy making roll damping coefficient	[kgm/s rad]
B_{eq}	equivalent roll damping coefficient	[kgm/s rad]
B_f	skin friction roll damping coefficient	[kgm/s rad]
B_L	lift roll damping coefficient	[kgm/s rad]
B_N	hydrodynamic damping at the cut-off frequency	[kgm/s rad]
B_{visc}	quadratic viscous roll damping term	[kgm/s rad]
B_w	wave making roll damping	[kgm/s rad]
$\mathbf{C}$	ship hydrostatic stiffness matrix	[N/m] or [Nm/rad]
$\mathbf{C}_{ss}$	state-space output matrix	[-]
$c(x)$	non-linear constraints vector	[kN]
$C(\mu)$	wind/current load coefficient	[-]
c_1	viscous quadratic damping tuning parameter	[-]
C_{IE}	entrained water fitting parameter	[-]
C_Q	four-quadrant torque coefficient	[-]

C_T	four-quadrant thrust coefficient	[-]
D	propeller diameter	[m]
e	setpoint error	[m] or [deg]
EAR	propeller expanded area ratio	[-]
$\mathbf{F}(\omega)$	first-order wave excitation force amplitude vector	[N] or [Nm]
$F_0(\mathrm{x})$	thrust allocation objective function	[-]
H_s	significant wave height	[m]
I_E	added rotational inertia of entrained water in propeller	[kg m^2]
I_p	propeller rotational inertia	[kg m^2]
I_{ps}	propeller shaft rotational inertia	[kg m^2]
I_r	rotor rotational inertia	[kg m^2]
I_s	total thruster system rotational inertia	[kg m^2]
K	empirical coefficient entrained water added rotational inertia	[-]
K_p	proportional controller coefficient	[-]
K_i	integral controller coefficient	[-]
K_d	derivative controller coefficient	[-]
k_g	gearbox ratio	[-]
L_{pp}	vessel length between perpendiculars	[m]
$\mathbf{M}$	ship inertia matrix	[kg] or [kgm^2]
N	total number of frequencies	[-]
N_t	total number of thrusters	[-]
P/D	propeller pitch-diameter ratio	[-]
Q_{cm}	commanded motor torque	[Nm]
Q_m	motor torque	[Nm]
Q_p	propeller torque	[Nm]
Q_{cm}	commanded motor torque	[Nm]
R_{max}	maximum DP excursion in the horizontal plane	[m] or [deg]
$S_\eta(\omega)$	motion response spectrum	[m^{2}s] or [rad^{2}s]
$S_\xi(\omega)$	wave spectrum	[m^{2}s]
t	time vector	[s]
T	vessel draft	[m]
T_c	cut-off scaling time constant	[-]
T_m	thruster time constant	[s]
T_{max}	maximum thrust magnitude	[kN]
T_p	wave peak period	[s]
v_a	propeller advance velocity	[m/s]
W_{3DP}	workability when 3DP system is engaged	[%]
W_{DP}	workability when DP system is engaged	[%]
W_{inc}	workability increase	[%]
x	vessel surge displacement	[m]
y	vessel sway displacement	[m]
y_{max}	maximum value in model result range	[-]
y_{min}	minimum value in model result range	[-]
z	vessel heave displacement	[m]
Z	number of propeller blades	[-]

Contents

1 Introduction

1.1. Background

The results of the UN Paris climate agreement in 2015 and the globally increasing environmental awareness among people, made the need for clean and sustainable energy bigger then ever before. As a consequence, the offshore wind industry has been rapidly expanding. The annual European offshore wind turbine installations rose from 318.4 MW to 3018 MW between the years 2007 and 2015 [26].
Offshore contractors are hired to install these wind turbines. They are involved in the offshore construction of, for example, foundations, monopiles, subsea power cables and transformer platforms. To carry out these construction activities, a range of ships is used. These ships are all subjected to the wind, waves and current present in the offshore environment. To enable safe and economical ship operation, it is important to be able to predict the ship motion response to the environmental forces present. Even more important would be the ability to actively control the ship motion response during offshore operations. This enables the ship to operate more safely and economically.

Active ship motion control started in 1961 with the world's first automatically controlled dynamically positioned (DP) drillship *Eureka*, operated by Shell [20]. The *Eureka* was equipped with two thrusters to control its position in the horizontal plane. It was a very successful ship. The *Eureka* drilled 9 cores a day up to 150 meters in the sea floor at water depths up to 1200 meter, where comparably sized anchored ships were able to do this in 2 to 4 days at a limited water depth of 100 meter.
Since the introduction of the *Eureka*, dynamically positioned ships became the standard for offshore construction ships. Not only in the oil and gas sector, but also in the offshore renewable industry. Nowadays, numerous FPSOs, cable-laying, pipe-laying, heavy-lift and offshore supply ships are equipped with a DP system to actively control the horizontal motions.

DP systems are currently used to control motions in the horizontal plane only. However, the safety and operability of several offshore operations, like helicopter landings and lifting operations, can be increased when also motions in the vertical plane can be controlled. A recent study conducted by Rudaa [28] at NTNU showed that it is also possible to use the thrusters of the DP system to reduce the roll motion of a ship.

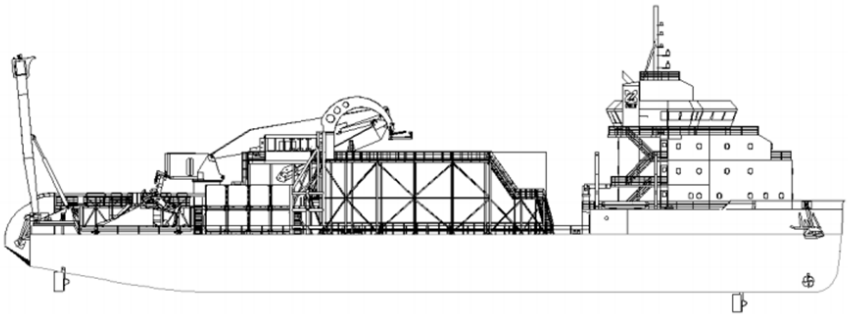

Figure 1.1: Schematic visualization of the *Ndurance*

1.2. Problem statement

The *Ndurance* is a DP offshore construction vessel operated by Boskalis. The vessel is currently used for laying, connecting and repairing subsea power cables, rock bag installation, survey and mass flow excavation operations. A visualization of the *Ndurance* is given in Figure 1.1. The vessel experiences significant roll motions during beam waves in the natural frequency range. Several offshore DP operations require a fixed heading and therefore the vessel is not always able to avoid beam waves by weathervaning. The roll response during these circumstances can be so significant that it prevents the crew from safely operating the equipment on deck, forcing the ship to wait for more advantageous weather conditions. This phenomena is reducing the operability of the vessel.

To increase the operability of the vessel, the roll motion needs to be reduced. This can possibly be achieved by using the thrusters of the installed DP system. Since the COG of the vessel is located above the thrusters, the produced thrust results in a roll moment which can be used to counteract the wave induced roll moment. Thruster controlled roll reduction is possible as concluded from mathematical and experimental model tests conducted at NTNU. However, the effect of active roll reduction on the station keeping performance of the ship has not been investigated, since the available thrust is fully used for roll reduction purposes. Also, the application of thruster induced roll reduction has only been evaluated for an offshore supply vessel, which hull shape and DP system significantly differs from the cable-lay vessel *Ndurance*.

1.3. Research objective

The main objective is to evaluate whether it is possible to reduce the significant roll amplitude of the *Ndurance* in beam seas during DP operations by active control of the thrusters. To be able to achieve the main objective, a merged mathematical ship, thruster and control system model with 3-dimensional motion control capability has to be constructed (3DP). With this model it is also possible to evaluate the effect of active roll reduction onto the station keeping performance of the ship. Recommendations regarding possible thruster alternatives, ship lay-out and DP configuration that influence the possibility and magnitude of actively controlled roll reduction are given. The sub-research objectives are formulated as:

1. Develop a 6 DOF ship model in the time domain that captures the ship response to environmental forces and validate this model with frequency domain data.
2. Develop a thruster model that captures the thruster dynamics in the time domain, this will include modeling of the thruster drive train system and thrust variations due to oscillating inflow velocities.
3. Develop a simulation model that is able to simulate DP system behavior, this includes modelling of the DP system and environmental forces.
4. Develop a control system model that enables combined DP station keeping and active roll reduction.
5. Identify and quantify the possibility and magnitude of thruster induced roll reduction and its effect on the station keeping performance of the ship.
6. Give recommendations regarding possible thruster alternatives, the ship lay-out and DP system configuration that influence the possibility and magnitude of actively controlled roll reduction.

The report is structured in such a way that the results of every sub-research objective will be presented in the conclusions of the dedicated chapter.

1.4. Research approach

First, the ship is mathematically modeled in the time domain in 6 DOF, according to the damping and added mass as calculated by diffraction analysis. The time domain model results are compared to frequency domain model results to verify that the implementation is correct. This is done by comparison of the motion amplitude results when both models are subjected to regular harmonic waves. Subsequently, a viscous roll damping model is implemented in both the frequency and time domain model to include viscous effects not captured by diffraction analysis.

Secondly, the thruster behavior in the time domain is modeled. Since the thrusters of the *Ndurance* are fixed pitch propellers, the produced thrust is directly linked to the RPM of the electrical motor driving the thrusters. To model the thruster response to control inputs and to capture the ramp-up and ramp-down of the thrusters, a dynamic thruster model is constructed which includes the total thruster system inertia. Next, the influence of oscillating inflow velocities, due to the roll velocity of the ship, on the produced thrust and torque are captured by using the four-quadrant method.

Thirdly, the mathematical models of the thrusters and the ship are merged and the environmental forces induced by wind, waves and current are generated in the time domain. Also, a control model is implemented for station keeping (DP). This model enables the simulation of the 6 DOF ship motions during DP operations. The model is verified with MARIN data.

Fourthly, a new control model system is proposed that combines anti-roll control and station keeping control. This model is used to evaluate the possible roll reduction and the impact of the roll control mode onto the DP footprint, station keeping capability, power consumption and workability.

Finally, the results of the simulations are analyzed by comparing the root mean square values of the roll amplitudes with and without active roll control. Also, the DP footprint, DP capability, thruster power consumption and vessel workability is evaluated for different environmental conditions. According the results, recommendations will be given regarding the influence of different ship parameters on the possibility and magnitude of thruster induced roll reduction.

1.5. Report structure

The report structure is shortly summarized in the enumeration below.

- In Chapter 2 (**Ship Model**), models to calculate a ship's motion response are presented and reviewed. A time domain ship model is constructed and verified.
- In Chapter 3 (**Thruster Model**), a dynamic thruster model is presented and implemented. Also, the thruster behavior in oscillating flow is included in the dynamic model. The results are verified with manufacturer data and expert indication
- In Chapter 4 (**DP System Model**), the DP control system simulation model is developed. The results are verified with time domain test data.
- In Chapter 5 (**3DP System Model)**, the anti-roll controller is introduced and merged with the DP system to obtain a new simulation model for roll reduction and station keeping combined. This system is called 3DP.
- In Chapter 6 (**Results**), the results of the 3DP system model regarding the achieved roll reduction are evaluated. Also, the DP footprint, DP capability, thruster power consumption and workability of the 3DP model is evaluated and compared to the performance of the conventional DP system model.
- In Chapter 7 (**Conclusions and Recommendations**), conclusions and recommendations are given regarding the model results and the conducted research.

2
Ship Model

In order to evaluate the possibility and magnitude of thruster induced roll reduction and its effect on the DP footprint of the *Ndurance*, it is important to construct a model that is able to calculate the 6 DOF ship motion response, resulting from environmental and thruster loads. The method and models to estimate and simulate ship motions are presented in this chapter.

2.1. Introduction

In literature there exists two different models to capture the physical behavior of a ship in a mathematical hydromechanic model: the frequency domain model and the time domain model. Both models and their underlaying assumptions are discussed. Subsequently, since no viscous effects are included in either models, models to capture these viscous effects are presented and discussed.

2.1.1. Ship motions

A ship in a seaway has the ability to move in 6 directions, so called degrees of freedom. These degrees of freedom, or shortly DOFs, are visualized in Figure 2.1 and described in Table 2.1. The origin of the coordinate system is located at the ship's center of gravity (COG).

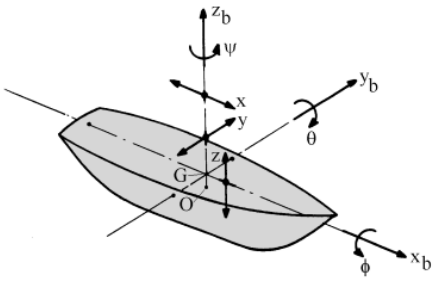

Figure 2.1: Ship motions in 6 degrees of freedom [20]

Motion	Name	Symbol	Unit
1	Surge	x	[m]
2	Sway	y	[m]
3	Heave	z	[m]
4	Roll	ϕ	[rad]
5	Pitch	θ	[rad]
6	Yaw	ψ	[rad]

Table 2.1: Description of ship motions and symbols

2.2. Frequency domain model

The frequency domain model is the most widely used method to calculate the response of a ship in a seaway. The approach is based on the assumption that the ship is excited by purely sinusoidal wave forces at a particular well defined frequency and that the resulting motions are small relative to the cross-sectional dimensions of the ship. Only the steady-state response can be be obtained using the frequency domain method. The model to calculate the ship response at zero-speed is equivalent to a frequency-dependent mass-damper-spring system. The model is mathematically defined by an 'apparent' differential equation according Cummins [7]:

$$[\mathbf{M} + \mathbf{A}(\omega)]\ddot{\eta} + \mathbf{B}(\omega)\dot{\eta} + \mathbf{C}\eta = \mathbf{F}(\omega)\cos(\omega t + \epsilon) \tag{2.1}$$

in which:

$\mathbf{M}$	=	ship inertia matrix
$\mathbf{A}(\omega)$	=	ship hydrodynamic added mass matrix
$\mathbf{B}(\omega)$	=	ship hydrodynamic damping matrix
$\mathbf{C}$	=	ship hydrostatic stiffness matrix
$\mathbf{F}(\omega)$	=	first-order wave excitation force amplitude vector
ω	=	wave frequency
η	=	ship motion amplitude vector, see Table 2.1
ϵ	=	phase angle vector
t	=	time vector

The ship is considered laterally symmetric. Therefore, no coupling terms other than the surge-heave-pitch and sway-roll-yaw coupling terms are included in the model. The frequency independent inertia matrix and hydrostatic stiffness matrix become:

$$\mathbf{M} = \begin{bmatrix} m_{11} & 0 & 0 & 0 & 0 & 0 \\ 0 & m_{22} & 0 & 0 & 0 & 0 \\ 0 & 0 & m_{33} & 0 & 0 & 0 \\ 0 & 0 & 0 & m_{44} & 0 & 0 \\ 0 & 0 & 0 & 0 & m_{55} & 0 \\ 0 & 0 & 0 & 0 & 0 & m_{66} \end{bmatrix} \qquad \mathbf{C} = \begin{bmatrix} 0 & 0 & 0 & 0 & 0 & 0 \\ 0 & 0 & 0 & 0 & 0 & 0 \\ 0 & 0 & c_{33} & 0 & c_{35} & 0 \\ 0 & 0 & 0 & c_{44} & 0 & 0 \\ 0 & 0 & c_{53} & 0 & c_{55} & 0 \\ 0 & 0 & 0 & 0 & 0 & 0 \end{bmatrix}$$

Where the first three diagonal terms in the inertia matrix represent masses and the last three terms represent rotational moments of inertia.

The energy that is carried away from the system due to the generation of surface waves as a result of the ship motions is captured in the radiation force, existing out of the added mass $\mathbf{A}(\omega)$ and potential damping $\mathbf{B}(\omega)$ according Fossen [11]:

$$\mathbf{A}(\omega) = \begin{bmatrix} a_{11} & 0 & a_{13} & 0 & a_{15} & 0 \\ 0 & a_{22} & 0 & a_{24} & 0 & a_{26} \\ a_{31} & 0 & a_{33} & 0 & a_{35} & 0 \\ 0 & a_{42} & 0 & a_{44} & 0 & a_{46} \\ a_{51} & 0 & a_{53} & 0 & a_{55} & 0 \\ 0 & a_{62} & 0 & a_{64} & 0 & a_{66} \end{bmatrix} \qquad \mathbf{B}(\omega) = \begin{bmatrix} b_{11} & 0 & b_{13} & 0 & b_{15} & 0 \\ 0 & b_{22} & 0 & b_{24} & 0 & b_{26} \\ b_{31} & 0 & b_{33} & 0 & b_{35} & 0 \\ 0 & b_{42} & 0 & b_{44} & 0 & b_{46} \\ b_{51} & 0 & b_{53} & 0 & b_{55} & 0 \\ 0 & b_{62} & 0 & b_{64} & 0 & b_{66} \end{bmatrix}$$

Due to lateral symmetry, the coupling terms in the above matrices are equal, so $c_{ij} = c_{ji}$, this also applies to a and b.

The first order wave excitation force amplitude is calculated by integration of the wave pressure acting on the submerged ship hull in a undisturbed wave. This is commonly referred to as the Froude-Krilov force according Journée [20]. The Froude-Krilov force is corrected since a part of the waves will be diffracted due to the presence of the hull in the fluid. The corrected first-order wave excitation force amplitude is denoted by $\mathbf{F}(\omega)$:

$$\mathbf{F}(\omega) = \begin{bmatrix} F_1 \\ F_2 \\ F_3 \\ F_4 \\ F_5 \\ F_6 \end{bmatrix}$$

Note that the last three terms in the first order wave excitation force amplitude vector represent moments, since the corresponding motions are rotations.

The added mass coefficients, damping coefficients, Froude-Krilov and diffraction forces can be obtained by using diffraction analysis software, such as for example, AQWA or WAMIT. In diffraction analysis, the ship geometry is represented by a discretized panel model. The theory underlying these solvers is very clearly and deliberately described by Journée [20] and Newman [21]. The discretized panel model of the *Ndurance* as implemented in AQWA is visualized in Figure 2.2. The vessel particulars are given in Appendix A.

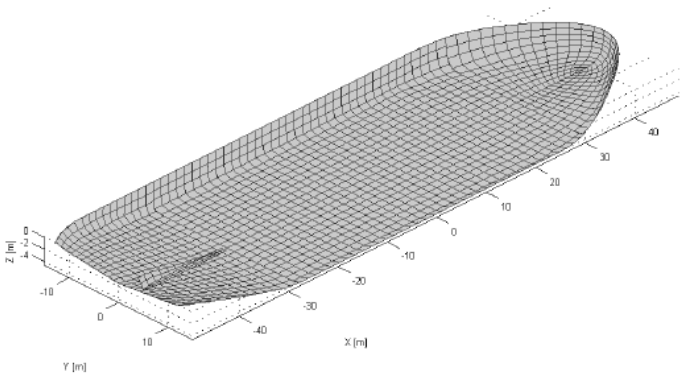

Figure 2.2: Panel model of the *Ndurance* in AQWA

Diffraction analysis is based on the assumption of potential flow, implying that the flow is assumed to be and to stay irrotational and non-viscous. As a consequence, it is not possible to calculate viscous effects by using diffraction analysis software.

Since a linear model is used to calculate the ship motions, the response of the ship in irregular waves can be calculated by using the superposition principle. The superposition principle allows the calculation of a motion response spectrum by using linear Response Amplitude Operators (RAO) and a defined wave spectrum according Journée [20]:

$$S_\eta(\omega) = \left|\frac{\eta(\omega)}{\xi}\right|^2 \cdot S_\xi(\omega) \tag{2.2}$$

in which:

$S_\eta(\omega)$	=	motion response spectrum
$\frac{\eta(\omega)}{\xi}$	=	motion RAO (motion amplitude / wave amplitude)
$S_\xi(\omega)$	=	wave spectrum

The RAO depends on the water depth, wave direction, draft and loading condition of the ship. A visualization of the ship motion RAOs are given in Figure 2.3.

Several statistical parameters of the ship motion response can be calculated according to the motion response spectrum. For example, the root mean square (RMS) value of the motion amplitudes, is calculated according Journée [20] by:

$$\eta_{RMS} = \sqrt{m_{0\eta}} = \sqrt{\int_0^\infty S_\eta(\omega) d\omega} \tag{2.3}$$

The root mean square value of the motion amplitude can be used to assess the operability of a specific offshore operation for each specific environmental condition characterized by a wave spectrum.

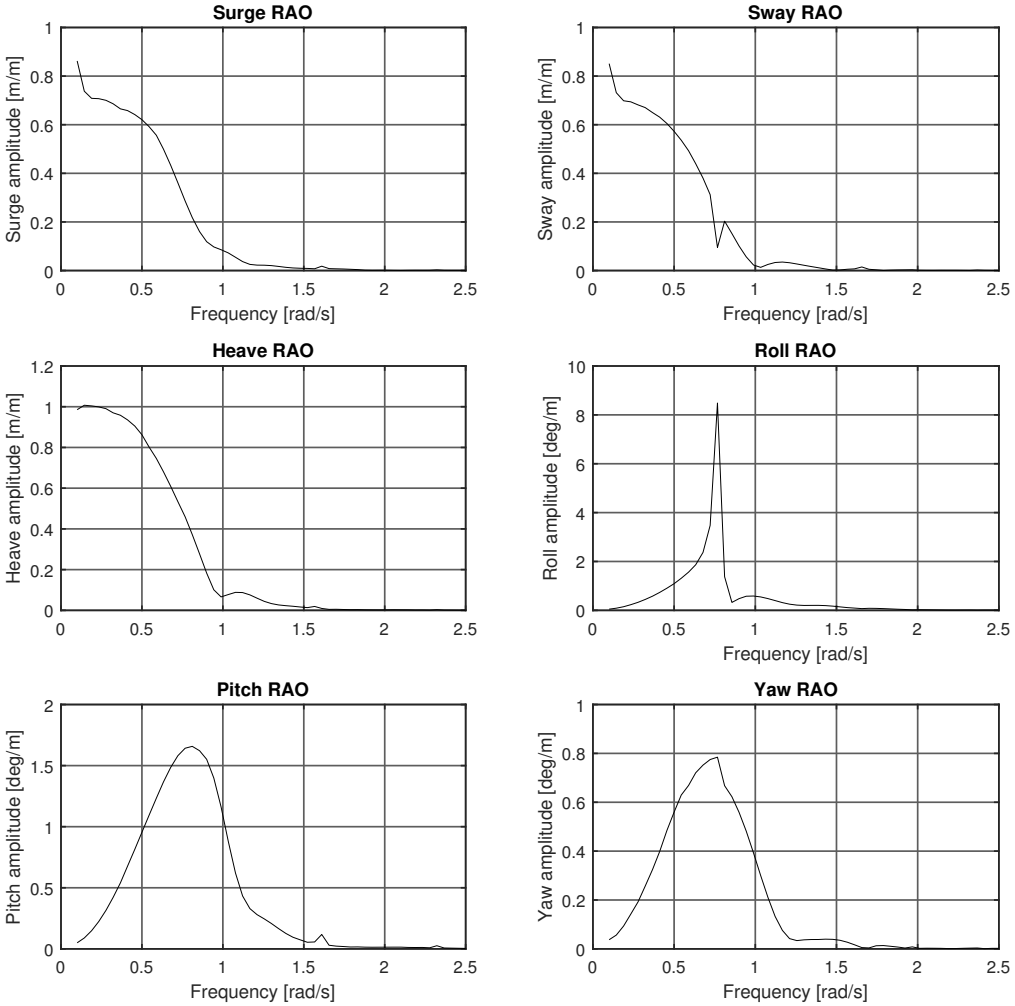

Figure 2.3: *Ndurance* Motion RAOs ($\mu = 45°$, T=4.7m, WD=1000m)

2.3. Time domain model

A limitation of the frequency domain model is its disability to calculate the ship response when it is subjected to non-linear or transient loads. To overcome this limitation, the time domain model as proposed by Cummins [7] can be used to calculate the transient ship response at zero speed by an integro-differential equation:

$$[\mathbf{M} + \mathbf{A}_\infty]\ddot{\eta} + \int_0^t \mathbf{K}(t-\tau)\dot{\eta}d\tau + \mathbf{C}\eta = F(t) \tag{2.4}$$

in which:

$\mathbf{A}_\infty$	=	infinite frequency added mass matrix
$\mathbf{K}$	=	retardation function matrix
$F(t)$	=	external excitation force

In the time domain model, the hydrodynamic damping term is represented by the convolution of the retardation function and the ship velocities. The infinite frequency added mass matrix and the retardation

function matrix are defined by:

$$\mathbf{A}_\infty = \begin{bmatrix} a_{11} & 0 & a_{13} & 0 & a_{15} & 0 \\ 0 & a_{22} & 0 & a_{24} & 0 & a_{26} \\ a_{31} & 0 & a_{33} & 0 & a_{35} & 0 \\ 0 & a_{42} & 0 & a_{44} & 0 & a_{46} \\ a_{51} & 0 & a_{53} & 0 & a_{55} & 0 \\ 0 & a_{62} & 0 & a_{64} & 0 & a_{66} \end{bmatrix}_\infty \qquad \mathbf{K} = \begin{bmatrix} K_{11} & 0 & K_{13} & 0 & K_{15} & 0 \\ 0 & K_{22} & 0 & K_{24} & 0 & K_{26} \\ K_{31} & 0 & K_{33} & 0 & K_{35} & 0 \\ 0 & K_{42} & 0 & K_{44} & 0 & K_{46} \\ K_{51} & 0 & K_{53} & 0 & K_{55} & 0 \\ 0 & K_{62} & 0 & K_{64} & 0 & K_{66} \end{bmatrix}$$

The retardation function is the impulse response function of the ship. It takes into account the so-called fluid memory. The retardation function can be calculated for every ship motion and coupling term according Fossen [11] by:

$$\mathbf{K}(t) = \frac{2}{\pi} \int_0^\infty \mathbf{B}(\omega) \cos(\omega t) d\omega \tag{2.5}$$

The infinite frequency added mass is the hydrodynamic added mass evaluated at infinite frequency. It is defined according Fossen [11] by:

$$\mathbf{A}_\infty = \overline{\mathbf{A}_\infty} = \mathbf{A}(\omega) + \frac{1}{\omega} \int_0^\infty \mathbf{K}(t) \sin(\omega t) dt \tag{2.6}$$

As can be derived from equation 2.6, the infinite frequency added mass is calculated by averaging over the complete frequency range. It can be derived from the equations of the retardation function and the infinite frequency added mass, that the time domain approach is constructed from hydrodynamic coefficients in the frequency domain. Therefore, the added mass and damping coefficients, calculated by diffraction analysis can be used to develop a time domain model.

Because of the ability to calculate the vessel transient response when subjected to non-linear forces and for simulation and controller design purposes, see Fossen [11], it is decided to simulate the motion response of the *Ndurance* in the time domain.

2.3.1. The convolution term

The convolution integral in equation 2.4, can make the simulation of the ship motion time and memory consuming according Armesto [1]. This is the result of the fact that the convolution integral equation requires to integrate all the way back to the start of the simulation at every time step. This causes simulations to run increasingly slower when the simulation time increases. In literature, three different approaches to compute the radiation term in Cummins' equation can be found:

- Direct integration of the convolution term by the Impulse Response Function (IRF), see Ricci [27].
- Computation of the convolution term by a State-Space (SS) model, see Perez [25].
- Computation of the convolution term by using Prony's coefficients to estimate the IRF, see De Backer [8].

In literature, the state-space method is commonly used to model the dynamic ship response in the time domain. This is due to the computational performance of the method and its suitability for control purposes, see Hatecke [13]. Due to these advantageous properties it is decided to use the state-space method to evaluate the convolution term in Cummins' equation.

State-space representation requires that a dynamic system is linear and time-invariant. Since the radiation term in Cummins' equation satisfies these conditions, it is possible to compute the fluid-memory effects by an approximated state-space model:

$$\kappa = \int_0^t \mathbf{K}(t-\tau)\dot{\eta} d\tau \simeq \left| \begin{array}{ll} \dot{x} = & \mathbf{A}_{ss} x + \mathbf{B}_{ss} \dot{\eta} \\ \kappa = & \mathbf{C}_{ss} x \end{array} \right. \tag{2.7}$$

in which:

$\dot{x} =$ state vector
$\mathbf{A}_{ss} =$ state-space system matrix
$\mathbf{B}_{ss} =$ state-space input matrix
$\mathbf{C}_{ss} =$ state-space output matrix

The strategy to construct the state-space models is based on the work of Perez and Fossen [24]. First, the retardation functions, or IRFs, are calculated in the time domain in order to calculate the values of the infinite frequency added mass matrix. According these results, the IRF is transformed to the frequency domain. This feels like a natural approach, since the added mass and damping coefficients as calculated by diffraction analysis are already represented in the frequency domain. Next, a transfer function (TF) is fitted through the IRF and the fitted transfer function is subsequently transformed back to the time domain by the state-space representation. A diagram of the strategy to construct the state-space models is given in Figure 2.4.

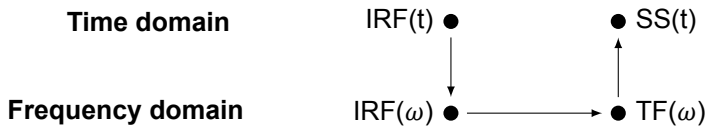

Figure 2.4: Strategy to obtain state-space representation

It may seem a more logical approach to directly transform the IRF to the state-space model in the time domain. However, this is significantly more complex, due to the fact that the order of the system is hard to guess by looking at the IRF alone and it is not possible to enforce the model to dynamic system constraints. The calculation steps visualized in Figure 2.4 will be presented in more detail in the following sections.

2.3.2. IRF in the time domain

The IRF needs to be calculated in the time domain to obtain an expression for the infinite added mass terms, see Equation 2.6. The formula for the IRF is evaluated at infinite frequency. This yields problems, since the IRF needs to be calculated by a numerical model. Therefore, the function is only evaluated until a cut-off frequency, in this case 4.5 rad/s. The cut-off frequency is determined by the diffraction software, since computational-wise, the software is not able to calculate higher frequency data for the panel model used.

Two different numerical models to calculate the IRF of the ship motion and coupling terms are evaluated in this study. One is used in the simulation program OrcaFlex [23] and the other is proposed by Journée [16].

The model used in OrcaFlex [23] is formulated by:

$$\mathbf{K}(t) = \exp\left[\left(\frac{-3t}{T_c}\right)^2\right] \cdot \sum_{n=1}^{N} 2\Delta B_n(\omega)\Delta\omega_n \cos(\omega t) \tag{2.8}$$

in which:

N = total number of frequencies
t = time vector
ΔB_n = hydrodynamic damping, $B_n - B_{n-1}$
$\Delta\omega_n$ = wave frequency, $\omega_n - \omega_{n-1}$
T_c = cut-off scaling time constant

The variable T_c can be adjusted to smoothly scale down the IRF function. A high value results in low smoothing of the IRF.

According to Journée [16], the discretized model of the IRF is:

$$\mathbf{K}(t) = \frac{2}{\pi t^2} \cdot \sum_{n=1}^{N} \left(\frac{\Delta B_n}{\Delta \omega} \left[\cos(\omega_n t) - \cos(\omega_{n-1} t) \right] \right) + \frac{2}{\pi t} \cdot B_N \sin(\omega_N t) \tag{2.9}$$

in which:

B_N = hydrodynamic damping at the cut-off frequency
ω_N = cut-off frequency

Both models have been implemented to check whether they are in agreement and to confirm the correct implementation of the numerical IRF model. The calculated IRFs for the six motion components using both methods are given in Figure 2.5.

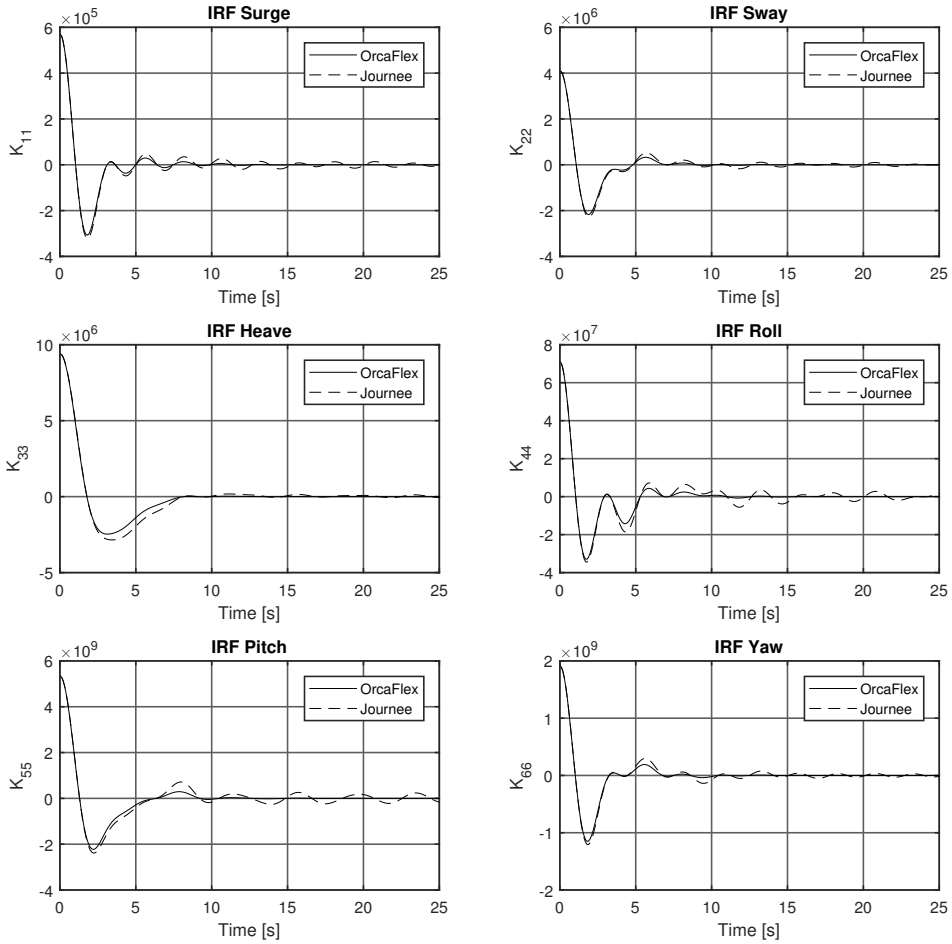

Figure 2.5: Calculated motion IRFs using the OrcaFlex and Journée models, T_c=50s

From Figure 2.5 can be concluded that both models result in the same estimation of the motion IRFs. The effect of the smoothing function defined by the variable T_c is clearly visible in the results. The OrcaFlex model estimates smoothen out significantly quicker compared to the Journée model. To increase the accuracy of the infinite frequency added mass calculation, it is decided to use the IRF model as proposed by Journée [16].

2.3.3. IRF in the frequency domain

The calculated IRF in the time domain needs to be subsequently transferred to the frequency domain. This is achieved according Fossen [11] by:

$$\mathbf{K}(\omega) = \mathbf{B}(\omega) + i\omega[\mathbf{A}(\omega) - \mathbf{A}_\infty] \tag{2.10}$$

From Equation 2.10 can be concluded that first the infinite frequency added mass matrix needs to be calculated. This is done according the calculated IRFs for the ship motion and coupling terms, see Equation 2.6. Again the integration needs to be cut-off, since integration at infinity is not possible using numerical techniques. The results of the infinite frequency added mass terms for the six motion components are calculated and plotted together with the frequency-dependent added mass estimates as calculated by the AQWA diffraction software in Figure 2.6.

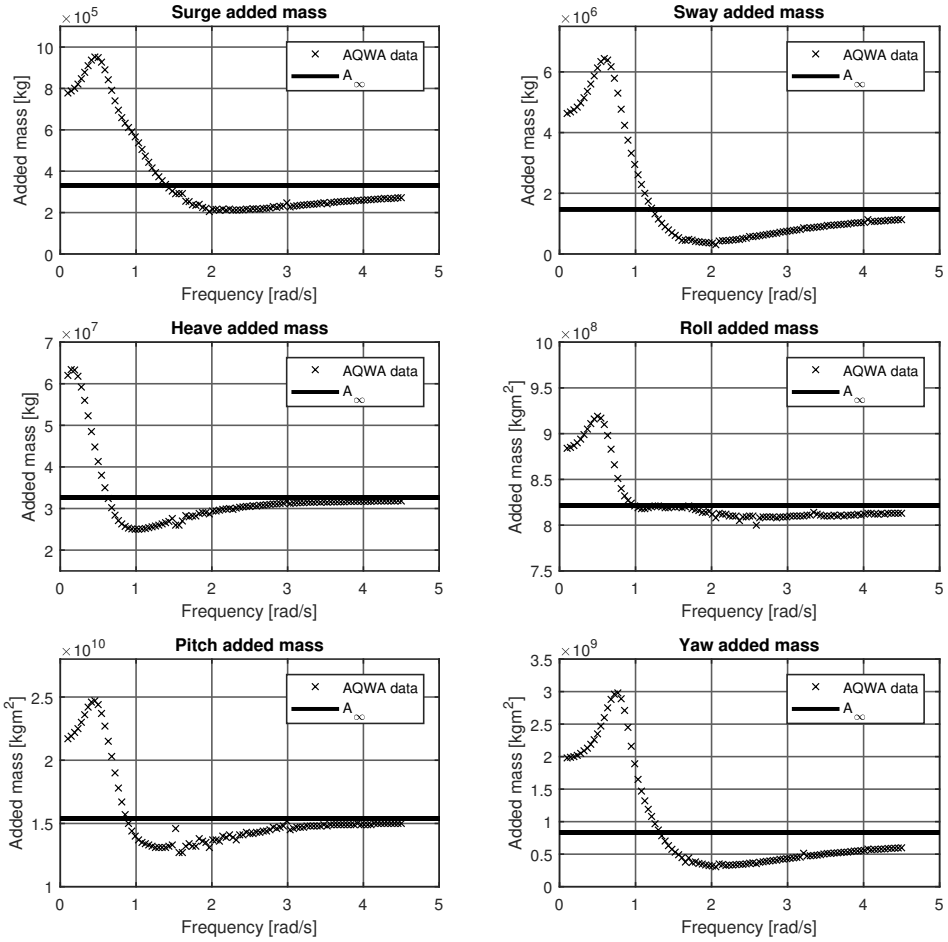

Figure 2.6: Frequency-dependent added mass for six ship motions and calculated infinity frequency added mass estimates

From Figure 2.6 can be observed that the added mass estimates as calculated by the diffraction software AQWA approach the calculated infinite frequency added mass estimate in the high frequency limit. From this can be concluded that the numerical model to calculate the infinity frequency added mass is implemented correctly and produces reliable results.

2.3.4. Transfer function fitting

The next step is to fit transfer functions through the calculated IRFs in the frequency domain. An extensive paper regarding the fitting method and procedure is written by Duarte [10]. To obtain the coefficients matrices $\mathbf{A}_{ss}$, $\mathbf{B}_{ss}$ and $\mathbf{C}_{ss}$ of the state-space models, a transfer function fitting algorithm is used. The steps executed in the algorithm are described in the following enumeration:

1. A parametric transfer function is fitted through the retardation function in the frequency domain defined by:

$$\tilde{K}(s) = \frac{P(s)}{Q(s)} = \frac{p_m s^m + p_{m-1} s^{m-1} + \ldots + p_0}{s^n + q_{n-1} s^{n-1} + \ldots + q_0} \tag{2.11}$$

   in which:

s	=	Laplace complex variable
p	=	nominator coefficients
q	=	denominator coefficients
m	=	order of nominator
n	=	order of denominator

2. A least squares method is solved to minimize the error between the fitted transfer function and the retardation function:

$$\min \sum_{k=1}^{n} w_t(k) |K(k)Q(w(k)) - P(w(k))|^2 \tag{2.12}$$

   In which w_t is a vector with weight factors and n is the number of frequency points. This method is implemented in the Matlab function 'invfreqs'.

3. The weight factors are calculated by:

$$w_t(k) = \frac{1}{|p(k) + i\omega(k)|^2} \tag{2.13}$$

4. The quality of the fit is calculated by:

$$R^2 = 1 - \frac{\sum (K(s) - \tilde{K}(s))^2}{\sum (K(s) - \overline{K}(s))^2} \tag{2.14}$$

According to Perez [25], some specific properties of the convolution terms have implications on the parametric transfer function models. The convolution term properties and their implications are listed in Table 2.2.

Property	Implication on parametric model
$\lim_{\omega \to 0}$ K(iω)=-B(∞)	K(s) is zero at s=0
$\lim_{\omega \to \infty}$ K(iω)=0	TF is strictly proper
K(t=0^+)=$\int_0^\infty [B(\omega) - B(\infty)] d\omega \neq 0$	TF relative degree is 1
$\lim_{t \to \infty}$ K(t)=0	TF is BIBO stable
Re(K(iω))$\geq$0	K(s) is passive, diagonal terms are positive real

Table 2.2: Convolution term properties and corresponding implications on the fitted transfer function (TF) according Perez [25]

The properties as given in Table 2.2 are incorporated in the transfer function fitting algorithm. The minimum order of the transfer function is set to 2, since it is not possible to fit a first-order transfer function to the retardation function. In the fitting procedure this order is increased and the weight vector is re-evaluated until the transfer function estimate has a fit quality of at least 0.9. The results of the fitting procedure are given in Figure 2.7.

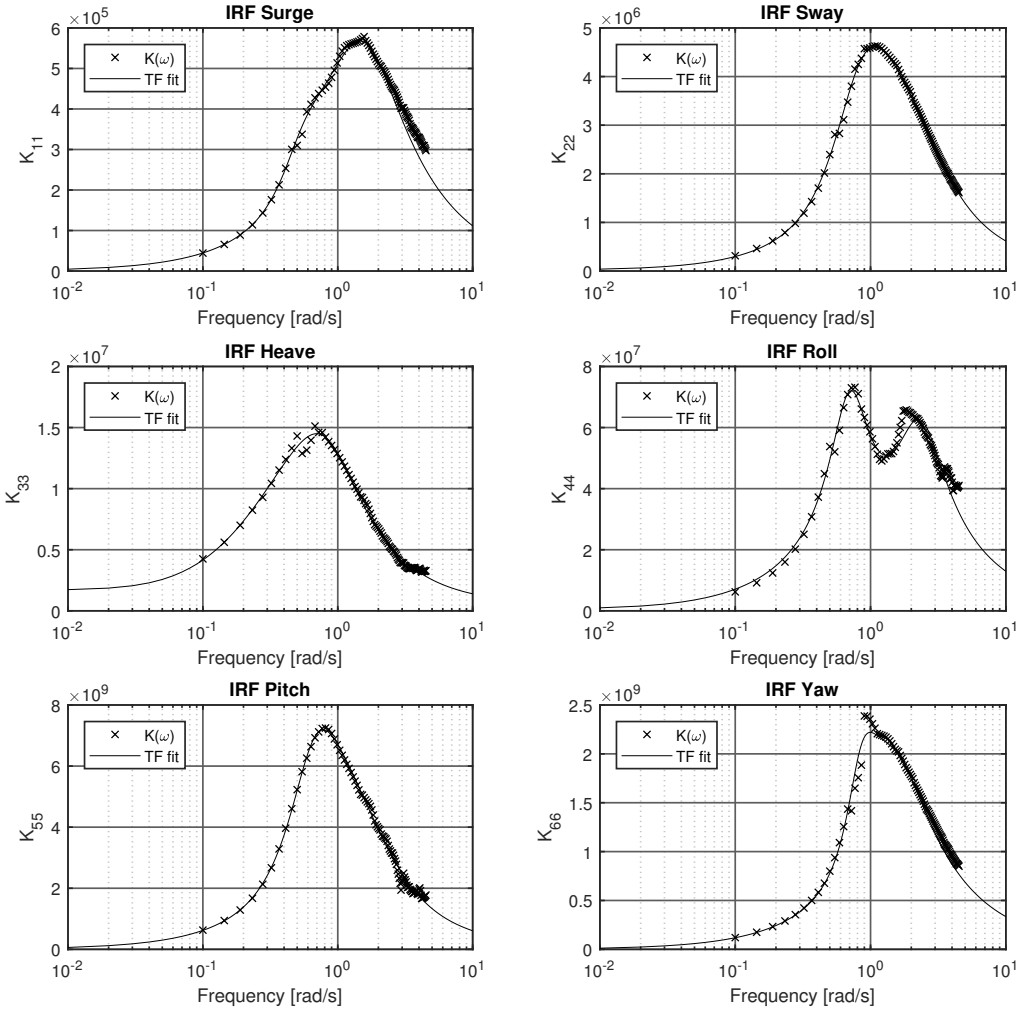

Figure 2.7: Frequency domain motion IRFs and fitted transfer functions

A transfer function is fitted through every motion and coupling term component. As can be derived from Figure 2.7, the fitted transfer functions are approximating the IRF functions quite well. The roll and yaw motions show some slight underestimation of the peaks at the higher frequencies, but it is expected that these effects are negligible. The transfer functions are subsequently transformed to a state-space model using the 'tf2ss' function in Matlab.

2.3.5. Time domain model verification

The time domain model in which the convolution terms are replaced by equivalent state-space representations is defined by:

$$[\mathbf{M} + \mathbf{A}_\infty]\ddot{\eta} + \mathbf{K}_{ss}\dot{\eta} + \mathbf{C}\eta = F(t) \tag{2.15}$$

where,

$$\mathbf{K}_{ss} = \begin{bmatrix} \kappa_{11} & 0 & \kappa_{13} & 0 & \kappa_{15} & 0 \\ 0 & \kappa_{22} & 0 & \kappa_{24} & 0 & \kappa_{26} \\ \kappa_{31} & 0 & \kappa_{33} & 0 & \kappa_{35} & 0 \\ 0 & \kappa_{42} & 0 & \kappa_{44} & 0 & \kappa_{46} \\ \kappa_{51} & 0 & \kappa_{53} & 0 & \kappa_{55} & 0 \\ 0 & \kappa_{62} & 0 & \kappa_{64} & 0 & \kappa_{66} \end{bmatrix}$$

The κ-terms represent the state-space representations of the motion and coupling terms defined by the state-space coefficients matrices $\mathbf{A}_{ss}$, $\mathbf{B}_{ss}$ and $\mathbf{C}_{ss}$.

The time domain model has been constructed in the simulation software Simulink. Both the frequency and time domain model are subjected to equal harmonic quartering wave forces and moments over a frequency interval of 0.1 to 2.5 rad/s. In this way the RAOs as visualized in Figure 2.3 are reconstructed and the time domain model is checked for the complete range of frequencies. The motion amplitude results as calculated by both models are compared to check whether the results are in agreement. The results are visualized in Figure 2.8.

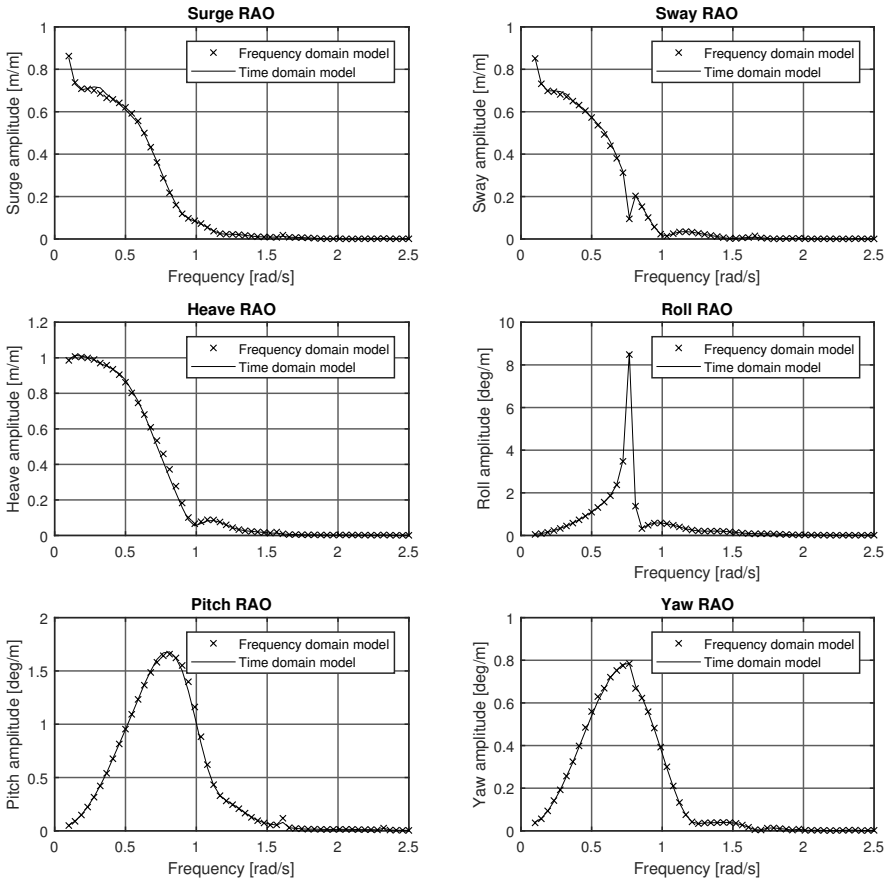

Figure 2.8: Comparison of calculated RAOs by both frequency and time domain model ($\mu = 45°$, T=4.7m, WD=1000m)

From Figure 2.8 can be observed that the calculated motion amplitudes are in good agreement for all 6 motion components. From these results is concluded that the constructed time domain model is implemented correctly, since it produces motion amplitude estimates similar to the frequency domain model when subjected to harmonic forces and moments.

To quantify the agreement between the motion estimates obtained by both models, the Relative Mean Absolute Error (RMAE) of each motion is calculated. The RMAE is defined by:

$$\text{RMAE} = \frac{\frac{1}{n}\sum_{i=1}^{n}|y_i - \hat{y}_i|}{|y_{max} - y_{min}|} \cdot 100\% \tag{2.16}$$

in which

$$\begin{aligned} n &= \text{total number of data points} \\ y_i &= \text{frequency domain result} \\ \hat{y}_i &= \text{time domain result} \\ y_{max} &= \text{maximum value in result range} \\ y_{min} &= \text{minimum value in result range} \end{aligned}$$

The RMAE value for each motion component visualized in Figure 2.8 is calculated and are given in Table 2.3.

Motion	**RMAE [%]**
Surge	0.36
Sway	0.25
Heave	0.59
Roll	0.05
Pitch	0.59
Yaw	0.33

Table 2.3: RMAE values of indicated ship motions

From Table 2.3 can be derived that that the maximum RMAE value is 0.59% for both the heave and pitch motion. A magnitude of 0.59% is considered negligible and therefore it is concluded that the time domain model with state-space representation is capable to correctly calculate the vessel motion response.

2.4. Viscous roll damping

Viscous effects are neglected when potential theory is used to calculate ship motions. This means that the damping only represents the energy dissipated by the radiated waves. Since the motions of a ship are largely inertia driven, the results obtained by potential theory are in general sufficiently accurate to correctly calculate the motion response.

For the roll motion however, viscous effects are of more importance. A significant amount of energy is dissipated by the formation of eddies at the bilges. This energy contributes to the roll damping of the ship. The contribution of the viscous damping to the total roll damping of the ship is found to be difficult to determine. Two approaches are commonly seen in literature:

1. Experimental model tests
2. Empirical models

Since no model test results of the *Ndurance* are available, an empirical model approach is used to take into account the effect of viscous roll damping.

2.4.1. Ikeda viscous damping model

As stated by Chakrabarti [5], the viscous roll damping term is a function of the roll velocity and can be expressed by:

$$B(\dot{\phi}) = B_1\dot{\phi} + B_2|\dot{\phi}|\dot{\phi} + B_3\phi^3 \tag{2.17}$$

where B_1, B_2 and B_3 represent linear, quadratic and cubic viscous damping coefficients. Since no higher order terms can be incorporated in the frequency domain model, the total damping is subsequently approximated by a linear equivalent damping term:

$$B(\dot{\phi}) = B_{eq}\dot{\phi} \tag{2.18}$$

According to Himeno [14], the equivalent viscous damping coefficient can be expressed in terms of its various contributions:

$$B_{eq} = B_f + B_e + B_L + B_{BK} \tag{2.19}$$

in which:

B_f = skin friction damping
B_e = eddy making damping
B_L = lift damping
B_{BK} = bilge keel damping

For each of this contributions a specific empirical model has been constructed according to experimental results. Since the *Ndurance* has no bilge keels and only the zero-speed condition is of interest, this equation can be reduced to:

$$B_{eq} = B_e + B_f \tag{2.20}$$

A schematic visualization of the eddy making and skin friction damping is given in Figure 2.9.

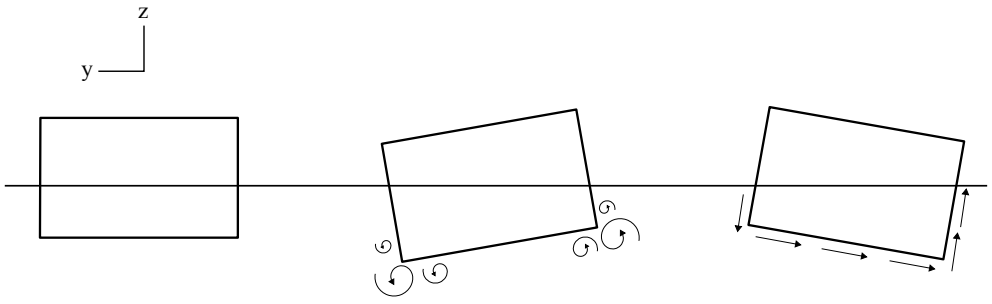

Figure 2.9: Schematic visualization of eddy making damping and skin friction damping

Eddy making damping
Eddy making damping arises due to the separation of vortices at the bilges of the ship. For ships with a barge-like rectangular midsection like the *Ndurance*, the contribution of the eddy making damping is most significant amidships. According to Ikeda [15], the eddy making damping coefficient of the bare ship hull with a rectangular cross-section is formulated by:

$$B_e = \frac{2}{\pi}\rho L D^4 (H_0^2 + 1 - OG/D)[H_0^2 + (1 - OG/D)^2] R_0 \omega \tag{2.21}$$

in which:

ρ	=	sea water density
L	=	ship length
D	=	draft
H_0	=	half of the beam-draft ratio (B/2D)
R_0	=	roll motion amplitude
OG	=	vertical distance from still water line (SWL) to COG

The eddy making damping model assumes that the hull has a rectangular (90°) bilge and that the rectangular cross sections is present over the complete length of the ship (section coefficient $C_M = 1$). The *Ndurance* has more ship-like sections in the aft and front of the ship. Next to this, the *Ndurance* has a slightly rounded bilge. Therefore, the length of the part of the ship at which the sections have a $C_M \geq 0.99$ has been selected as an equivalent length to be used in Equation 2.21. The length for which $C_M \geq 0.99$ is 54 meters.

Skin friction damping
Friction damping is the result of skin friction stress that acts on the ship hull. The skin friction stress is induced by the sea water viscosity and the roll motion of the ship. According Himeno [14], the skin friction damping coefficient can be expressed by:

$$B_f = 0.787 \rho S r_e^2 \sqrt{\omega \nu} \left\{ 1 + 0.00814 \left(\frac{r_e^2 R_0^2 \omega}{\nu} \right)^{0.386} \right\} \tag{2.22}$$

in which:

ρ	=	sea water density
S	=	wetted hull surface
r_e	=	effective bilge radius
ν	=	kinematic viscosity of water
R_0	=	roll motion amplitude

The effective bilge radius r_e is expressed by:

$$r_e = \frac{1}{\pi}\left[(0.887 + 0.145 C_B) \frac{S}{L} - 2OG \right] \tag{2.23}$$

in which:

C_B	=	ship block coefficient

2.4.2. Frequency domain model

As can be derived from Equation 2.21 and Equation 2.22, both the eddy making damping coefficient and the skin friction damping coefficient depend on the wave frequency and the roll motion amplitude. However, the roll motion amplitude also depends on the damping coefficients. To include this interaction, the damping coefficients are calculated by using an iterative approach. The damping coefficients are calculated by using the roll motion amplitude estimates of the frequency domain model without the implementation of a viscous damping term. Subsequently, the viscous damping coefficients are calculated and implemented in the frequency domain model:

$$[\mathbf{M} + \mathbf{A}(\omega)]\ddot{\eta} + \mathbf{B}(\omega)\dot{\eta} + B_{eq}\dot{\phi} + \mathbf{C}\eta = \mathbf{F}(\omega)\cos(\omega t + \epsilon) \tag{2.24}$$

The calculated roll motion amplitudes are then used to calculate a new viscous damping coefficient estimate for every frequency. This process is repeated until the viscous damping term is converged. The results of the iterative procedure are visualized in Figure 2.10.

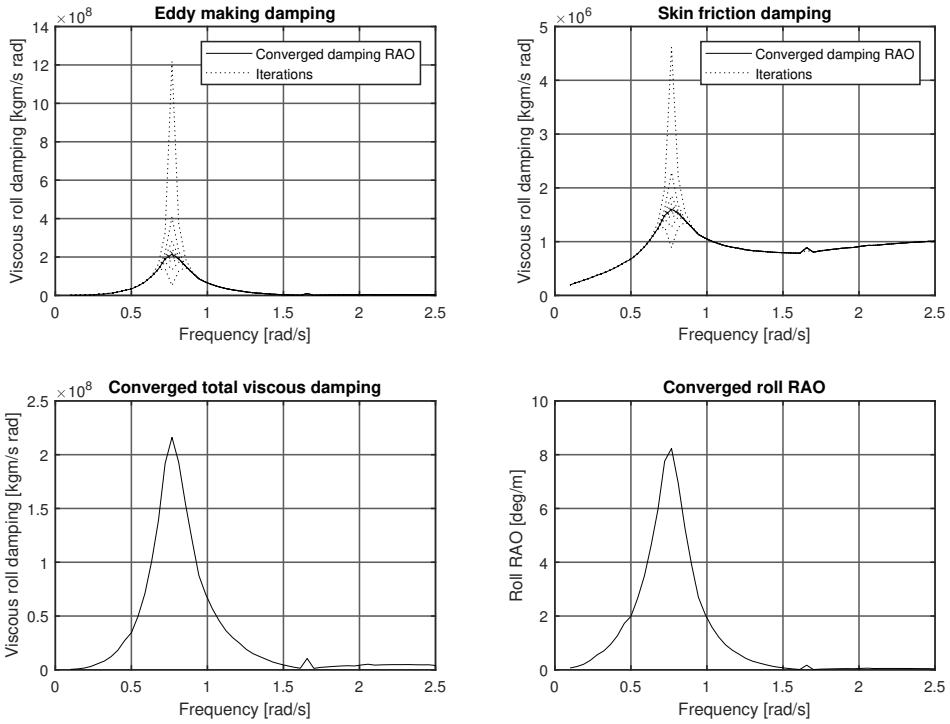

Figure 2.10: Results of iterative calculation of viscous damping RAOs and final roll motion RAO in the frequency domain model ($\mu = 90°$, T=4.7m, WD=1000m)

From Figure 2.10 can be observed that both the damping RAOs and the roll motion RAO converge to a final value. Also, the total converged viscous damping term RAO and the roll motion RAO are visualized.

2.4.3. Time domain model

In the time domain model it is possible to incorporate a quadratic damping term. This is considered a more physical approach, since it is known that drag forces have a quadratic relation with velocity, see for example Chakrabarti [5]. Therefore a quadratic viscous damping term is included, defined by:

$$B_{visc} = c_1|\dot{\phi}|\dot{\phi} \tag{2.25}$$

where c_1 is a fitting parameter. The value of this fitting parameter is obtained by fitting the time domain roll motion RAO to the frequency domain roll motion RAO with a linearized viscous roll damping term included. The time domain model with a viscous roll damping term included is now defined by:

$$[\mathbf{M} + \mathbf{A}_\infty]\ddot{\eta} + \mathbf{K}_{ss}\dot{\eta} + c_1|\dot{\phi}|\dot{\phi} + \mathbf{C}\eta = F(t) \tag{2.26}$$

By adjusting the value of c_1, the time domain roll motion RAO is fitted to the frequency domain roll motion RAO. The result is visualized in Figure 2.11

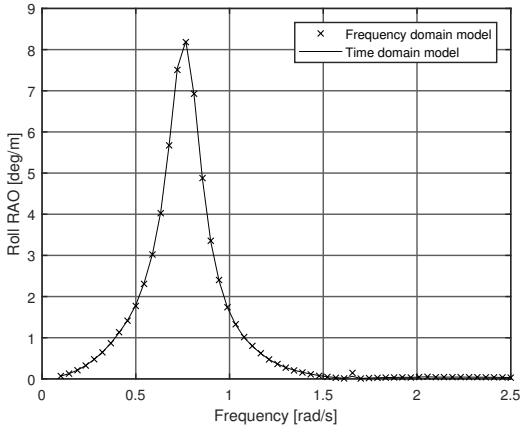

Figure 2.11: Results of time domain model RAO fitting to frequency domain RAO ($\mu = 90°$, T=4.7m, WD=1000m)

From Figure 2.11 can be observed that the roll motion RAO as calculated by both models are in good agreement. The value of the tuning parameter is determined as $c_1 = 2.2{\cdot}10^9$. To quantify the agreement between the frequency domain model and the time domain model, the RMAE is calculated according Equation 2.16. From this calculation is found that the RMAE of the results is 0.11%. This is considered negligibly small and therefore it is concluded that the match between the time domain model and the frequency domain model is excellent.

One should be aware of the fact that the frequency and time domain roll motion RAO only match for harmonic waves with unit amplitude. For higher wave amplitudes, the roll motion velocity will increase and therefore the time domain model will overestimate the viscous roll damping, due to the quadratic term, in comparison to the frequency domain model. For lower wave amplitudes, the opposite applies. This behavior is visualized in Figure 2.12.

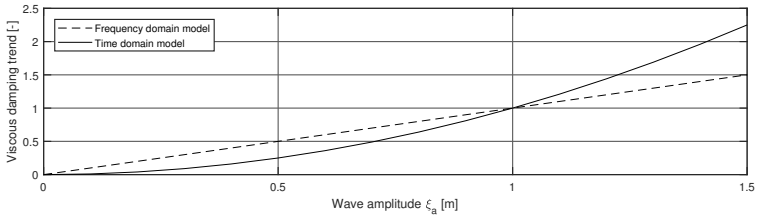

Figure 2.12: Viscous roll damping trend visualization in both frequency and time domain model

Since it is known that the viscous damping term has a quadratic relation regarding the roll velocity, it is assumed that the time domain model yields more physically correct results.

2.5. Conclusions

The first sub-research objective is formulated as:

"Develop a 6 DOF ship model in the time domain that captures the ship response to environmental forces and validate this model with frequency domain data."

Two models to calculate the ship motion response have been presented and evaluated in this chapter. The time domain model is constructed based on state-space representation of the convolution term. Empirical models are used to calculate the viscous damping terms in the frequency domain. The viscous roll damping term is incorporated in the time domain by inclusion of a quadratic fitting coefficient.

From this research is concluded that:

- It is possible to evaluate the convolution term in the time domain model by an equivalent state-space model.

- The maximum relative mean absolute error between the frequency domain model motion results and the time domain model motion results is 0.59%. This is considered small enough to conclude that the time domain model is verified by frequency domain results.

- It is possible to use a quadratic parameter in order to match the frequency domain and the time domain model roll motion RAO with a viscous damping term included.

- The maximum relative mean absolute error between the frequency domain roll RAO and the tuned time domain roll RAO is 0.11%. This error is considered negligible and therefore it is concluded that time domain model tuning procedure is verified for unit wave amplitudes.

3
Thruster Model

To achieve thruster induced roll reduction, the thrusters need to counteract the first-order roll moment. The dynamic response of the thrusters is therefore important to model. Methods and models to estimate and simulate the thruster performance in transient condition are presented in this chapter.

3.1. Introduction

The *Ndurance* is equipped with a diesel-electric propulsion system. The thruster system lay-out structure is schematically visualized in Figure 3.1

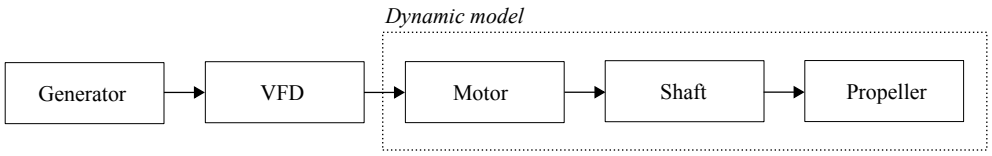

Figure 3.1: Schematic structure of thruster system lay-out

The generator is driven by a diesel engine that ensures the system is fed with electrical energy. The variable frequency drive (VFD) is a controller that regulates the motor torque and speed by controlling the stator magnetic motor flux. The required flux is calculated according the so-called vector control method. See for example Bargmeyer [2]. The electric motor is a three-phase asynchronous motor. The motor is connected to a drive shaft which transfers the rotational movement and torque of the motor to the gearbox. The gearbox reduces the rotational speed and increases the torque, which are subsequently transferred to the propeller. The rotation of the propeller results in thrust. Since the propeller is a fixed pitch propeller, the system dynamics are characterized by the components indicated in Figure 3.1. A model is presented which is able to capture the dynamic behavior of the thruster system.

The propeller will operate in fluctuating inflow conditions due to the roll motion of the vessel, see Figure 3.2.

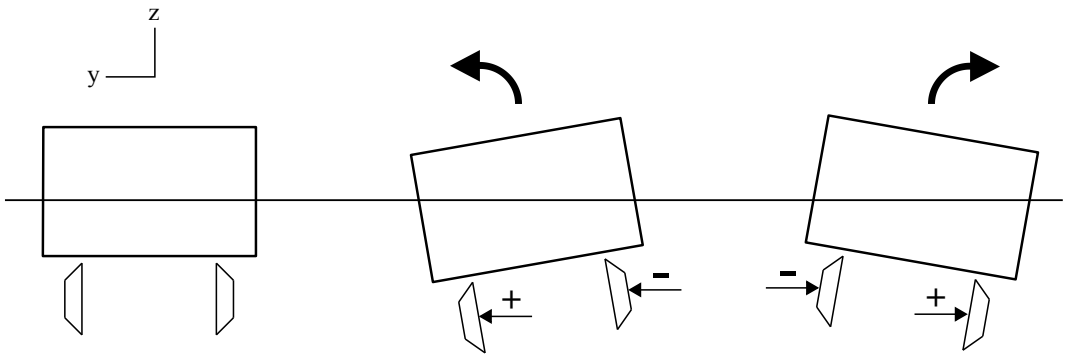

Figure 3.2: Schematic visualization of oscillating thruster inflow velocities due to the rolling motion of the vessel

As a result of this, the thrust and torque production will also change. A method to capture the thruster behavior when operating in these fluctuating inflow conditions will be presented and implemented.

3.2. Dynamic model

During roll reduction mode, the thrusters are used to counteract the first-order roll moment. This entails that the thrusters will be ramping up and down during one wave period. The response time of the thrusters is considered an important parameter regarding the possibility and magnitude of thruster induced roll reduction. To analyze the response time of the thrusters, a dynamic thruster model is constructed.

In literature there exist several modelling approaches. Cooke [6] proposes an energy-based dynamic model based on lumped parameters:

$$\dot{\omega} = \beta Q - \alpha\omega|\omega| \tag{3.1}$$

in which:

ω	=	propeller angular velocity
α, β	=	constant model parameters
Q	=	input torque

As can be derived from above equation, the propeller angular acceleration is depended on the difference between the torque delivered by the drive system and the torque required by the propeller. It is assumed that the parameters α and β remain constant during operation. Smogeli [32], proposes a more elaborate model that also includes a shaft friction term:

$$I_s\dot{\omega} = k_g Q_m - Q_p(\omega, \beta) - Q_f(\omega) \tag{3.2}$$

$$\dot{Q}_m = \frac{1}{T_m}(Q_{cm} - Q_m) \tag{3.3}$$

in which:

k_g	=	gearbox ratio
$Q_p(\omega, \beta)$	=	propeller torque
Q_{cm}	=	commanded motor torque
T_m	=	time constant
Q_m	=	motor torque
I_s	=	rotational inertia of motor, shaft and propeller
$Q_f(\omega)$	=	shaft friction term
β	=	hydrodynamic pitch angle

The shaft friction term is defined by:

$$Q_f(\omega) = \text{sign}(\omega)Q_s + K_\omega\omega \tag{3.4}$$

where Q_s and K_ω represent respectively the static shaft friction term and the linear friction term.

3.2.1. Entrained water added rotational moment of inertia

Smogeli [32] acknowledges the fact that there exists an added mass term due to the hydrodynamic forces in phase with the propeller rotational acceleration. However, in his work this term is neglected. This will give a reduced total system inertia, and hence faster dynamics. For conservatism, an empirical estimate of the inertia term is included in the total inertia of the thruster system I_s.

According to Saunders [29], the entrained water moment of inertia is defined by:

$$I_E = K \cdot I_p \tag{3.5}$$

where I_p is the propeller moment of inertia and K is a factor in the range of 0.25-0.50, where a factor of 0.25 is often used as a representative value. This method has a big uncertainty. Therefore, the

empirical estimates of the added inertia term are calculated based on the work of MacPherson [19] and Schwaneke [30]. In their work, the added rotational inertia term of the entrained water is defined by:

$$I_E = C_{IE}\rho D^5 \tag{3.6}$$

in which:

C_{IE} = fitting parameter
ρ = water density
D = propeller diameter

The fitting parameter C_{IE} is defined according Schwanecke [30] by:

$$C_{IE} = \frac{0.0703(P/D)^2 EAR^2}{\pi Z} \tag{3.7}$$

in which:

P/D = propeller pitch-diameter ratio
EAR = propeller expanded area ratio
Z = total number of propeller blades

MacPherson [19] proposes the following expression for the fitting parameter C_{IE}:

$$C_{IE} = C_1 EAR(P/D) - C_2 \tag{3.8}$$

where C_1 and C_2 are fitting parameters given in Table 3.1.

Parameter	Z=3	Z=4	Z=5	Z=6
C_1	0.00477	0.00394	0.00359	0.00344
C_2	0.00093	0.00087	0.00080	0.00076

Table 3.1: Fitting coefficients according MacPherson [19]

Since both empirical models are based on model test results carried out using different propeller types, the average of the model results is used as a representative value for the inertia term.

According Smogeli [32], the total rotational moment of inertia can be calculated from a motor or propeller point of view. It is decided to use the motor point of view, since this is the component that is controlled. Using this approach, the total system rotational moment of inertia is defined by:

$$I_s = \frac{I_p + I_{ps} + I_E}{k_g^2} + I_r \tag{3.9}$$

in which:

I_p = propeller rotational moment
I_{ps} = propeller shaft rotational moment
I_r = rotor rotational moment

3.2.2. Four-quadrant model

As can be observed from Figure 3.2, the thrusters will experience oscillating inflow velocities due to the rolling motion of the vessel. These oscillating inflow velocities will affect the thrust and torque production of the thrusters.

The thrust and torque characteristics of a wide range of propellers and ducted propellers is tested experimentally. The results are captured by so-called C_T and C_Q diagrams. These diagrams show the thrust (C_T) and torque (C_Q) coefficients as a function of the ship's advance velocity, see for example Stapersma [34]. However, these diagrams do not capture the thrust and torque behavior when the propeller is subjected to a reversed inflow, or when the propeller is in braking mode. MARIN [34] developed the so called four-quadrant model to extend the C_T and C_Q diagrams to the full operating range of a propeller. The four quadrants are divided as shown in Table 3.2.

Quadrant	β [deg]	**Ship speed** V_s	**Propeller speed** n_p	**Description**
1	0-90	+	+	normal forward operation
2	90-180	-	+	forward thrust at negative speed
3	180-270	+	-	reversing propeller during stopping
4	270-360	-	-	normal astern operation

Table 3.2: Four quadrant operation of a propeller [34]

The hydroydynamic pitch angle β is defined by:

$$\beta = \arctan\left(\frac{v_A}{0.7\pi \cdot n \cdot D}\right) \tag{3.10}$$

where n and v_a represent the rotational speed of the propeller and the propeller advance velocity. The propeller advance velocity as a result of the vessel roll motion is calculated by:

$$v_a = \dot{\phi}\sqrt{z_T^2 + y_T^2} + v_c \tag{3.11}$$

where z_T, y_T, $\dot{\phi}$ and v_c represent the vertical distance from the thruster centre to the CoG of the vessel, horizontal distance from the thruster centre to the CoG of the vessel, the roll velocity amplitude and the current velocity. An impression of a four-quadrant model is given in Figure 3.3.

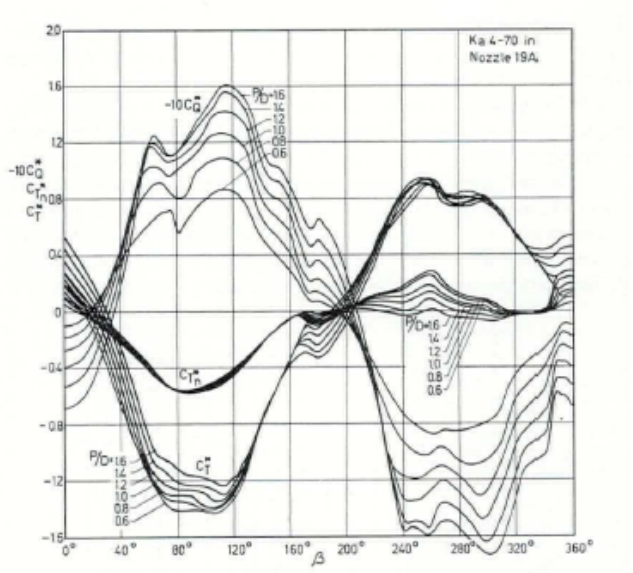

Figure 3.3: Four-quadrant diagram of Ka 4-70 thruster with different P/D ratios as found in Oosterveld [22]

The torque and thrust produced by the propeller are defined by:

$$Q_p(\beta, n) = C_Q(\beta)\rho\left(v_a^2 + (0.7\pi nD)^2\right)\frac{\pi}{8}D^3 \tag{3.12}$$

$$T_p(\beta, n) = C_T(\beta)\rho\left(v_a^2 + (0.7\pi nD)^2\right)\frac{\pi}{8}D^2 \tag{3.13}$$

The torque and thrust coefficients are approximated by using a 20-th order Fourier series:

$$C_Q(\beta) \approx \sum_{k=0}^{20}[A_Q(k)\cos(\beta k) + B_Q(k)\sin(\beta k)] \tag{3.14}$$

$$C_T(\beta) \approx \sum_{k=0}^{20}[A_T(k)\cos(\beta k) + B_T(k)\sin(\beta k)] \tag{3.15}$$

where A_Q, B_Q, A_T and B_T are Fourier coefficients based on experimental data. The values can be found in Appendix B.

The roll moment induced by the thruster is calculated by multiplying the produced thrust by the roll moment arm. The roll moment arm is defined according Rudaa [28] as the vertical distance between the thruster propeller centre and the centre of gravity of the vessel, see Appendix B.

To take into account the effect of thruster-hull interaction, the calculated open water thrust is reduced by applying a thrust deduction factor $t = 0.04$. This is the thrust deduction factor found by Wichers, [35] for an azimuth angle of 90°, see Appendix B.

3.3. Model verification

The dynamic thruster model has been applied to the azimuthing thrusters installed at the *Ndurance*. The stern thrusters are of the thruster type TH1500 and the forward thrusters are type TH1250. The thruster parameters of both types can be found in Appendix B. The results regarding thrust production are compared to manufacturer thruster curve data to ensure the validity of the modelling approach. Subsequently, the transient response of the thrusters is verified by expert indication.

3.3.1. Thruster curves

The implementation of the four-quadrant model is verified by comparing the thruster curves during different advance velocities as provided by the manufacturer with model output. The results are given in Figure 3.4.

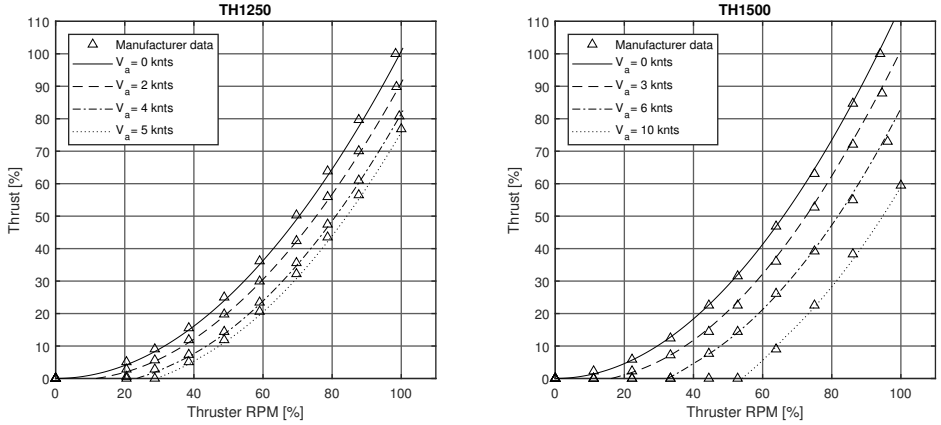

Figure 3.4: Model results for different advance velocities compared to manufacturer data for thruster type 1250 and 1500

As can be observed in Figure 3.4, the model output is in good agreement with the manufacturer data. To quantify the agreement, the relative mean absolute error between the model estimates and manufacturer data is calculated according Equation 2.16. The results are given in Table 3.3.

TH1250	RMAE [%]
V_a=0 knts	1.06
V_a=2 knts	0.81
V_a=4 knts	0.91
V_a=5 knts	0.91

TH1500	RMAE [%]
V_a=0 knts	0.48
V_a=3 knts	1.42
V_a=6 knts	0.76
V_a=10 knts	0.95

Table 3.3: RMAE values for thruster type TH1250 and TH1500 during different advance velocities

From Table 3.3 can be observed that the maximum RMAE value is 1.42%. This is considered sufficiently small to consider the mathematical model verified.

3.3.2. Transient response

The transient response of the thrusters is analyzed to asses whether the model is able to simulate realistic thruster behavior. In order to do so, a step impulse from 30% to 100% thrust is applied to the dynamic thruster model. The transient response of both thruster types is visualized in Figure 3.5.

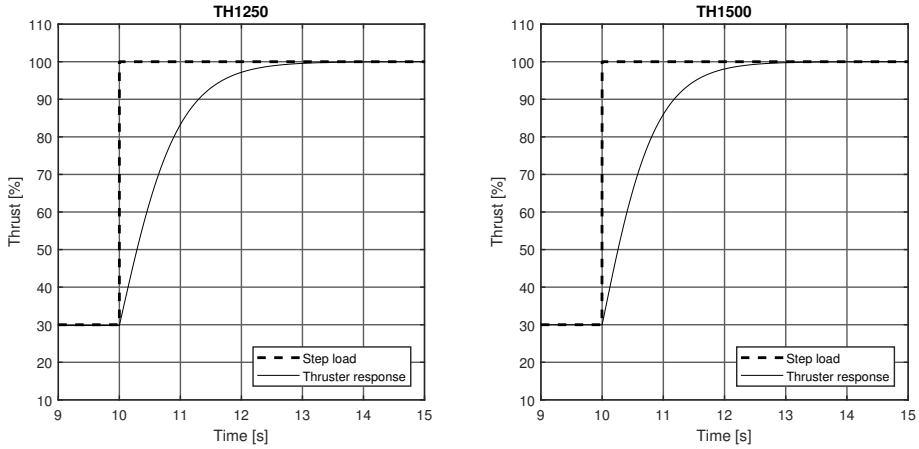

Figure 3.5: Transient response for thruster type 1250 and 1500 models

Figure 3.5 shows that both thrusters take around 3 seconds to ramp from 30% to 100% thrust. The behavior was hard to verify by literature, since no data was available for this specific thruster set-up. The Chief Engineer of the *Ndurance* estimated that it would take about 2 seconds for the thrusters to ramp from 30% to 100% thrust. This estimate is in agreement with the model results. Therefore, it is assumed that the model is able to simulate realistic dynamic thruster behavior.

3.4. Conclusions

The second sub-research objective is defined as:

"Develop a thruster model that captures the thruster dynamics in the time domain, this will include modeling of the thruster drive train system and thrust variations due to oscillating inflow velocities."

A dynamic thruster model is presented in this chapter. An empirical estimate of the entrained water added rotational inertia has been incorporated in the dynamic model to ensure conservatism. The thrust and torque produced by the thruster during oscillating inflow velocities is modelled by using a four-quadrant model.

From this research is concluded that:

- The four-quadrant thruster model thrust results have a maximum relative mean absolute error value of 1.42% when compared to manufacturer data. This error is considered sufficiently small to consider the mathematical model verified.

- The step load response of the dynamic thruster model is in line with the expectations of the *Ndurance* Chief Engineer. From this result is concluded that the thruster model is able to simulate realistic behavior.

4

DP System Model

In this chapter a DP system model is presented. The DP system model is developed in order to simulate the behavior of the DP system installed on board the *Ndurance*. By using this model it is possible to investigate the DP footprint, DP capability and thruster power consumption of the ship.

4.1. Introduction

The horizontal motions surge, sway and yaw as calculated by the time domain model are based on a body-fixed reference frame and earth-fixed reference frame. The vessel motions, velocities and accelerations are calculated in the body-fixed frame and are subsequently translated to the earth-fixed reference frame by using the rotation matrix:

$$\mathbf{R}(\psi) = \begin{bmatrix} \cos(\psi) & -\sin(\psi) & 0 \\ \sin(\psi) & \cos(\psi) & 0 \\ 0 & 0 & 1 \end{bmatrix} \tag{4.1}$$

The reference frames used in this report are illustrated in Figure 4.1. Also the orientation of the environmental directions is indicated.

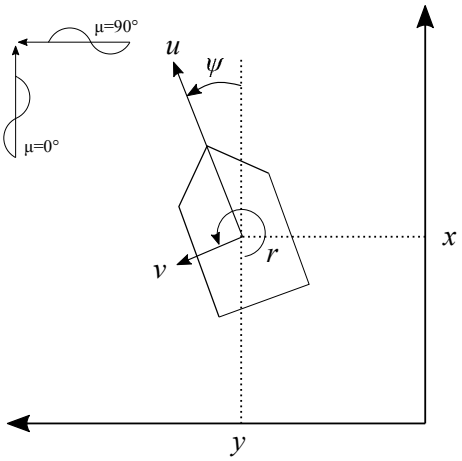

Figure 4.1: Definition of reference frames and environmental force direction

The *Ndurance* is equipped with a DP system. The DP system is a control system that enables the ship to maintain a specified position and heading when conducting operations in the offshore environment. The installed DP system on board the *Ndurance* uses 5 thrusters, of which 4 azimuthing thrusters and 1 tunnel thruster, to maintain its position and heading. The thruster lay-out is given in Figure 4.2.

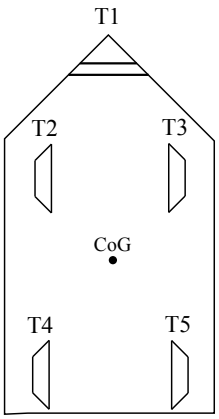

Figure 4.2: Schematic visualization of the thruster system lay-out of the *Ndurance*

In this chapter, the components out of which a DP system consists are explained. Next to this, an approach to model a DP system is presented and implemented. This modeling approach is largely based on the work of Serraris [31]. The chapter concludes with a verification of the constructed DP system model. This is done by comparing the model results to a DP time domain study conducted by MARIN.

4.2. DP system configuration

A DP system consist out of several components. In general, the main components are:

- Position and heading sensors
- Kalman filter, to filter out the first-order ship motions in the sensor signal
- DP Controller, to estimate the required thrust to ensure the ship maintains heading and position
- Allocation algorithm, to divide the required thrust over the available thrusters
- Thrusters, to produce the required thrust for station keeping

Since a mathematical model is constructed, the ship motions as a result of the environmental forces can not be observed by a sensor. Therefore, the sensor is left out and the calculated ship motions as explained in Chapter 2 are directly fed to the Kalman filter. A schematic overview of the DP system model is given in Figure 4.3.

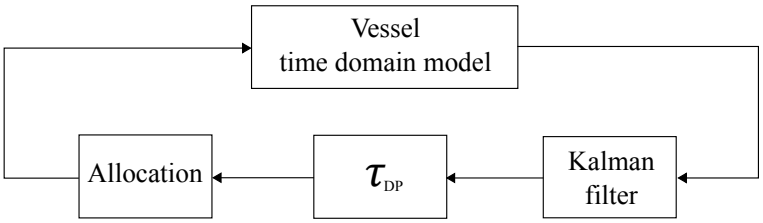

Figure 4.3: Schematic overview of DP system model

As can be observed in Figure 4.3, the symbol τ_{DP} is used to indicate the DP controller. In the upcoming sections, each system component of the DP system model and its modelling approach will be discussed.

4.3. Environmental forces

A ship in the offshore environment is subjected to forces and moments induced by waves, wind and current. Since a mathematical model is constructed, these forces and moment need to be generated numerically. For each component a model is presented.

4.3.1. Waves

The forces and moments induced by sea waves have two components: a first and a second-order component. The first-order wave forces and moments are oscillatory with a zero mean. The first-order wave forces result in first-order ship motions. These motions are those one experiences when sailing in a seaway. The first-order forces and moments are calculated in the time domain according Journée [20] by using:

$$F^1(t) = \sum_{n=1}^{N} \sqrt{2 \cdot S_{\eta,F}(\omega)\Delta\omega}\cos(\omega_n t + \epsilon_n + \epsilon_{\eta,F}) \tag{4.2}$$

in which:

N	=	total number of wave frequencies
ϵ_n	=	random phase angle in the domain [0 , 2π]
$\epsilon_{\eta,F}$	=	phase shift of the wave load
ω_j	=	wave frequency
$S_{\eta,F}(\omega)$	=	wave force response spectrum
t	=	time vector

The wave force response spectrum $S_{\eta,F}(\omega)$ is defined by the wave force RAO squared multiplied by a wave spectrum:

$$S_{\eta,F}(\omega) = \left|\frac{F_\eta}{\xi}(\omega)\right|^2 S_\xi(\omega) \tag{4.3}$$

The wave spectrum is defined by a JONSWAP spectrum as found in Journée [20]:

$$S_\xi(\omega) = \frac{320H_s^2}{T_p^4}\omega^{-5}\exp\left\{\frac{-1950}{T_p^4}\omega^{-4}\right\}\gamma^A \tag{4.4}$$

in which:

H_s	=	significant wave height
T_p	=	wave peak period
γ	=	3.3 (peak factor)
A	=	$\exp\left\{\left(\frac{\omega/\omega_p - 1}{\sigma\sqrt{2}}\right)^2\right\}$
σ	=	a step function of ω : if $\omega < \omega_p$ then $\sigma = 0.07$
		if $\omega > \omega_p$ then $\sigma = 0.09$

The second-order wave forces and moments arise from the square of the oscillatory components of the first-order wave components. This results in mean, high- and low-frequency wave forces and moments. The magnitude of these forces is smaller compared to the first-order wave forces. However, they can result in significant motions due to the low amount of damping at these frequencies and the fact that the frequency of these forces and moments can be near the low natural frequency of a moored ship. The mean component of the second-order wave force is commonly referred to as the mean drift force.

The low-frequency and mean wave drift forces in irregular waves are calculated according Newman [21] in the time domain by using:

$$F^2(t) = \sum_i \sum_j \xi_i \xi_j P_{ij}^- \cos((\omega_i - \omega_j)t + (\epsilon_i - \epsilon_j)) + \sum_i \sum_j \xi_i \xi_j Q_{ij}^- \sin((\epsilon_i - \epsilon_j)t + (\epsilon_i - \epsilon_j)) \quad (4.5)$$

in which:

ξ_i	=	i^{th} wave amplitude
ξ_j	=	j^{th} wave amplitude
ω_i	=	i^{th} wave frequency
ω_j	=	j^{th} wave frequency
P_{ij}^-	=	in-phase quadratic transfer function (QTF)
Q_{ij}^-	=	out-of-phase quadratic transfer function (QTF)
t	=	time vector

The mean components are calculated when $i = j$. Note that the high-frequency, or sum, components are not incorporated, since these forces and moments are considered negligible for a softly moored structure like a ship with a DP control system.

The QTFs Q^- and P^- are obtained from ANSYS AQWA. The panel method uses the far-field method to calculate the mean components of QTF and the near-field method to calculate the sum and difference components of the QTF. For a more elaborate review of both methods, see Journée [20].

4.3.2. Wind

The part of the ship that is not submerged is subjected to forces and moments induced by the wind. The wind forces and moments for surge, sway and yaw are calculated according to Serraris [31] by:

$$F_x = C_x(\mu)\frac{1}{2}\rho_a v_w^2 A_T \quad (4.6)$$

$$F_y = C_y(\mu)\frac{1}{2}\rho_a v_w^2 A_L \quad (4.7)$$

$$M_z = C_m(\mu)\frac{1}{2}\rho_a v_w^2 A_L L_{pp} \quad (4.8)$$

in which:

$C(\mu)$	=	wind load coefficient
μ	=	environmental direction
ρ_a	=	air density, typically 0.00125 ton/m^3
v_w	=	wind speed
A_T	=	frontal wind area
A_L	=	lateral wind area
L_{pp}	=	length between perpendiculars

In this environmental force model it is assumed that the wind speed is constant. The wind load coefficients can be obtained by conducting wind tunnel test or by the use of empirical models. The wind coefficients of the *Ndurance* are given in Appendix C.

4.3.3. Current

The submerged part of the ship is subjected to forces and moments induced by the water current. The environmental current force model for surge, sway and yaw are calculated in a similar approach as the

wind force as stated in Serraris [31]:

$$F_x = C_x(\mu)\frac{1}{2}\rho v_c^2 L_{pp} T \tag{4.9}$$

$$F_y = C_y(\mu)\frac{1}{2}\rho v_c^2 L_{pp} T \tag{4.10}$$

$$M_z = C_m(\mu)\frac{1}{2}\rho v_c^2 L_{pp}^2 T \tag{4.11}$$

in which:

$C(\mu)$	=	current load coefficient
ρ	=	sea water density, typically 1.025 ton/m^3
v_c	=	current speed
T	=	draft

Similar to the wind speed, it is assumed that the current speed is constant. The current load coefficients can be obtained by conducting wind tunnel test or by the use of empirical models. The current coefficients of the *Ndurance* are given in Appendix C.

4.4. Kalman filter

A Kalman filter is used in a DP system to filter out the first-order motions of the ship. The filtering is done in order to make sure that the thrusters do not respond to the high frequency motions. This would result in increased fuel consumption and wear and tear of the thrusters.
The benefits of a Kalman filter are minimum phase lag and the ability to continue estimation of a signal when the sensor signal is lost. The last property can prevent the DP system from a run-off in case of a sensor failure.

The Kalman filter estimates the vessel position by calculating the response of the ship according to its mass and the low-frequent excitation force. This force is derived from the measured thruster forces. The estimated response is compared to the measured response and a weighted portion of the difference between the position estimate and the measured position is added to the signal. The Kalman filter is based on a prediction-correction algorithm. First the prediction step is carried out as defined by Cadet [4]:

$$\begin{cases} \hat{x}_k = \mathbf{A}\hat{x}_{k-1} + \mathbf{B}u_k \\ \mathbf{P}_k = \mathbf{A}\mathbf{P}_{k-1}\mathbf{A}^T + \mathbf{Q} \end{cases} \tag{4.12}$$

in which:

$\hat{x}_k$	=	state that is estimated at timestep k
u_k	=	control input
$\mathbf{A}$	=	state transition matrix
$\mathbf{B}$	=	control input matrix
$\mathbf{P}_k$	=	error covariance matrix at timestep k
$\mathbf{Q}$	=	process noise covariance matrix

For every motion that is controlled by the DP system, a seperate Kalman filter has been implemented. In the report the yaw motion is described, but exactly the same approach has been used for the surge and sway motion. For the yaw motion, the estimated state vector, state transition matrix, control input

vector and process noise matrix become:

$$\hat{x}_k = \begin{bmatrix} \psi \\ \dot{\psi} \end{bmatrix} \tag{4.13}$$

$$u_k = \begin{bmatrix} 0 \\ M_z \end{bmatrix} \tag{4.14}$$

$$\mathbf{A} = \begin{bmatrix} 1 & \Delta t \\ 0 & 1 \end{bmatrix} \tag{4.15}$$

$$\mathbf{B} = \begin{bmatrix} 1 & 0 \\ 0 & \frac{1}{I_{yy}+a_{66}(\infty)} \end{bmatrix} \tag{4.16}$$

$$\mathbf{Q} = \begin{bmatrix} Q & 0 \\ 0 & Q \end{bmatrix} \tag{4.17}$$

In Equation 4.14, M_z represent the yaw moment induced by the thrusters. The Q term in Equation 4.17 represents the process noise covariance. This is a tuning parameter of the Kalman filter. A high Q value will put more emphasis on the measurement signal.

Next is the correction step:

$$\begin{cases} \mathbf{K}_k = \mathbf{P}_k\mathbf{H}^T(\mathbf{H}\mathbf{P}\mathbf{H}^T + \mathbf{R})^{-1} \\ \hat{x}_k = \hat{x}_k + \mathbf{K}_k(z_k - \mathbf{H}\hat{x}_k) \\ \mathbf{P}_k = (\mathbf{I} - \mathbf{K}_k\mathbf{H})\mathbf{P}_k \end{cases} \tag{4.18}$$

in which:

z_k	=	measurement signal
$\mathbf{K}_k$	=	Kalman gain
$\mathbf{H}$	=	mapping matrix from measurement to state
$\mathbf{I}$	=	2x2 identity matrix
$\mathbf{R}_k$	=	measurement noise covariance matrix

For the yaw motion, the measurement signal vector, mapping matrix and measurement noise covariance matrix become:

$$z_k = \begin{bmatrix} \psi \\ \dot{\psi} \end{bmatrix}_{measured} \tag{4.19}$$

$$\mathbf{H} = \begin{bmatrix} 1 & 0 \\ 0 & 1 \end{bmatrix} \tag{4.20}$$

$$\mathbf{R} = \begin{bmatrix} R & 0 \\ 0 & R \end{bmatrix} \tag{4.21}$$

In Equation 4.21, R represents the measurement noise covariance, which is also a tuning parameter. When the noise covariance is set at a high value, the Kalman filter puts less emphasis on the measurement signal.

The Kalman filter uses a recursive method to estimate the filtered signal. Therefore, it needs to be initialized with first estimates of the state and error covariance matrix. The measurement and process noise covariances are tuned manually to obtain the desired filter performance. Tuning of these parameters affect the over-all performance of the DP system. When the Kalman filter is tuned to be very responsive, the thruster response will also be responsive, resulting in a decreased DP footprint. More relaxed Kalman tuning parameters will cause the thrusters to react more slowly, but will also increase the DP footprint. DP operations like float-overs require a small DP footprint, where drilling ships or FPSOs allow a bigger DP footprint. Therefore, it is important to keep in mind the desired performance of the DP system when tuning the Kalman filter.

4.5. DP controller

After the Kalman filter has been applied, the position and heading signals are send to the DP controller. The DP controller consists out of 3 stand-alone closed loop PID controllers, responsible for controlling the surge, sway and yaw motions of the vessel. An schematic example of a standard closed-loop PID controller is given in Figure 4.4.

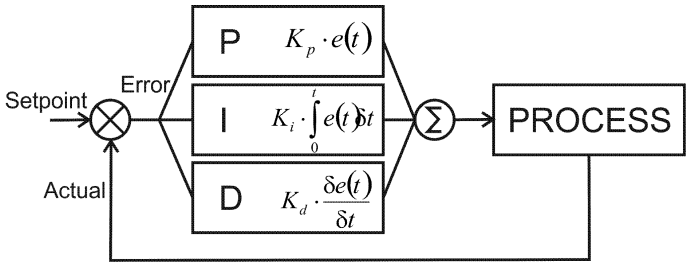

Figure 4.4: Block diagram of closed-loop PID controller

The PID controllers determine the total thrust in the horizontal plane required by the propulsion system to maintain position. The required thrust is calculated according to Serraris [31] by:

$$\tau_{DP} = K_p e + K_i \int_{\Delta t} e(t)dt + K_d \dot{e} \tag{4.22}$$

in which:

K_p	=	proportional coefficient vector
K_i	=	integral coefficient vector
K_d	=	derivative coefficient vector
e	=	position error vector

The position error is defined by:

$$e = \begin{bmatrix} x_s - x \\ y_s - y \\ \psi_s - \psi \end{bmatrix} \tag{4.23}$$

where x_s, y_s and ψ_s represent the surge, sway and yaw setpoint during the DP operation. The variables x, y and ψ represent the actual vessel position and heading. Note that the PID coefficients are vectors, since the coefficient value is not equal for each motion component. The proportional coefficient K_p determines the stiffness of the DP system. This is comparable to the spring stiffness of a mass-spring-damper system. The derivative K_d coefficient represents the damping of the DP system, likewise the damping term in a mass-spring-spring system. The integral term K_i is the integration coefficient. This coefficient enables compensation of the mean error offset of the system by integrating the error over time.

The P, I and D coefficients determine the behavior of the DP system. The coefficient values are tunable. Similarly to the tuning of the Kalman filter, it is important to keep in mind the desired performance of the DP system when tuning the PID coefficients. The initial values are often obtained by rule of thumb estimates and manually tuned to obtain the desired system behavior. Serraris [31] recommends the following rule of thumb estimates for the P and D coefficients:

$$P = \frac{N_t \cdot T_{max}}{(50 - 70\%)R_{max}} \tag{4.24}$$

$$D = (50 - 70\%) \cdot 2\sqrt{(M + a)P} \tag{4.25}$$

in which:

N_t	=	total number of thrusters
T_{max}	=	maximum thrust per thruster
R_{max}	=	maximum allowable horizontal excursion
M	=	ship mass
a	=	ship added mass

These rules of thumb provide a first estimate of the P and D coefficients. The I coefficient is often set to zero, since model tests showed that instability of the system might occur according Serraris [31]. Next to this, the mean offset, which is reduced by the I coefficient, can be neglected when one is interested in the station keeping accuracy of the DP system.

4.6. Thrust allocation

The total thrust in the horizontal plane as calculated by the DP controller is fed to a thrust allocation algorithm. Thrust allocation serves multiple purposes. The main purpose is to divide the required thrust over the available thrusters in such a way that the power consumption is minimized. Next to this, the thrust allocation algorithm also prevents thrusters from operating in so called 'forbidden zones'. Forbidden zones are the azimuth angles at which a thruster wake blows in the direction of a neighbouring thruster. When this happens, the efficiency of the downstream thruster is significantly reduced, which can result in a run-off of the DP system. Finally, the thrust allocation algorithm makes sure that the thrusters of the DP system are not overloaded, by making sure that no additional thrust is allocated to thrusters that have reached their saturation limit.

The thrust allocation algorithm tries to find the minimum of a objective function while satisfying both linear and non-linear constraints. The thrust allocation algorithm can be mathematically formulated by:

$$\begin{aligned} \underset{x}{\text{minimize}} \quad & F_0(x) \\ \text{subject to} \quad & c(x) \leq 0 \\ & \mathbf{A} \cdot x = b \end{aligned} \tag{4.26}$$

in which:

$F_0(x)$	=	objective function
x	=	unknown thrust vector in x- and y-direction
$c(x)$	=	vector with non-linear constraints
$\mathbf{A}$	=	matrix with linear constraints
b	=	required forces and moment in the horizontal plane

The objective function is defined as described in Serraris [31]:

$$F_0(x) = \sum_{i=1}^{N_{total}} \left| \frac{T_i}{T_{max}} \right|^2 + \sum_{i=1}^{N_{total}} w_i \left(\left(\frac{T_i}{T_{max}} \right)^2 - 1 \right)^2 \tag{4.27}$$

The last summation term is a penalty function that is included in the objective function when a thruster saturates. In that case $w_i = 10000$, else the value of w_i equals 0.

The total number of unknowns is calculated by:

$$N_{total} = 2N_{azi} + N_{bow} \tag{4.28}$$

In this equation N_{azi} represents the number of azimuth thrusters and N_{bow} the number of bow thrusters that are part of the DP system. Since an azimuth thruster can deliver thrust in both the x- and y-direction,

it contributes to 2 unknown thrust components. Since the *Ndurance* has 4 azimuth thrusters and 1 bow thruster, the total number of unknowns equals 9. The unknown thrust vector becomes:

$$x = \begin{bmatrix} T_{1y} \\ T_{2x} \\ T_{2y} \\ T_{3x} \\ T_{3y} \\ T_{4x} \\ T_{4y} \\ T_{5x} \\ T_{5y} \end{bmatrix} \tag{4.29}$$

In this vector, the term in the subscript corresponds to the thruster number and the thrust direction. The vector with non-linear constraints makes sure that the function is minimized without thruster overloading. The constraints are defined by:

$$c(x) = \begin{bmatrix} \sqrt{T_{2x}^2 + T_{2y}^2} - T_{2max} \\ \sqrt{T_{3x}^2 + T_{3y}^2} - T_{3max} \\ \sqrt{T_{4x}^2 + T_{4y}^2} - T_{4max} \\ \sqrt{T_{5x}^2 + T_{5y}^2} - T_{5max} \end{bmatrix} \tag{4.30}$$

Note that these constraints are non-linear due to the root term. The linear constraints matrix $\mathbf{A}$ is defined by Serraris [31]:

$$\mathbf{A} = \begin{bmatrix} 0 & 1 & 0 & 1 & 0 & 1 & 0 & 1 & 0 \\ 1 & 0 & 1 & 0 & 1 & 0 & 1 & 0 & 1 \\ x_{T1} & -y_{T2} & x_{T2} & y_{T3} & x_{T3} & -y_{T4} & -x_{T4} & y_{T5} & -x_{T5} \end{bmatrix} \tag{4.31}$$

The terms in the third row of $\mathbf{A}$ represent the thruster x- and y-position with regards to the centre of gravity of the ship. These terms have been added to calculate the moments created by each thruster. The required forces and moments in the horizontal plane that the thruster system has to realize to maintain position are captured in vector b:

$$b = \begin{bmatrix} F_{TX} \\ F_{TY} \\ M_{TZ} \end{bmatrix} \tag{4.32}$$

Vector b is directly fed from the DP controller and is used as the input variables of the allocation algorithm. The allocation algorithm uses the 'fmincon' Matlab function as solver. The mathematical background of the non-linear programming method, which forms the basis for the fmincon function, is elaborately discussed in Byrd [3].

The forbidden zones are taken into account by using a similar approach as proposed by Serraris [31]. The algorithm checks whether the solution contains azimuth angles located in a forbidden zone. When this is the case, the algorithm fixes the forbidden azimuth angle to the nearest boundary of the forbidden zone and reruns the allocation. This procedure is repeated until the solution satisfies the constraints and no azimuth angles are located in forbidden zones. The performance of the algorithm is checked by subjecting the vessel to environmental forces from 0° to 360°. The results are given in Appendix C.

The numerical values of the forbidden zones are given in Table 4.1.

Thruster	Forbidden zone [deg]
2	256.4 - 283.6
3	76.4 - 103.6
4	255.6 - 284.4
5	75.6 - 104.4

Table 4.1: Thruster azimuth angle forbidden zones

The allocation algorithm is executed during every time step. As a result of this, it is possible that the allocated azimuth angle differs significantly between two time steps. In reality a thruster is not able to switch its azimuth angle instantly. According to Serraris [31], it takes an azimuth thruster around 30 seconds to turn 360°. Therefore, the thruster rotation rate is limited to 12° per second.

4.7. Model verification

Now the building blocks of a DP system model have been constructed, the blocks are connected and merged into a complete DP system model. The constructed DP system model needs to be verified. This is done by comparing the model output to DP time domain simulations conducted by MARIN. MARIN uses its in-house developed simulator AnySim to conduct time domain DP simulations. The underlaying principles and assumptions of AnySim are presented in Serraris [31].

Three simulation cases have been selected for comparison. The selected cases are given in Table 4.2.

Case	Draft	$\mathbf{V_w}$	μ_w	$\mathbf{V_c}$	μ_c	$\mathbf{H_s}$	$\mathbf{T_p}$	μ_{H_s}	Spectrum
[#]	[m]	[m/s]	[deg]	[m/s]	[deg]	[m]	[s]	[deg]	[-]
1	4.7	12.86	45	1.286	45	2.0	5.7	45	JONSWAP
2	4.7	12.86	180	1.286	180	2.0	5.7	180	JONSWAP
3	4.7	12.86	90	1.286	165	2.0	5.7	165	JONSWAP

Table 4.2: Overview of simulation cases and corresponding environmental conditions for model verification

The ship, thruster and system tuning parameters used are given in Appendix C.
One should note that there exist many differences between the constructed DP model and the MARIN model. The differences considered the most significant are:

- **Kalman filter**, the MARIN model uses a coupled non-linear state transition model. Therefore, an Extended Kalman filter is used. The DP system model uses a linear Kalman filter. Next to this, it is unknown how the filter is tuned in the MARIN model.
- **Allocation algorithm**, the MARIN model uses a Lagrange multiplier method to solve the allocation problem, whereas the DP system uses a non-linear trust-region method to solve the allocation problem.
- **Ship motions**, it is unknown which motion coupling terms have been included in the MARIN model. Also, it is not known whether or not the MARIN model includes a viscous roll damping term.
- **Wave forces**, the calculation method of wave forces in the time domain that is used by the MARIN model is unknown.

The three selected cases have been simulated by the constructed DP system model. The mean, standard deviation, maximum value and minimum value of the calculated time signal of the ship motions, thrust and azimuth angles are given in Table 4.3, Table 4.4 and Table 4.5.

Case 1	**MODEL**				**MARIN**			
Motion	Mean	Std	Max	Min	Mean	Std	Max	Min
Surge [m]	0.46	0.12	0.69	-0.34	0.55	0.64	5.56	-1.13
Sway [m]	1.38	0.15	1.69	0.00	1.73	1.11	12.03	0.00
Heave [m]	0.00	0.05	0.19	-0.19	0.00	0.04	0.18	-0.15
Roll [deg]	0.00	0.18	0.65	-0.68	-0.11	0.26	1.03	-1.21
Pitch [deg]	0.00	0.27	1.11	-1.08	0.00	0.27	1.15	-1.08
Yaw [deg]	-0.51	0.15	0.09	-1.08	-0.66	0.79	3.28	-5.06
Thrust								
T1 [kN]	-25.01	4.94	0.00	-42.23	-42.79	9.37	0.69	-59.93
T2 [kN]	64.27	11.25	104.95	0.01	59.58	20.32	128.05	0.65
T3 [kN]	61.25	12.44	99.81	0.01	57.04	20.51	130.38	0.65
T4 [kN]	96.97	13.04	181.38	0.00	93.37	22.03	183.30	1.12
T5 [kN]	95.49	13.75	183.69	0.01	96.42	23.74	198.68	1.12
Azimuth								
T1 [deg]	0.00	0.00	0.00	0.00	0.00	0.00	0.00	0.00
T2 [deg]	-104.68	10.21	0.00	-141.98	-116.68	5.19	0.00	-152.22
T3 [deg]	-107.79	9.87	0.00	-136.44	-109.97	3.90	0.00	-147.53
T4 [deg]	-106.79	13.80	0.00	-148.16	-106.38	6.29	0.00	-167.86
T5 [deg]	-110.24	13.94	0.00	-165.32	-103.69	8.42	63.15	-155.78

Table 4.3: Comparison of simulation results for case 1

Case 2	**MODEL**				**MARIN**			
Motion	Mean	Std	Max	Min	Mean	Std	Max	Min
Surge [m]	-0.488	0.064	0.001	-0.659	-0.697	0.439	0.210	-2.997
Sway [m]	0.000	0.000	0.002	0.000	0.000	0.021	0.481	-0.216
Heave [m]	0.000	0.038	0.121	-0.132	0.000	0.057	0.211	-0.212
Roll [deg]	0.000	0.000	0.000	0.000	0.000	0.002	0.097	-0.037
Pitch [deg]	0.000	0.161	0.636	-0.681	-0.002	0.205	0.839	-0.895
Yaw [deg]	0.072	0.007	0.077	0.000	-0.005	0.035	0.462	-0.630
Thrust								
T1 [kN]	-0.827	0.062	-1.056	0.000	0.007	0.613	11.220	-17.300
T2 [kN]	19.256	5.670	60.718	0.004	27.201	5.601	57.101	-2.200
T3 [kN]	18.733	5.663	60.344	0.004	27.201	5.598	56.571	-2.200
T4 [kN]	34.142	10.106	107.947	0.004	23.596	5.337	51.772	-4.006
T5 [kN]	35.193	10.095	107.292	0.004	23.596	5.331	51.409	-4.006
Azimuth								
T1 [deg]	0.000	0.000	0.000	0.000	0.000	0.000	0.000	0.000
T2 [deg]	-0.109	0.155	-0.019	-3.142	0.008	4.567	179.892	-178.233
T3 [deg]	-0.112	0.156	-0.019	-3.142	0.008	4.567	179.892	-178.223
T4 [deg]	0.069	0.129	3.096	0.000	-0.007	4.594	179.861	-178.264
T5 [deg]	0.072	0.130	3.097	0.000	-0.007	4.593	179.861	-178.264

Table 4.4: Comparison of simulation results for case 2

Several conclusions can be drawn from the comparison of the results given in Table 4.3, Table 4.4 and Table 4.5. First the ship motion results are considered. Next, the thrust results and finally the resulting azimuth angles.

Ship motion
The mean values of the ship motions are in good agreement for all cases. The maximum deviation is 0.35 meter, which is considered negligible for a ship with a length of 99 meters. From this can be concluded that the mean environmental forces, caused by the wave drift force, wind force and current force are generally in agreement in both models. However, the standard deviation, maximum and minimum

Case 3	**MODEL**				**MARIN**			
Motion	Mean	Std	Max	Min	Mean	Std	Max	Min
Surge [m]	-0.272	0.085	0.111	-0.561	-0.299	0.501	2.045	-1.941
Sway [m]	1.340	0.143	1.555	0.000	1.680	0.320	3.294	0.000
Heave [m]	0.000	0.038	0.118	-0.112	0.000	0.057	0.218	-0.211
Roll [deg]	0.000	0.068	0.279	-0.291	-0.093	0.110	0.333	-0.567
Pitch [deg]	0.001	0.169	0.568	-0.574	-0.001	0.202	0.839	-0.841
Yaw [deg]	0.252	0.062	0.425	-0.097	0.240	0.292	1.777	-0.671
Thrust								
T1 [kN]	-30.291	3.734	0.404	-49.928	-41.585	1.988	1.125	-44.542
T2 [kN]	73.299	8.520	117.535	0.000	62.892	7.312	109.486	0.000
T3 [kN]	62.497	8.015	104.139	0.000	62.988	7.474	108.111	0.000
T4 [kN]	65.557	9.890	101.525	0.000	61.683	7.676	106.247	0.000
T5 [kN]	60.118	9.224	95.373	0.000	62.223	7.710	107.740	0.000
Azimuth								
T1 [deg]	0.000	0.000	0.000	0.000	0.000	0.000	0.000	0.000
T2 [deg]	-79.771	15.960	0.000	-179.332	-80.487	6.275	0.000	-106.470
T3 [deg]	-82.344	18.119	0.000	-179.259	-75.329	2.418	0.000	-103.600
T4 [deg]	-80.045	18.675	0.000	-153.712	-81.033	6.065	0.000	-102.928
T5 [deg]	-80.059	19.265	0.000	-153.722	-75.001	2.081	0.000	-104.400

Table 4.5: Comparison of simulation results for case 3

value of the calculated ship motions differs significantly. The tuning of the Kalman filter, simulation time and initial conditions can be reasons for these deviations. In case 1, a drift-off of 12 meters in the sway direction is observed in the MARIN results. This would be unacceptable during a real DP operation. The DP model shows much lower maximum and minimum values, resulting subsequently in a lower standard deviation.

Thrust
In general the mean thrust values are in good agreement. However, the MARIN model allocates significantly more thrust to the bow thruster. The reason is unknown, but probably this is the result of a different allocation algorithm. During case 2, the MARIN model allocates more thrust to the forward thrusters compared to the aft thrusters. This is unexpected, since the aft thrusters have a bigger thrust capacity and it is therefore powerwise more efficient to use the aft thrusters to compensate the head waves, wind and current. The DP model behavior is more as expected.

Azimuth angles
The mean azimuth angles are generally in agreement. However, the standard deviations tend to deviate. During case 2, the MARIN model has a significant higher standard deviation, whereas the DP model shows higher standard deviations during the other cases. Reasons for this different behavior could be the Kalman filter tuning and the different allocation algorithm.

To quantify the agreement between both models, the RMAE value of the horizontal motions and the thrust and azimuth angle mean estimates are calculated. The results are given in Table 4.6.

Parameter	**RMAE [%]**
Surge	8.7
Sway	13.3
Yaw	8.7
Thrust	6.7
Azimuth	2.1

Table 4.6: RMAE values for model results compared to MARIN results

4.8. Conclusions

The third sub-research objective is defined as:

"Develop a simulation model that is able to simulate DP system behavior, this includes modelling of the DP system and environmental forces."

A DP system model consisting out of a Kalman filter, DP controller and a thrust allocation algorithm is developed. The DP model is merged with the vessel time domain model. Different models to calculate the environmental forces due to wind, waves and current are presented.

From this research is concluded that:

- The developed DP model is able to simulate stable DP station keeping.
- The maximum relative mean absolute motion error when the simulation results are compared to MARIN simulations is 13.3% for the mean sway motion. This error is equal to 0.35 m in the sway direction, which is considered acceptable.
- The relative mean absolute error of the thrust and azimuth angle mean simulation results, when compared to MARIN data, is respectively 6.7% and 2.1%. This is considered acceptable.
- The significant differences in standard deviation, maxima and minima between the constructed DP model and the MARIN model are most probably the result of different Kalman filter tuning coefficients and a different thrust allocation algorithm.
- The developed DP system model merged with the environmental force models and the vessel time domain model is able to simulate DP system behavior.

5
3DP System Model

In this chapter, a novel control model is proposed for combined thruster induced roll reduction and DP station keeping. Also, the tuning procedure of the controllers is discussed.

5.1. Introduction

The main objective of this research is to investigate whether it is possible to reduce the significant roll amplitude of the *Ndurance* in beam seas during DP operations by active control of the thrusters. Koschorrek et al. [17] proposed a method to combine DP and roll control for a vessel equipped with Voith Schneider propellers. Sørensen and Strand [33] and Xu et al. [36] proved that it is possible to actively damp the unintentional roll-pitch motion induced by the DP system of a semi-submersible. The proposed control algorithm also increased the DP position keeping performance. A combined control model for first-order roll reduction combined with DP station keeping using conventional thrusters has not been investigated to the best of the author's knowledge.

The development of such a control model is presented in this chapter. In the previous chapters, models to calculate the vessel motions, thruster response and DP system behavior have been presented. These models combined provide a mathematical playground, which is used to develop and implement a novel control model system that is able to combine DP station keeping and active roll reduction. A general control structure is proposed and a novel allocation approach is presented. Also, the tuning of the control systems in the model is discussed.

5.2. Conventional DP control system vs. 3DP control system

To achieve DP station keeping and active roll reduction combined, a new control model needs to be implemented. The differences between a conventional DP control system and the anti-roll control system are summarized in Table 5.1.

	DP control system	**3DP control system**
System objective	station keeping	roll reduction and station keeping
System application	all conditions	beam seas
Controlled motions	x,y,ψ	x,y,ψ, ϕ
Controller bandwith	low frequency	high frequency
Allocation objective	power minimization	roll reduction maximization

Table 5.1: Differences between a conventional DP model and the 3DP model

From Table 5.1 can be observed that in order to develop an anti-roll control system, the allocation and controller part of a conventional DP control system needs to be adapted. The newly proposed allocation and controller models are presented in the following sections.

5.3. Allocation model

In a conventional DP system, the allocation algorithm allocates the required thrust to the available thrusters in such a way that the thruster power consumption is minimized. During active roll reduction, allocation based on minimization of power consumption is not applicable anymore, since a lot of thruster power will be used to achieve roll reduction. Therefore, a new allocation method is proposed to enable both roll reduction and station keeping.

5.3.1. Roll reduction

Rudaa [28] proposes to use thruster pairs to counteract the wave induced roll moment. When the thruster pairs are fixed pointing in opposing direction, this yields three main advantages:

- Yaw stability, when the thruster pair consist out of a forward and aft thruster, the yaw moments induced by both thrusters are balanced.
- Sway stability, when both a port side and starboard thruster pair is used, the sway motion induced by the port side thruster pair is balanced by the starboard thruster pair.
- No thruster interaction, since the thruster wakes are pointed away from each other, there is no possibility of thruster-thruster interaction

A schematic visualization of the thruster pairs and wave direction is given in Figure 5.1.

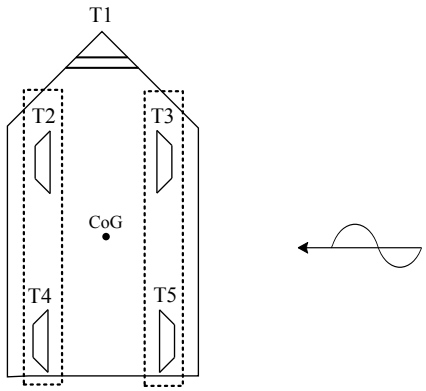

Figure 5.1: Thruster pair configuration 3DP control model for roll reduction

The first thruster pair consist out of T2 and T4. The second thruster pair consist out of T3 and T5. As can be observed from Figure 5.1, no thruster-thruster interaction can occur, since all thruster wakes are pointed away from each other. To obtain maximum roll reduction, the thruster pairs need to work in anti-phase. This means that when thruster pair 1 is ramping up to counteract the wave induced roll moment, thruster pair 2 is ramping down. This method of operation also ensures yaw and sway stability, since the averaged yaw moment and sway force produced by both thruster pairs over time equals zero when operating perfectly in anti-phase. The allocation vector $\mathbf{H}_1$ is used to indicate which thrusters are used for roll reduction:

$$\mathbf{H}_1 = \begin{bmatrix} 0 \\ 1 \\ 1 \\ 1 \\ 1 \end{bmatrix} \tag{5.1}$$

From $\mathbf{H}_1$ can be observed that all azimuthing thruster are used for roll reduction purposes.

5.3.2. Station keeping

Next to roll reduction, the thrusters are also used for station keeping. In beam waves, the wave forces that need to be counteracted by the control model are mainly in the sway direction. Since thruster T2 and T4 are already pointed in the direction of the incoming wave force, it is a logical approach to use these thrusters for station keeping in the sway direction.

The yaw motion is controlled by the bow thruster, this makes sense since this thruster has a long yaw moment arm and is not used for roll reduction purposes. Therefore, the complete thruster capacity can be used to control the yaw motion.

Since all thrusters are aligned in the sway direction, compensation of environmental forces in the surge direction is not possible. To solve this problem, the azimuth angles of the thrusters used for surge control are controlled by an azimuth controller. Thruster T3 is used for compensation of positive surge

forces and thruster T5 is used to compensate negative surge forces. A schematic visualization of the thrusters used for station keeping is given in Figure 5.2.

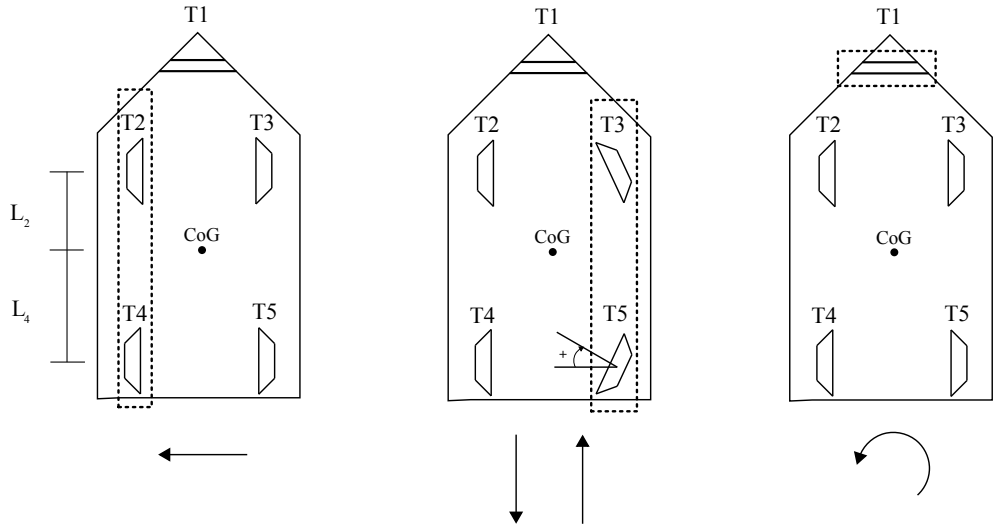

Figure 5.2: Thruster configuration 3DP control model for station keeping (sway, surge and yaw motion)

The allocation vector $\mathbf{H}_2$ is used to indicate which thrusters are used to control the surge, sway and yaw motions:

$$\mathbf{H}_2 = \begin{bmatrix} 0 & 0 & 1 \\ 0 & \frac{L_2}{L_2+L_4} & 0 \\ X_3 & 0 & 0 \\ 0 & \frac{L_4}{L_2+L_4} & 0 \\ X_5 & 0 & 0 \end{bmatrix} \tag{5.2}$$

where L_2 and L_4 represent the thruster moment arms of respectively thruster T2 and thruster T4, see Figure 5.2. X_3 and X_5 represent two Boolean variables defined by:

$$X_3 = \begin{cases} 1 & \text{if } T_x \leq 0 \\ 0 & \text{otherwise} \end{cases}$$

$$X_5 = \begin{cases} 1 & \text{if } T_x > 0 \\ 0 & \text{otherwise} \end{cases}$$

where T_x represent the required thrust in the surge direction to maintain position as calculated by the surge DP controller. Allocation matrix $\mathbf{H}_2$ indicates that thruster T1 is used for yaw control. The required thrust in the sway direction is divided over thruster T2 and T4. The division is done according the thruster yaw moment arms. By doing so, the yaw moment of both thruster is balanced and no resulting yaw moment is induced. Negative thrust in the surge direction is delivered by T2, whereas T5 delivers positive thrust in the surge direction when required.

5.4. Controllers

The proposed control model consist out of a high-level motion controller and low-level shaft speed and azimuth angle controllers. The control structure is schematically visualized in Figure 5.3.

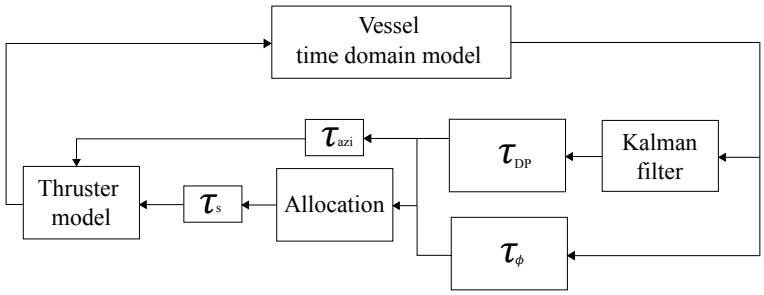

Figure 5.3: 3DP control model structure

In this section the high-level motion controllers and the low-level shaft speed controller and azimuth angle controller are discussed.

5.4.1. Roll reduction

The purpose of the anti-roll controller is to actively reduce the roll motion of the vessel. The high-level motion controller therefore needs to counteract the first-order roll moment induced by the waves. The controller output is a thruster RPM command, since this is the input set point variable for the low-level shaft speed controller. Rudaa [28] proposes to use a non-linear proportional derivative (PD) type controller:

$$\tau_\phi = -K_p \text{sign}(\dot{\phi}) \sqrt{\frac{|\dot{\phi}|}{c}} - K_d \ddot{\phi} \tag{5.3}$$

where K_p, c and K_d represent the proportional coefficient, a tuning parameter and the derivative coefficient. Rudaa [28] includes the non-linear square root term to make sure the contribution from the thrusters is equally large for all roll rates. Also the thrusters are limited to a specific limit, to increase their reaction time. Systematic numerical simulations are carried out to analyze the influence of the tuning coefficients and the thruster limits.

Tuning coefficients

In order to analyze the influence of the coefficients K_P, c and K_D onto the controller performance, systematic numerical simulations have been carried out with different tuning coefficients at one particular sea state. The selected simulation cases and corresponding tuning coefficients are visualized in Figure 5.4.

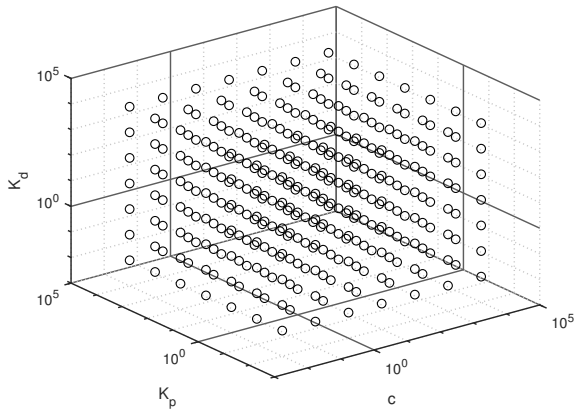

Figure 5.4: Selected search space for controller tuning coefficients in range [0.01 10000], $H_s = 0.5$m and $T_p = 8.5$s

The roll reduction for every simulation case is calculated by subtracting the RMS value of the roll angle time trace with active roll reduction by the RMS value of the roll angles without active roll reduction. The RMS value of the roll angle time trace is calculated by:

$$\phi_{RMS} = \sqrt{\frac{1}{n}(\phi_1^2 + \phi_2^2 + \ldots + \phi_n^2)} \tag{5.4}$$

where n is the total number of samples and ϕ is the roll angle amplitude.

To determine the sensitivity of the tuning parameters to the roll reduction, the maximum partial derivative of the RMS reduction is calculated with respect to every tuning coefficient in the calculated range:

$$\frac{\partial RMS}{\partial c} \qquad \frac{\partial RMS}{\partial K_p} \qquad \frac{\partial RMS}{\partial K_d}$$

The other tuning parameters are considered equal 1 when calculating the partial derivatives. The result is given in Figure 5.5.

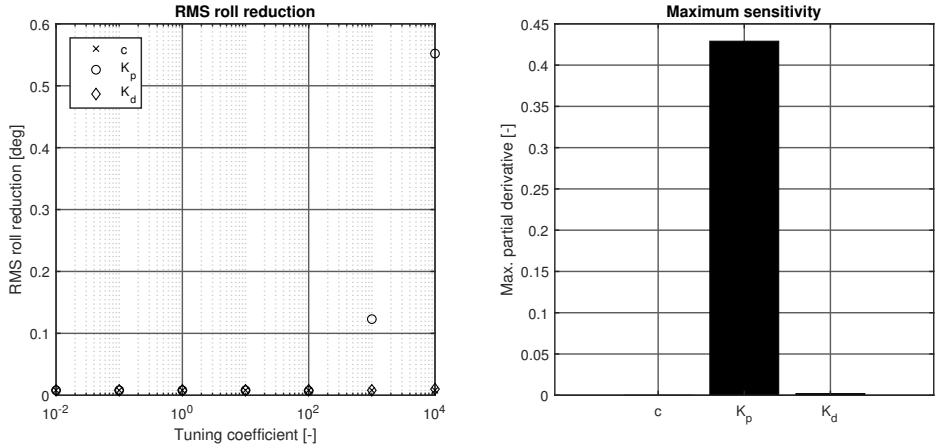

Figure 5.5: Roll reduction for different tuning coefficients and maximum sensitivity of every tuning coefficient (H_s = 0.5m and T_p = 8.5s)

As can be observed in Figure 5.5, the effect of the tuning variables c and K_d is of a negligible magnitude in the current controller model. The roll reduction depends on K_p solely, therefore it is decided to use a much more simplified proportional anti-roll controller τ_ϕ defined by:

$$\begin{aligned} \tau_\phi &= K_p \dot{\phi} \\ \tau_{min} &\leq \tau_\phi \leq \tau_{max} \end{aligned} \tag{5.5}$$

where τ_{min} and τ_{max} represent the thruster RPM limits. In order to analyze the optimum value of the controller proportional coefficient K_p, systematic numerical simulations have been carried out for three different sea states and increase values of K_p. The magnitude of the roll reduction is quantified by calculating the relative roll reduction (RRR):

$$RRR = \frac{\phi_{RMS1} - \phi_{RMS2}}{\phi_{RMS1}} \tag{5.6}$$

where ϕ_{RMS1} is the RMS value of the roll angle time trace without active roll reduction and ϕ_{RMS2} is the RMS value of the roll angle time trace with roll control activated. The results are given in Figure 5.6.

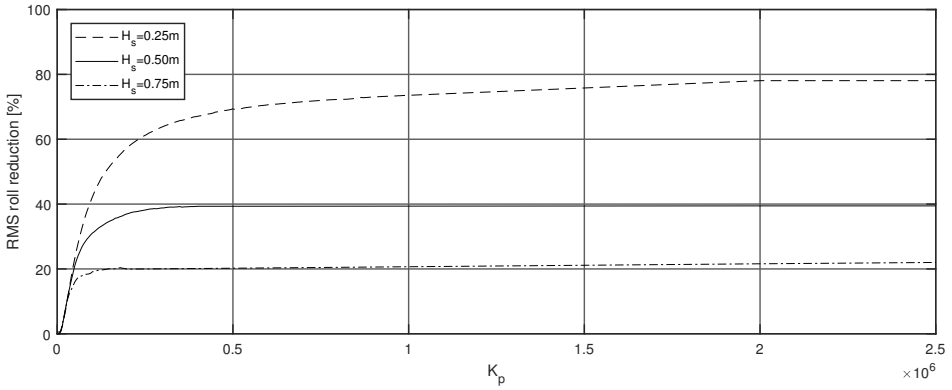

Figure 5.6: Roll reduction percentage for different K_p values ($T_p = 8.5$s)

From Figure 5.6 can be observed that the roll reduction percentages converge to a constant value when the coefficient K_p increases. As can be derived from Figure 5.6, the roll reduction percentage converges quicker for a high sea state. This can be explained by the fact that controller reaches the saturation limit τ_{max} earlier as a result of the higher roll velocities during increased environmental loads. On the basis of these results, it is decided to use a controller coefficient of a value of $K_p = 2.5 \cdot 10^6$, since at this value, the roll reduction has been converged to a maximum value for all sea states.

Thruster limits

The thruster RPM is limited to a maximum and a minimum value. The maximum RPM value is incorporated to avoid overloading the thruster above its maximum rated RPM. The minimum RPM is included to increase the response time of the thruster. Ramping up a thruster from 0% RPM to 90% RPM takes more time then, for example, ramping from 15% RPM to 90% RPM. See Figure 5.7.

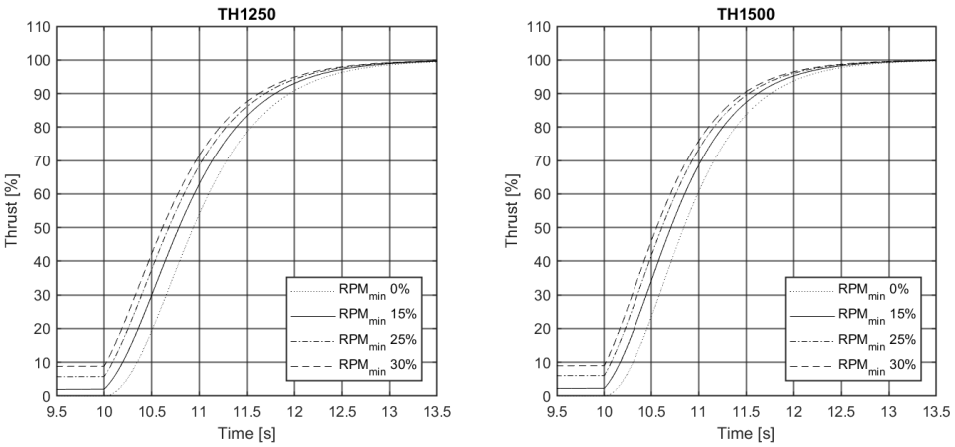

Figure 5.7: Response time of thruster TH1250 and TH1500 for different minimum limit RPMs

On the other hand, increasing the minimum RPM of the thruster will decrease the magnitude of the counteracting roll moment that a thruster pair can realize. This is the result of the thruster pair that is working in anti-phase at a particular minimum RPM, decreasing the net counteracting roll moment. Therefore, there exist a trade-off between thruster response time and the minimum thruster RPM variable. To investigate the optimum minimum thruster RPM limit, systematic numerical simulations have been carried out for different minimum RPM limits and sea states. The results are given in Figure 5.8.

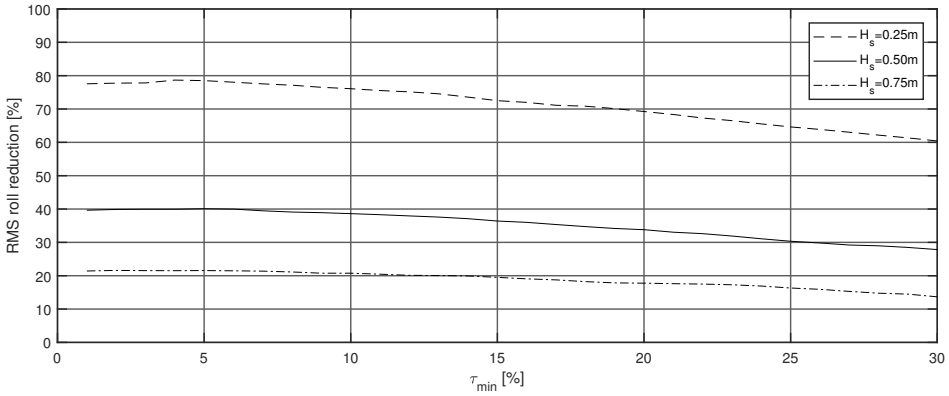

Figure 5.8: Roll reduction percentage for different τ_{min} as percentage of τ_{max} (T_p = 8.5s)

Figure 5.8 indicates that the optimum lower limit of the thruster RPM is 5% for all three sea states. A clear trend is visible that when the lower RPM limit is increased, the roll reduction percentage decreases. This is as expected, since the net counteracting roll moment produced by the thruster pairs is decreased. In the simulations, the lower RPM limit τ_{min} is set at 5% of τ_{max}.

5.4.2. Station keeping

The controller design for DP station keeping is based on the conventional PID controller structure as proposed by Serraris [31]. However, this controller output is a thrust command. Since the controller structure is based on RPM as control variable, the DP station keeping controller thrust estimate is transformed to a RPM command by:

$$\tau_{DP,RPM} = \frac{1}{0.7\pi D}\sqrt{\frac{\tau^*_{DP,T}}{\frac{\pi}{8}D^2 C_T \rho} - v_a^2} \tag{5.7}$$

where $\tau^*_{DP,T}$ represents the thrust-based controller as described in the previous chapter.

The next step is to combine the output of the roll controller and station keeping controller. This is done by using the allocation matrices $\mathbf{H}_1$ and $\mathbf{H}_2$:

$$\begin{aligned} \tau &= \mathbf{H}_1\tau_\phi + \mathbf{H}_2\tau_{DP} \\ \tau_{min} &\leq \tau \leq \tau_{max} \end{aligned} \tag{5.8}$$

By using this approach, the high-frequency roll controller and the low-frequency DP controller are combined. The principle is schematically visualized in Figure 5.9.

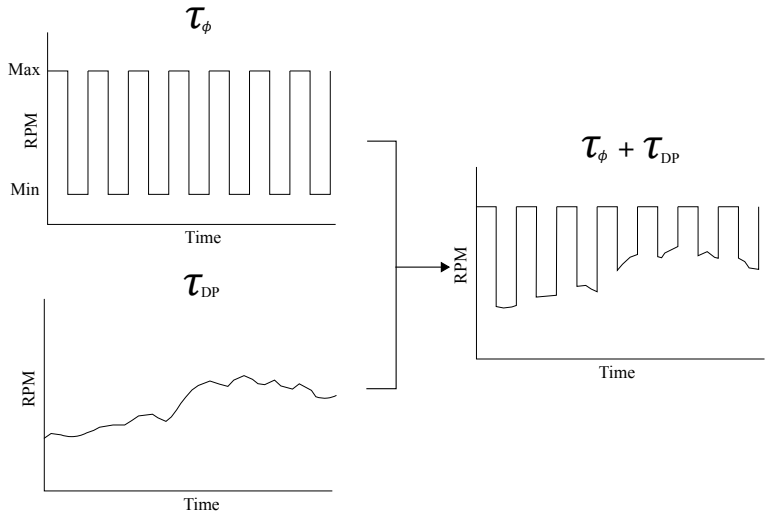

Figure 5.9: 3DP control system high-level motion control principle

As can be observed from Figure 5.9, the high- and low-frequency controller signal are combined into one. In this way, the controller ensures that both the second-order mean wave drift, wind, current forces and the first-order roll moment are counteracted.

5.4.3. Azimuth angle

Since all thrusters pairs are aligned in the sway direction to achieve maximum roll reduction, compensation of environmental forces in the surge direction is not possible. In beam waves, the wave forces acting on the vessel in the surge direction are negligible. However, the wind and current can induce significant forces in the surge direction, since these forces can differ from the wave direction. To increase the station keeping capability of the vessel in these conditions, the azimuth angle of the thrusters used for surge motion control are rotated by an angle as can be seen in Figure 5.2. There are two different methods to determine the azimuth angle:

- Static method, in which fixed azimuth angles are used.
- Dynamic method, in which the azimuth angles are dependent on a particular variable.

First, the optimum static azimuth angles resulting in maximum roll reduction are determined by conducting systematic simulations. During these simulations, the environmental forces induced by wind

and current are varied between $0°$ and $180°$ with a constant interval of $30°$. The wave forces are always beam on. The azimuth angles are varied in the interval $[0°, 20°]$ for thruster T3 and $[0°, -30°]$ for thruster T5. The optimum azimuth angles per direction are shown in Figure 5.10.

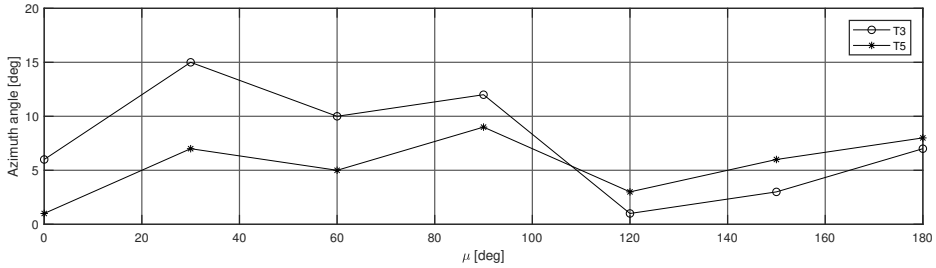

Figure 5.10: Optimum azimuth angle resulting in maximum roll reduction (H_s = 0.5m and T_p = 8.5s)

From Figure 5.10 can be observed that the optimum azimuth angles vary significantly per environmental direction. Next to this, one can see that the magnitude of the azimuth angle of T3 is bigger compared to T5 in the first quadrant ($0° - 90°$) and vice versa in the second quadrant ($120° - 180°$). This is the result of the fact that thruster T3 is used to counteract positive environmental forces and T5 is used to counteract negative environmental forces in the surge direction. From both observations is concluded that a static method is not suitable to determine the azimuth angles of the thruster used for surge motion control. A static method, where the azimuth angles are fixed to a specific value, does not yield maximum roll reduction and more importantly, is not able to adapt to changing environmental conditions.

The dynamic method is based on the idea that the azimuth angles need to be controllable in order to adjust to changing environmental conditions. It was observed that there exist a relation between the DP controller mean thrust command in the surge direction and the RMS of the roll angle time trace, see Figure 5.11.

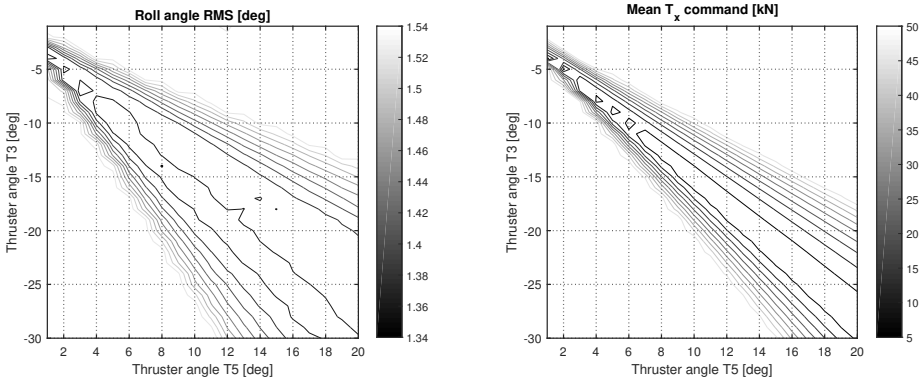

Figure 5.11: Azimuth angles for T3 and T5 vs. roll angle RMS and mean T_x command (H_s = 0.5m and T_p = 8.5s, $\mu = 60°$)

From Figure 5.11 can be observed that there exist a relation between the roll angle RMS and the mean T_x command of the DP controller. When the mean T_x command is minimum, the roll angle RMS is also at a low value. Therefore, it is decided to minimize the DP controller T_x command by using a proportional controller:

$$\tau_{azi} = K_p e_{azi} \tag{5.9}$$

where e_{azi} is defined by:

$$e_{azi} = 0 - T_x \tag{5.10}$$

By using a proportional azimuth angle controller, the controller behaves similar to a mechanical spring, adjusting the azimuth angle when the environmental load increases. There is no mean offset or damping term that has to be included in this controller, since the azimuth angle controller is intended purely

proportional. Therefore, no K_i and K_d terms are included. To verify the behavior of the controller, the average azimuth angles per environmental direction are visualized in Figure 5.12.

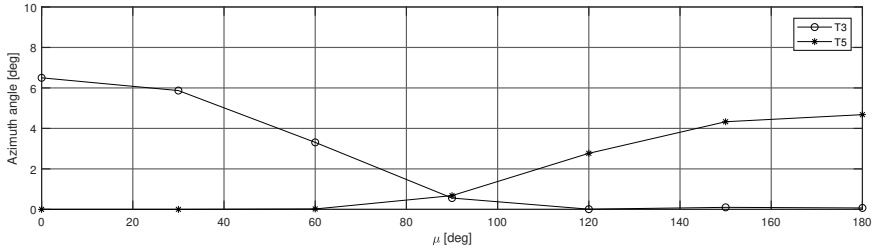

Figure 5.12: Mean azimuth angles for T3 and T5 per environmental direction ($H_s = 0.5$m and $T_p = 8.5$s)

From Figure 5.12 can be observed that the mean azimuth angles resulting from the proportional azimuth controller show behavior as expected. The azimuth angles of T3 are bigger compared to T5 for positive environmental forces in the surge direction. The opposite applies for T5 during negative environmental forces in the surge direction. By implementing this type of azimuth angle controller, the control system is able to counteract significant environmental loads in the surge direction and is able to counteract the change in environmental loads.

The proposed azimuth angle controller is tuned by conducting systematic simulations per environmental direction and different values for K_p. The results are given in Figure 5.13.

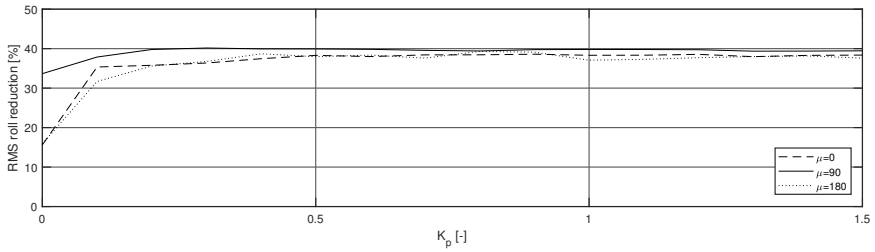

Figure 5.13: Roll reduction percentage for three environmental directions and tuning coefficients K_p ($H_s = 0.5$m and $T_p = 8.5$s)

From Figure 5.13 can be observed that the RMS roll reduction converges for increasing K_p coefficient values. The roll reduction percentages of every environmental direction are averaged and the K_p coefficient which result in the highest averaged roll reduction percentage is selected. This resulted in a value of $K_p = 0.9$. A typical time trace of the surge, sway and yaw motions of the 3DP model is given in Appendix D.

5.4.4. Shaft speed

The shaft speed controller is in place to keep the shaft speed equal to the required shaft speed as determined by the high-level motion controllers. According Leonhard [18], a proportional-integral (PI) controller is considered the most appropriate type for electrical motor control. Also Smogeli [32] proposes a PI controller for shaft speed control. Therefore, a PI controller is implemented to control the shaft speed:

$$\tau_s = Q_{cm} = K_p e_s + K_i \int_0^t e_s(t)dt \tag{5.11}$$

where Q_{cm} and e_s represent the commanded motor torque and shaft speed error calculated by:

$$e_s = \tau - n \tag{5.12}$$

where τ and n represent the requested shaft speed by the high-level motion controller and the actual shaft speed.

A first estimate of the tuning parameters K_p and K_d is obtained by using the approach as formulated by Smogeli [32]:

$$K_p = k_p \frac{k_g Q_N}{n_{bp}} \tag{5.13}$$

$$K_i = \frac{K_p}{T_i} \tag{5.14}$$

$$T_i = k_t T_{sum} \tag{5.15}$$

where k_p, Q_N, n_{bp}, k_t and T_{sum} represent a tuning parameter in the domain $[5, 10]$, the propeller torque, shaft speed at bollard pull condition, a tuning parameter ≥ 4 and a time constant defined by:

$$T_{sum} = T_m + T_f \tag{5.16}$$

where T_m and T_f represent the motor time constant and the shaft speed constant. The model is manually tuned to achieve desired controller behavior. The tuning coefficients are given in Appendix D. The performance of the shaft speed controller for the thruster type TH1250 is visualized in Figure 5.14.

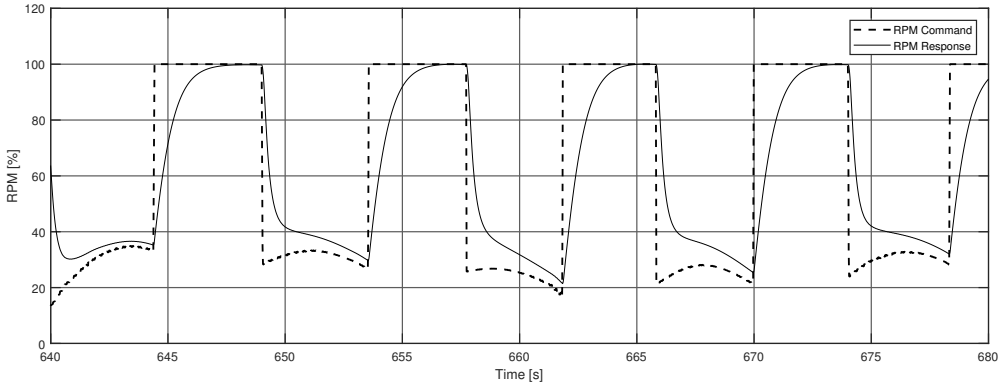

Figure 5.14: Commanded RPM signal and actual RPM behavior of T3

As can be observed from Figure 5.14 the shaft speed controller performs as desired. No RPM overshoot and oscillatory behavior is observed.

5.5. Conclusions

The fourth sub-research object is defined as:

"Develop a control system model that enables combined DP station keeping and active roll reduction."

In this chapter a new control system model is presented that combines DP station keeping and active roll reduction. The newly proposed control model consist out of a high-level motion controller, which is a combination of a proportional anti-roll controller and a conventional DP controller, and lower-level shaft speed and azimuth angle controllers. Allocation matrices are used to transfer the controller commands to the correct thrusters. The motion controller command is subsequently used as input variable for the shaft speed controller in the dynamic thruster model. The azimuth angle of the thrusters used for motion control in the surge direction is controlled by a proportional controller to ensure the ability to counteract environmental forces in the surge direction. Tuning of the newly proposed controllers is done by conducting systematic simulations. The conventional shaft speed and DP controller are tuned by obtaining first estimates from literature.

From this research is concluded that:

- It is essential to form thruster pairs to achieve combined DP station keeping and active roll reduction.
- The optimal minimum RPM limit to achieve maximum roll reduction is 5% of the maximum thruster RPM.
- A proportional controller is the most effective controller for active roll reduction.
- By implementing a proportional azimuth angle controller, the control system is able to counteract environmental loads in the surge direction.

6
Results

In this chapter, results regarding the performance of the proposed control system model are presented and compared to a conventional DP system model.

6.1. Introduction

The performance of the proposed control model is analyzed on the basis of multiple aspects. The aspects that will be treated in this chapter are:

- Roll reduction
- DP footprint
- DP capability
- Thruster power consumption
- Workability

Each aspect will be treated in a dedicated section.

6.2. Roll reduction

In order to analyze the roll reduction obtained by the 3DP control system, systematic simulations in irregular sea states have been carried out. First, the simulation is carried out without roll control activated. Subsequently, active roll control is activated. A snapshot of the roll amplitude time traces is given in Figure 6.1.

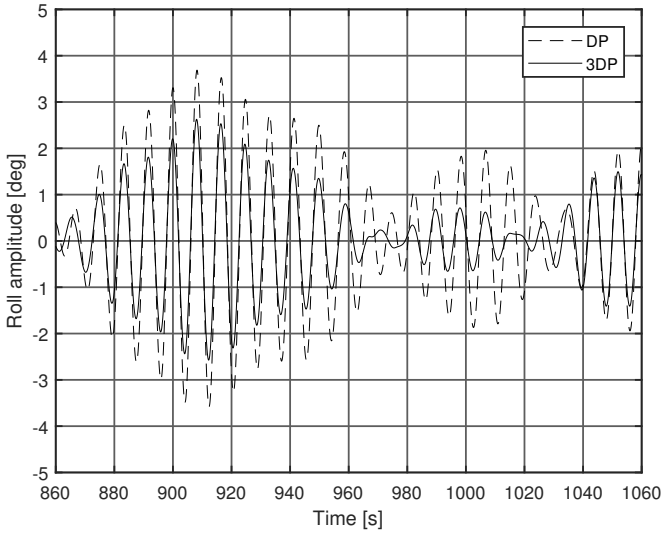

Figure 6.1: Snapshot of the roll angles time traces with and without active roll control ($H_s = 0.5$m and $T_p = 8.5$s)

As can be derived from Figure 6.1, the control system is able to actively reduce the roll angle amplitudes of the vessel in irregular waves. To quantify the roll reduction, the RMS of both roll angle time traces is calculated for a range of wave periods at a constant significant wave height and vice versa for a range significant wave heights at a constant wave period. The results are observable in Figure 6.2.

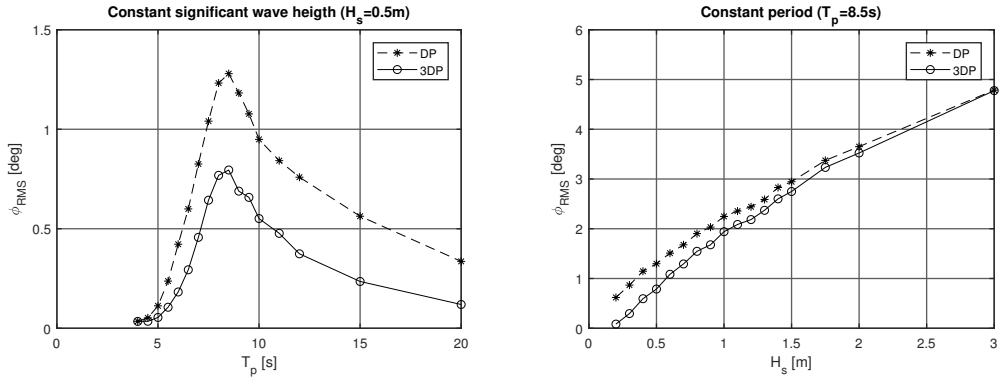

Figure 6.2: Roll angle RMS as a function of wave period and significant wave height for both control models

From the first plot in Figure 6.2 can be observed that the roll reduction increases significantly in the lower period range (T_p=4.5-7s), this can be explained by the fact that the thruster are less able to counteract the short waves due to their response time, which is in the range of the wave period. In the higher period range (T_p=8-20s) it can be observed that thrusters are able to significantly reduce the roll RMS. The maximum reduction is achieved when T_p= 8.5s, the natural frequency of the vessel.

The second plot in Figure 6.2 indicates that thruster induced roll reduction decreases when the significant wave height increases. This is the result of the fact that the wave induced roll moment becomes larger in comparison to the maximum thruster induced counteracting roll moment. Therefore, the relative contribution of the thrusters decreases when the significant wave height is increased.

To quickly obtain an estimate of the relative RMS roll reduction percentage at the roll natural frequency for different sea states, the RRR results are fitted by an exponential model. The result is given in Figure 6.3.

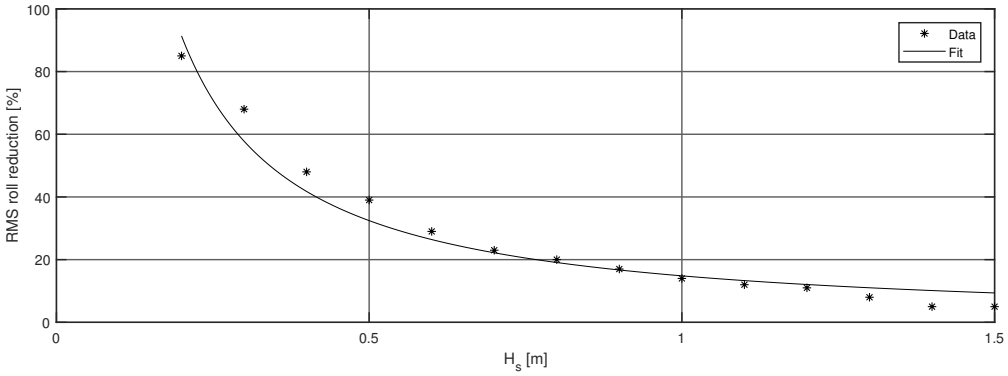

Figure 6.3: Relative RMS roll angle percentage at the roll natural frequency versus significant wave height

The exponential fit model is given by:

$$RRR = 14.83 \cdot H_s^{-1.13} \tag{6.1}$$

As can be derived from Figure 6.3, the fit model somewhat underestimates the RMS roll reduction percentages during low significant wave heights and slightly overestimates the RRR percentage during the higher wave heights. However, the model is deemed appropriate to obtain a quick estimate of the

expected roll reduction percentage for a particular significant wave height.

In order to analyze the roll reduction performance of the 3DP model in different conditions, systematic simulations with different values of H_s and T_p have been carried out. During these simulations, the current velocity V_c and wind velocity V_w is kept constant at:

$$V_w = 3.32\,\text{m/s}$$
$$V_c = 0.75\,\text{m/s}$$
$$\mu = 90^\circ \quad \text{(for both wind and current)}$$

The resulting roll reduction during every sea state is visualized in the contour plot given in Figure 6.4.

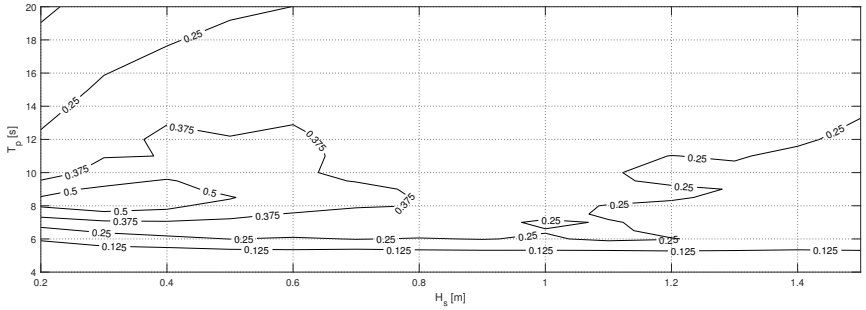

Figure 6.4: Contour plot of roll reduction for different combinations of T_p and H_s

As can be derived from Figure 6.4, the roll reduction is maximum for low sea states around the natural frequency. The minimum roll reduction is found at the lower periods, since the thrusters are not able to counteract the short wave periods. Again a trend is visible that the roll reduction decreases when the significant wave height increases.

6.3. DP footprint

The DP footprint visualizes the maximum excursions of the vessel in the horizontal earth-fixed reference frame with respect to the DP setpoint. To assess the station keeping performance of the proposed control model, the DP footprint of a conventional DP system is compared to the DP footprint of the 3DP control system. The simulated cases are given in Table 6.1.

Case	**Draft**	$\mathbf{V_w}$	μ_w	$\mathbf{V_c}$	μ_c	$\mathbf{H_s}$	$\mathbf{T_p}$	μ_{H_s}	**Spectrum**
[#]	[m]	[m/s]	[deg]	[m/s]	[deg]	[m]	[s]	[deg]	[-]
1	4.7	0.39	90	0.75	90	0.5	8.5	90	JONSWAP
2	4.7	1.94	90	0.75	90	0.75	8.5	90	JONSWAP
3	4.7	3.32	90	0.75	90	1.0	8.5	90	JONSWAP

Table 6.1: Overview of simulation cases and corresponding environmental conditions

The wind and current velocity is chosen according the environmental conditions table given in IMCA. The wave period is equal to the natural roll frequency of the vessel. The results are given in Figure 6.5.

From Figure 6.5 can be observed that the DP footprint of both control models increases during an increasing significant wave height. This behavior is as expected, since the environmental loads increase. Figure 6.5 also indicates that the DP footprint of the DP model is smaller compared to the DP footprint of the 3DP model. This can be explained by the fact that the thrusters produce oscillating thrust levels due to the combination of the anti-roll and DP controller. The maximum increase of the DP footprint is 1 meter in the sway direction. This is considered an acceptable magnitude.

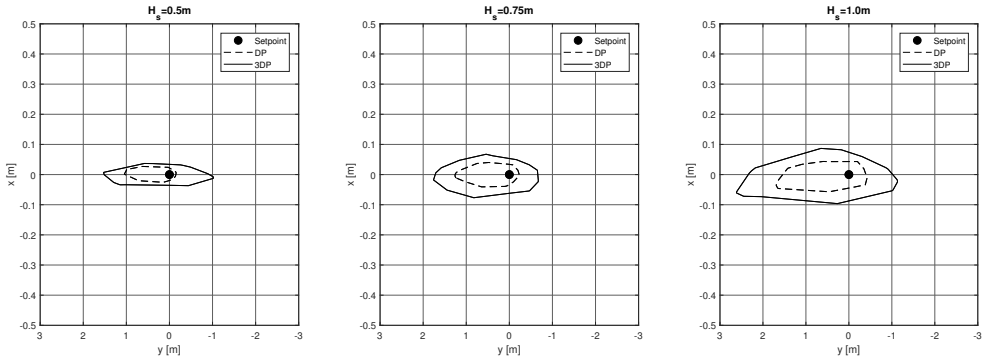

Figure 6.5: DP footprints results for case 1,2 and 3

Next to the station keeping performance of the vessel regarding its horizontal position, also the yaw motions are of interest. The thrust variations will result in significant yaw moments, which the control system has to counteract. A normal distribution has been used to visualized the yaw station keeping performance of the vessel when both control models are applied, see Figure 6.6.

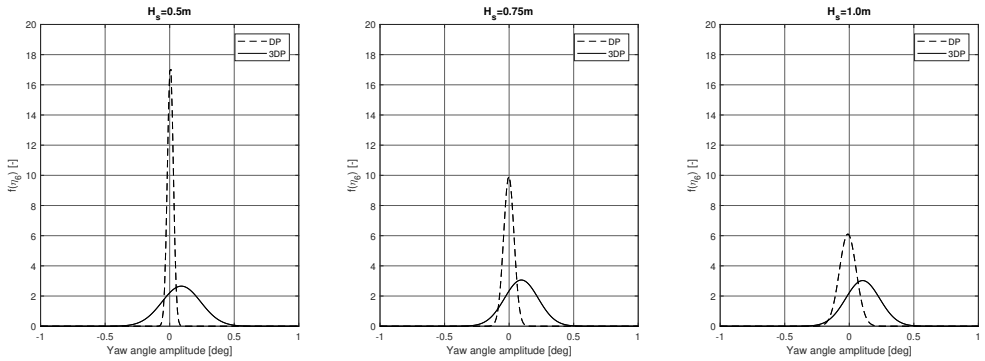

Figure 6.6: Normal distribution probability density function of the yaw motion for case 1,2 and 3

From Figure 6.6 can be observed that DP model has the highest probability density at a yaw angle of 0°. This is as expected, since the DP model yaw angle setpoint is 0°. Figure 6.6 also shows that the variance increases proportional to the significant wave height. This can be explained by the fact that the vessel motions increase as a result of the increased environmental loads during higher significant wave heights.

The 3DP model results show that the mean of the probability density function is slightly shifted towards a yaw angle of 0.1°. This can be explained by the fact that the yaw moments in the 3DP model are significantly higher compared to the 3DP model. The K_i coefficient term of the DP controller in the 3DP model should be increased to remove the yaw offset. However, for comparison reasons, it is decided to use the same DP controller tuning variables in both the DP and the 3DP model.

The plots show that the probability density function remains more or less constant during increased significant wave heights. This is the result of the fact that the yaw moments induced by the thrusters are significantly bigger in magnitude compared to the yaw moments resulting from waves, current and wind.

The yaw angle variance of the 3DP model is bigger compared to the DP model. This is explained by the oscillating yaw moments induced by the thrusters during active roll reduction. The maximum increase of the yaw angle is 0.7°, which is considered acceptable.

6.4. DP capability

Also the station keeping capability of the vessel during active roll reduction in beam waves is of interest. The station keeping capability is in this study defined by the limiting current speeds at which the vessel is still able to maintain position. Maintaining position is defined according the positioning limits as defined by DNV-GL [9] for DP capability level 3. The positioning limits herein are defined as a maximum of 5 meter excursion from the DP setpoint and a maximum of +/-3° yaw angle excursion. The current velocity is increased per environmental direction until the vessel exceeded the specified positioning limits. The last current velocities at which the vessel was still able to remain within the positioning limits are visualized in Figure 6.7

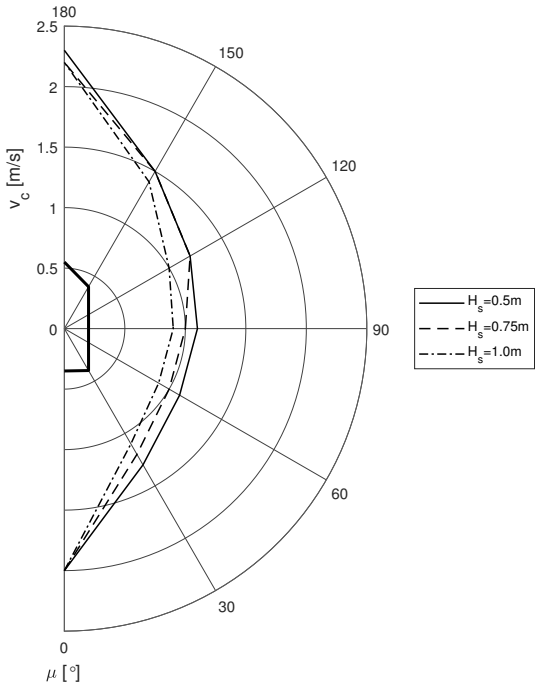

Figure 6.7: Limiting current velocities per environmental direction for case 1,2 and 3, wave force is always beam on

From Figure 6.7 can be observed that the limiting current velocities per environmental direction decrease when the significant wave height increases. This is as expected since the environmental loads on the vessel increase proportional to the wave height. The vessel is able to maintain position during relative high current velocities of 2.2 m/s and 2.0 m/s in respectively head and following seas. In beam seas, the station keeping capability is limited by a current velocity of 0.9 m/s for a H_s=1m.

6.5. Thruster power consumption

The 3DP control model is designed to obtain maximum roll reduction. The achieved roll reduction comes at a cost. This cost can be expressed in terms of power consumed by the thrusters. The thruster power consumption is calculated according Stapersma [34] by:

$$P_T = 2\pi Q_p n_s \tag{6.2}$$

where Q_p and n_s represent the propeller torque and the shaft speed.

In the DP control model, the shaft speed and propeller torque are not calculated. Therefore, a different approach is used to calculate the power consumption by the thrusters.
From Equation 6.2 can be derived that the thruster power consumption has a cubic relation with respect to the shaft speed, since it is known that propeller torque scales $\sim^2$ with shaft speed, see Equation 3.13. Using this relation, the power consumption of every thruster is calculated according:

$$P_T = P_{max}\left(\frac{T}{T_{max}}\right)^{1.5} \tag{6.3}$$

where P_{max}, T, T_{max} represent the maximum power consumption of the thruster, actual thrust produced by the thruster and the maximum thrust magnitude of the thruster.

The sum of the power consumption of every thruster is calculated to obtain the total power consumption of the control system over time. The mean of the total power consumption of both control models is calculated and is expressed in percentage of the total installed thruster power. The results are given in Figure 6.8

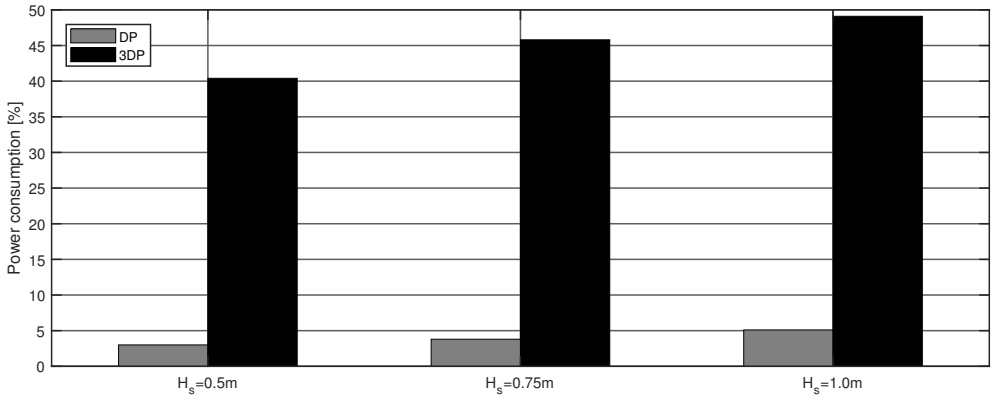

Figure 6.8: Mean power consumption percentage of total installed DP power for case 1,2 and 3

Figure 6.8 clearly indicates that the power consumption of the 3DP control system is significantly higher compared to the DP system. This is as expected, since the thrusters are constantly ramping up to maximum thrust. It also logical that the power consumption of the thrusters is around 50% of the total installed thruster power, since the thrusters are working 50% of their time at thrust levels near the maximum level to counteract the wave induced roll moment. The power consumption is around a factor 10 higher compared to the 3DP model.

From Figure 6.8 can also be observed that the power consumption of both control systems increases during increasing sea state. This is as expected, since the environmental loads increase accordingly.

6.6. Workability

The final step is to analyze whether application of the 3DP control model results in increased vessel workability. Workability is defined as the percentage of time the vessel is able to carry out operational activities like crane operations, tool over-boardings and subsea power cable pull-ins. The ability to conduct these operations is determined by vessel operability. The operability is defined by operating criteria, see for example the NORDFORSK criteria in Journée [20].

In this research, the focus is on critical offshore operations, which are sensitive to roll motions. For example, the over-boarding of a trencher for subsea power cable burial operations. It is assumed that this type of operations have an operability limit of 1° roll RMS. To calculate the workability, the vessel roll RMS is calculated for a range of sea states defined by different combinations of H_s and T_p. It is assumed that the following conditions are present during each sea state:

$$V_w = 3.32 \text{ m/s}$$
$$V_c = 0.75 \text{ m/s}$$
$$\mu = 90^\circ \quad \text{(for both wind and current)}$$

The sea states during which the vessel roll RMS exceeds the defined operability limit are marked with a 'x'. This procedure has been done for both the DP and the 3DP control system model. The results are given in operability tables, see Table 6.2 and Table 6.3.

$\mathbf{T_p[s]/H_s[m]}$	**0.2**	**0.3**	**0.4**	**0.5**	**0.6**	**0.7**	**0.8**	**0.9**	**1.0**	**1.1**	**1.2**	**1.3**	**1.4**	**1.5**
4														
4.5														
5														
5.5														
6													x	x
6.5									x	x	x	x	x	x
7						x	x	x	x	x	x	x	x	x
7.5				x	x	x	x	x	x	x	x	x	x	x
8			x	x	x	x	x	x	x	x	x	x	x	x
8.5			x	x	x	x	x	x	x	x	x	x	x	x
9			x	x	x	x	x	x	x	x	x	x	x	x
9.5				x	x	x	x	x	x	x	x	x	x	x
10					x	x	x	x	x	x	x	x	x	x

Table 6.2: Operability table for the DP control model

$\mathbf{T_p[s]/H_s[m]}$	**0.2**	**0.3**	**0.4**	**0.5**	**0.6**	**0.7**	**0.8**	**0.9**	**1.0**	**1.1**	**1.2**	**1.3**	**1.4**	**1.5**
4														
4.5														
5														
5.5														
6														
6.5											x	x	x	x
7								x	x	x	x	x	x	x
7.5						x	x	x	x	x	x	x	x	x
8						x	x	x	x	x	x	x	x	x
8.5					x	x	x	x	x	x	x	x	x	x
9					x	x	x	x	x	x	x	x	x	x
9.5						x	x	x	x	x	x	x	x	x
10							x	x	x	x	x	x	x	x

Table 6.3: Operability table for the 3DP control model

To determine the workability increase, both the operability tables are applied to a yearly wave scatter that represent the wave climate at the Borssele offshore wind farm. The wind farm location is visualized in Figure 6.9

Figure 6.9: Location of the Borssele offshore wind farm (marked with x)

The wave scatter used is given in Table 6.4. The complete wave scatter is given in Appendix E.

$\mathbf{T_p[s]/H_s[m]}$	**0.2**	**0.3**	**0.4**	**0.5**	**0.6**	**0.7**	**0.8**	**0.9**	**1.0**	**1.1**	**1.2**	**1.3**	**1.4**	**1.5**
4	0.4	1.0	1.3	1.0	0.7	0.4	0.5	0.7	0.7	0.5	0.4	0.2	0.1	0.0
4.5	0.5	0.9	0.9	0.9	0.4	0.3	0.4	0.4	0.5	0.3	0.4	0.4	0.2	0.1
5	0.8	0.6	0.6	0.3	0.4	0.8	0.5	0.5	0.4	0.3	0.2	0.2	0.1	0.1
5.5	0.3	0.8	0.7	0.4	0.4	0.6	0.4	0.4	0.3	0.2	0.3	0.3	0.2	0.1
6	0.2	1.1	1.1	0.8	0.6	0.3	0.3	0.3	0.4	0.2	0.2	0.1	0.2	0.0
6.5	0.3	1.3	1.3	1.3	1.1	0.7	0.2	0.2	0.3	0.1	0.1	0.2	0.2	0.2
7	0.2	0.8	1.1	0.9	1.0	0.7	0.2	0.1	0.1	0.0	0.1	0.1	0.0	0.0
7.5	0.0	0.5	1.2	1.0	0.9	0.4	0.3	0.2	0.1	0.1	0.0	0.0	0.1	0.0
8	0.0	0.2	0.2	0.5	0.4	0.3	0.2	0.1	0.1	0.1	0.0	0.0	0.0	0.0
8.5	0.0	0.1	0.2	0.2	0.2	0.1	0.1	0.1	0.0	0.0	0.0	0.0	0.0	0.0
9	0.2	0.1	0.1	0.1	0.2	0.0	0.1	0.0	0.0	0.0	0.0	0.1	0.0	0.0
9.5	0.1	0.0	0.1	0.0	0.1	0.0	0.0	0.0	0.0	0.0	0.0	0.0	0.1	0.0
10	0.1	0.1	0.0	0.0	0.0	0.0	0.1	0.0	0.1	0.1	0.1	0.0	0.0	0.1

Table 6.4: Yearly wave scatter of the Borssele field, values are in percentage. Light grey represent sea states at which the operability limit is exceeded for the DP model. Dark gray represent the 3DP model

The wave scatter given in Table 6.4 shows the percentage of time a particular sea state occurs at the specific offshore location. By removing the percentages of the sea states marked with an 'x' in the operability tables and adding up the percentages in the wave scatter, the workability of the operation is calculated. This process is indicated by the light gray and dark gray colored cells in Table 6.4.

The increased vessel workability is calculated by:

$$W_{inc} = W_{3DP} - W_{DP} \tag{6.4}$$

where W_{3DP} and W_{DP} represent respectively the workability obtained when the 3DP model and the DP model are applied. This corresponds by summing up the light gray colored cells in Table 6.4. The calculation results are given in Table 6.5.

W_{DP} [%]	89.9
W_{3DP} [%]	95.1
W_{inc} [%]	5.2

Table 6.5: Yearly workability calculation results in beam waves

A workability increase of 5.2% on a yearly basis corresponds to roughly 19 days. So by applying the

3DP model, the amount of days the vessel is limited by operability criteria decreased by 19 days. This corresponds to a relative decrease of 48% of the amount of days the vessel is not able to operate. One should take into account that this workability increase is only valid for operations in beam waves.

To assess the workability increase when the vessel is subjected to waves coming from different environmental conditions, simulations have been carried out for waves coming from 0° to 180° with intervals of 15°. The resulting operability tables for each environmental direction are given in Appendix E. The yearly workability of the vessel per environmental direction is given in Table 6.6. As can be derived from

μ [°]	**0**	**15**	**30**	**45**	**60**	**75**	**90**	**105**	**120**	**135**	**150**	**165**	**180**
W_{DP}[%]	100	100	100	99.7	95.5	92.3	89.9	91.3	94.6	98.9	100	100	100
W_{3DP}[%]	100	100	100	100	98.7	97	95.1	96	98.5	99.8	100	100	100

Table 6.6: Yearly workability per environmental direction for the DP and 3DP model for the Borssele field

Table 6.6, the workability of the vessel is only increased for environmental directions between 45°-135°. This is due to the fact that the roll response of the vessel during the other environmental conditions is much smaller in magnitude and is therefore not exceeding the operability limits. The workability increase per direction is visualized in Figure 6.10.

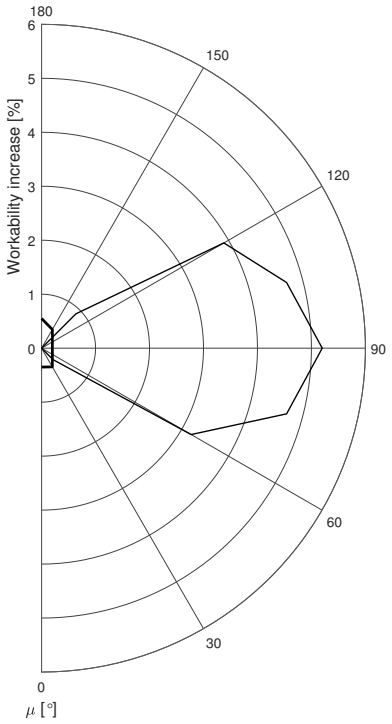

Figure 6.10: Yearly workability increase per environmental direction for the Borssele field when the 3DP model is engaged

As can be derived from Figure 6.10, the workability increase is maximum for beam waves and becomes less for other environmental directions. This can be explained by the fact that during beam waves, the vessel roll response is maximum. Application of the 3DP control system is therefore most effective during this condition.

It is assumed that the probability of occurrence of each environmental direction during critical operations is equal. The yearly workability increase can therefore be calculated by averaging the workability increase per direction. This results in an average workability increase of 2.0%. This corresponds to a week of increased workability on a yearly basis for the Borssele field. One should take into account that this estimate could change when a different wave scatter is used. For example, the Borssele wind farm is close to shore, so shorter wave periods are present. At a more offshore location, longer wave periods are more likely to occur, and therefore a higher workability increase can be expected.

7

Conclusions and Recommendations

In this chapter the conclusions are drawn based on the results of the conducted research. Next to this, recommendations regarding further research are given.

7.1. Conclusions

The fifth sub-research objective is defined as:

"Identify and quantify the possibility and magnitude of thruster induced roll reduction and its effect on the station keeping performance of the ship."

From the results presented in Chapter 6 is concluded that:

- It is possible to actively reduce the roll motion amplitude of the *Ndurance* by active control of the thrusters.
- The most significant roll reduction is obtained during sea states defined by significant wave heights in the range of 0.2 to 0.7 meter and wave peak periods around the natural roll period of the vessel. During these conditions, the achieved roll reduction is around 0.5° roll RMS.
- It is possible to combine active roll reduction and DP station keeping.
- The maximum DP footprint increase is 1 meter in the sway direction and 0.7° for the yaw motion of the vessel when the 3DP model is activated.
- In beam seas, the station keeping capability during active roll reduction is limited by a current velocity of 0.9 m/s during H_s=1m.
- The thruster power consumption increases with a factor 10 when the 3DP control model is engaged.
- The yearly workability of the *Ndurance* for the Borssele field increases with 5.2% in beam waves.
- The yearly workability increase for the Borssele field averaged over all environmental directions is 2.0%.

The main research objective is to evaluate the possibility of reducing the ship roll motion during DP operations by active control of the thrusters. From the conducted research is concluded that this is possible.

7.2. Recommendations

The sixth and final sub-research objective is defined as:

"Give recommendations regarding possible thruster alternatives, the ship lay-out and DP system configuration that influence the possibility and magnitude of actively controlled roll reduction."

The recommendations based on the conducted research given below.

- **Wear and tear of the thrusters**
  Probably the most import recommendation is to investigate the wear and tear experienced by the thruster system during active roll reduction mode. This study confirms that thruster induced roll reduction is possible. However, no attention has been paid to the wear and tear of the whole thruster drive train system. Since the system will operate in quite an unorthodox way, it is expected that the wear and tear of especially the gearbox and transmission will be significant. The increased maintenance cost, next to the increased fuel consumption, has to be taken into account when one is looking into the performance of the 3DP control system from a financial point of view.

- **Thruster alternatives**
  Alternative methods that can be used to achieve actively controlled roll reduction during DP operations are active anti-roll tanks as investigated by Habing [12] and active fins as proposed by Ikeda [15]. These systems however require vessel modifications and the installation of additional equipment and power. The limited amount of increased operability is probably not worth such an investment, as stated by Habing [12].

  Passive roll reduction can be achieved by fitting bilge keels at the bilge of the *Ndurance*. This option is also investigated by using a empirical bilge keel damping model, see Appendix F. From this research is concluded that fitting bilge keels at the *Ndurance* results in 4 times less roll reduction compared to the 3DP model during low to moderate sea states with wave periods around the roll natural period of the vessel. So fitting bilge keels at the *Ndurance* is probably not worth the investment.

- **Ship lay out**
  The achievable thruster induced roll reduction is probably more significant for ship-shaped vessels than for barge-shaped vessels. This is due to the fact that barge-shaped vessel experience a bigger roll moment in waves compared to a ship shaped vessel. The ratio between the counteracting thruster induced roll moment and the wave roll moment becomes smaller for ship-shaped vessels. Therefore, the thrusters are able to more significantly reduce the roll motion. To achieve optimum thruster induced roll reduction it is important that the thrusters are located as far away as possible from the vessel CoG to obtain a large roll moment arm.

- **Model tests**
  The performance of the constructed 3DP control model has only been investigated by conducting mathematical simulations. It is recommended to validate the implementation of a quadratic viscous damping term in the time domain model by conduction systematic roll tests on model scale for different wave heights and wave periods. On the basis of these results a new method or model can be constructed that more accurately describes the viscous damping term in the time domain.

- **Operational use**
  The use of the 3DP control model is probably only beneficial for critical moments during offshore operations. For example, when the vessel needs to conduct an operation that is at the roll operability limit and the weather forecast shows worsening weather conditions for the coming weeks. The RRR fit model can be used to asses the effectiveness of engaging the 3DP system. When considered effective, the 3DP system can enable the crew to carry out the operation, instead of leaving the field and start the waiting on weather for multiple weeks. In this way, the 3DP control model is more used as a back-up instrument instead of an operational mode that is engaged for longer periods of time.

- **New innovations**
  New innovations like lighter composite propellers and improved electrical drives are currently introduced in the maritime industry. These innovations can increase the feasibility and performance of thruster induced active roll reduction. Also new innovations can be thought off. For example, one could design a system where the thruster pair ramping up could benefit from the wasted energy of the thruster pair that is braking or ramping down at the same moment. Maybe an intelligent energy conversion or transfer system can be developed and applied.

- **Modelling approach**
  A lot of students use software packages like OrcaFlex or AQWA when one wants to conduct time domain simulations. I would encourage everybody that is planning to do so during their graduation to try to develop a time domain model by yourself. I believe it strongly increases the knowledge regarding time domain simulations, vessel behavior and dynamics. Next to this, it enables you in a lot of cases to conduct simulations much more faster and to post-process the results more quickly.

A Appendix

A.1. Vessel particulars

A photo of the *Ndurance* in the field at the Egmond aan Zee wind farm is given in Figure A.1.

Figure A.1: *Ndurance* in the field at the Egmond aan Zee wind farm

The vessel particulars of the cable-lay vessel *Ndurance* are given in Table A.1.

Vessel	***Ndurance***
L [m]	99
B [m]	30
D [m]	4.7
∇ [m^3]	11400
I_{xx} [kgm^2]	1.24E+09
I_{yy} [kgm^2]	7.33E+09
I_{zz} [kgm^2]	7.93E+09
C_{33} [N/m]	2.77E+07
C_{44} [Nm/rad]	1.25E+09
C_{55} [Nm/rad]	1.95E+10
C_{35} [Nm/rad]	7.74E+07
KG [m]	4.29
A_t [m^2]	430
A_l [m^2]	807

Table A.1: Vessel particulars *Ndurance*

A.2. Ramp function

A ramp function is used when environmental loads are applied to the vessel time domain model. By doing so, the transient response of vessel time domain model is decreased. Especially for calculation of the motion RAO's this is important to avoid, since one does not want a motion offset in the results. The ramp function is chosen similar as in OrcaFlex and is calculated by:

$$f_{ramp} = u^3(6u^2 - 15u + 10) \tag{A.1}$$

where u is a parameter in the range $[0, 1]$. The length of the ramp function can be selected by adjusting the slope of u:

$$\Delta u = \frac{1}{t_{end}} \tag{A.2}$$

where t_{end} is the desired endtime of the ramp function. A visualization of the ramp function for an endtime of 100 seconds is given in Figure A.2.

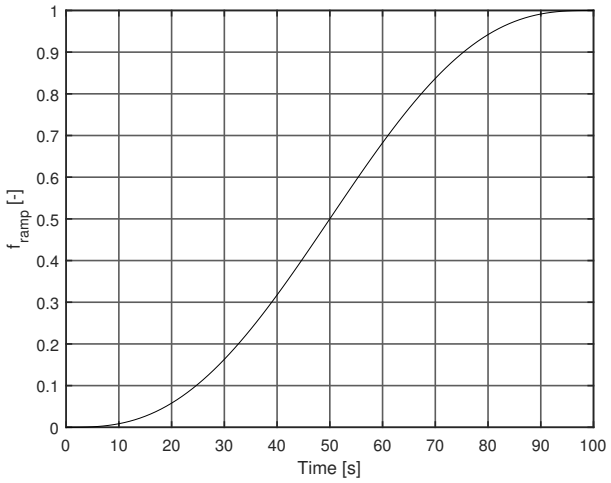

Figure A.2: Ramp function for t_{end}=100s

B
Appendix

B.1. Thruster and electrical drive data

The thruster parameters are given in Table B.1.

Thruster type	**TH1250**	**TH1500**
D [m]	1.75	2.00
P/D [-]	1	1.2
Z [-]	4	4
EAR [-]	0.7	0.7
Propeller type	Kaplan	Kaplan
Nozzle	19A	19A
k_g [-]	3.409	6.207
Power [kW]	1000	1250
Thrust in bollard pull [kN]	177	222
I_p [kgm^2]	10.2	9.2
I_e as fraction of I_p [-]	0.385	0.332
I_{ps} [kgm^2]	0.6	0.6
Q_s [Nm]	320	270
K_ω [Nms/rad]	0.4	0.32
Roll moment arm [m]	10.2	7.7

Table B.1: Thruster TH1250 and TH1500 particulars

The electrical drive particulars are given in Table B.2.

Electrical drive	**AEM WH450-L6**	**Hyundai HRN3-48E**
Power [kW]	1000	1250
Torque [Nm]	8000	6745
Rel. break down torque [-]	2.6	2.5
Nom. RPM [1/m]	1200	1800
Frequency [Hz]	60	60
T_m [s]	0.1	0.1
I_r [kgm^2]	65.0	33.8

Table B.2: Electrical drive particulars

B.2. Four-quadrant Fourier coefficients

The four-quadrant coefficients A_T, A_Q, B_T and B_Q are given in Table B.3. The application of the coefficients resulted in a erroneous estimation of the thruster coefficients. It was concluded that Oosterveld reported some mistaken coefficients in his report. After some trial-and-error procedures the correct values for the Ka 4-70 propeller with P/D=1.0 and P/D=1.2 in the 19A nozzle were obtained. The corrected values are given in Table B.3 and Table B.4.

Order	$\mathbf{C_T}$		$\mathbf{C_Q}$	
k	A(k)	B(k)	A(k)	B(k)
0	-1.09850E-01	0.0000E+00	3.15890E-02	0.00000E+00
1	1.40640E-01	-1.0583E+00	2.44060E-01	-1.17170E+00
2	1.57850E-01	4.7284E-02	-7.38800E-03	5.11550E-02
3	4.55440E-02	1.3126E-01	2.82600E-02	8.90690E-02
4	5.16390E-03	-7.7539E-03	-5.59590E-03	6.56700E-03
5	-2.55600E-03	9.3507E-02	2.65580E-04	1.42040E-01
6	-6.05020E-03	9.2520E-03	1.13680E-02	7.70520E-03
7	6.73680E-03	-1.4828E-02	-4.74010E-02	-3.60910E-02
8	6.85710E-03	-9.6554E-03	-6.56860E-03	4.20360E-03
9	4.72450E-03	9.6216E-03	-7.49900E-03	2.11390E-03
10	2.35910E-03	-7.5453E-04	1.28730E-03*	1.30950E-02
11	8.79120E-03	2.4453E-03	4.65020E-03	3.09610E-02
12	1.19680E-03	-8.7981E-03	-4.66760E-03	-9.94590E-03
13	8.38080E-03	1.8184E-03	3.34380E-03	1.79210E-02
14	-8.20980E-04	-2.0077E-03	2.20460E-03	-8.19170E-03
15	2.73710E-03	-3.3070E-03	7.00340E-03	-7.84280E-04
16	-2.61210E-04	-7.9201E-04	3.91470E-03*	7.26610E-03
17	1.91330E-03	-3.6311E-04	7.37190E-03	-4.73160E-03
18	3.22900E-04	-1.9377E-03*	9.40830E-04	-2.57310E-03
19	1.52230E-03	-1.2135E-03	6.05600E-03	1.11360E-03
20	-1.01510E-03	-3.1678E-04	4.23900E-04	-1.54700E-03

Table B.3: Corrected (marked with an *) coefficients as reported by Oosterveld for the Ka 4-70 (P/D=1.0) propeller in a 19A nozzle [22]

Order	$\mathbf{C_T}$		$\mathbf{C_Q}$	
k	A(k)	B(k)	A(k)	B(k)
0	-9.08880E-02	0.0000E+00	4.38000E-02	0.0000E+00
1	1.79590E-01	-1.0260E+00	3.52990E-01	-1.2949E+00
2	1.49560E-01	6.1459E-02	-1.09170E-02	5.9030E-02
3	6.56750E-02	1.3715E-01	4.70620E-02	9.3540E-02
4	5.21070E-03	-1.7280E-02	-1.07790E-02	-6.1148E-03
5	-6.82320E-03	9.6579E-02	-1.01930E-02	1.6121E-01
6	-6.28960E-03	5.8809E-03	-8.88240E-04	1.4624E-02
7	1.81780E-02	-2.2587E-02	-3.78930E-02	-5.3549E-02
8	6.06940E-03	-1.4819E-02	-7.03460E-03	-3.1589E-03
9	6.19420E-03	1.0398E-02*	-8.01300E-03	1.4382E-02
10	2.64820E-03	-2.9324E-03	7.26220E-03	9.9836E-03
11	1.21370E-02	4.0913E-03	-5.43900E-03	3.8781E-02
12	-3.57050E-03	-4.4436E-03	-2.00380E-03	-4.6749E-03
13	3.29850E-03	-1.2190E-03	3.92810E-03	1.4944E-02
14	-8.86520E-04	-2.2551E-03	-6.52560E-04	-6.3253E-03
15	6.98070E-03	-3.2272E-03	1.54140E-02	2.2275E-03
16	-1.75600E-04	1.7533E-03	3.03560E-03	7.1826E-03
17	2.16430E-03	1.4875E-03	5.90730E-03	1.0229E-03
18	3.53620E-04	4.5353E-05	4.14330E-03	-5.9201E-03
19	2.57720E-03	-8.8702E-04	4.61020E-03	-1.4814E-03
20	-1.82790E-03	-9.4609E-04	-5.74230E-04	-4.3092E-03

Table B.4: Corrected (marked with an *) coefficients as reported by Oosterveld for the Ka 4-70 (P/D=1.2) propeller in a 19A nozzle [22]

B.3. Thrust deduction factor

The thrust deduction factor due to thruster-hull interaction is based on the work of Wichers [35]. An azimuth angle of 90° has been assumed. A factor of 0.04 is used, see Figure B.1.

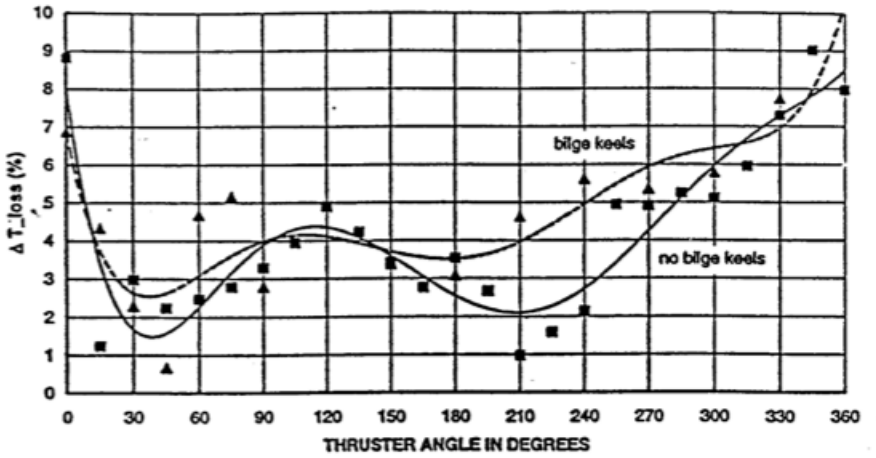

Figure B.1: Thrust deduction percentage due to thruster-hull interaction as a factor of azimuth angle according Wichers [35]

The thruster moment arms in the horizontal plane with respect to the CoG are given in Table B.5

Thruster	x [m]	y [m]
T1	45	0
T2	36.5	7.5
T3	36.5	-7.5
T4	-45.5	7.5
T5	-45.5	-7.5

Table B.5: Thruster moment arms with respect to vessel CoG

C
Appendix

C.1. Wind and current coefficients

The wind coeffcients are given in Figure C.1

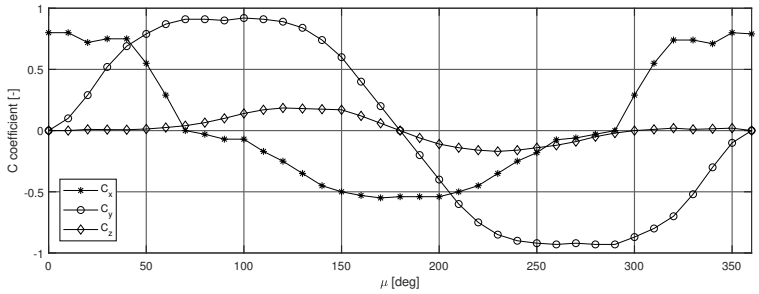

Figure C.1: *Ndurance* wind coefficients per environmental direction

The current coeffcients are given in Figure C.2

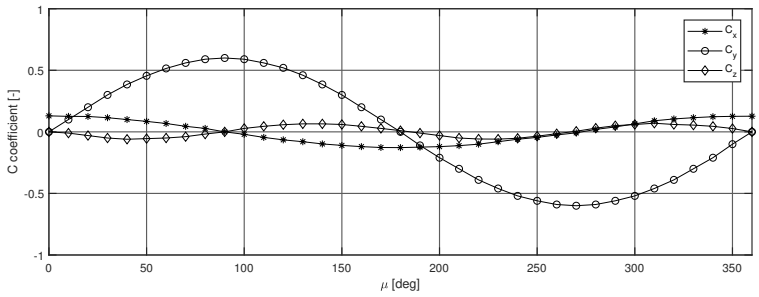

Figure C.2: *Ndurance* current coefficients per environmental direction

C.2. DP model tuning parameters

The tuning parameters used in the controller and the Kalman filter implemented in the DP model system for comparison with the AnySim simulations are given in Table C.1.

Motion	Surge	Sway	Yaw
K_p	212.2	235.8	4932.21
K_d	2309.35	2776.35	34781.5
Q	1.00E-09	2.00E-09	1.00E-09
R	1.30E-04	6.50E-05	1.30E-04

Table C.1: Controller and Kalman filter tuning parameters

The integral tuning coefficient K_i is omitted, since this is also the case in the AnySim simulations.

C.3. Forbidden zones

The performance of the allocation algorithm is checked by subjecting the vessel to environmental loads coming from 0° to 360°. The calculated thruster angles by the allocation algorithm to counteract the environmental loads are visualized in Figure C.3.

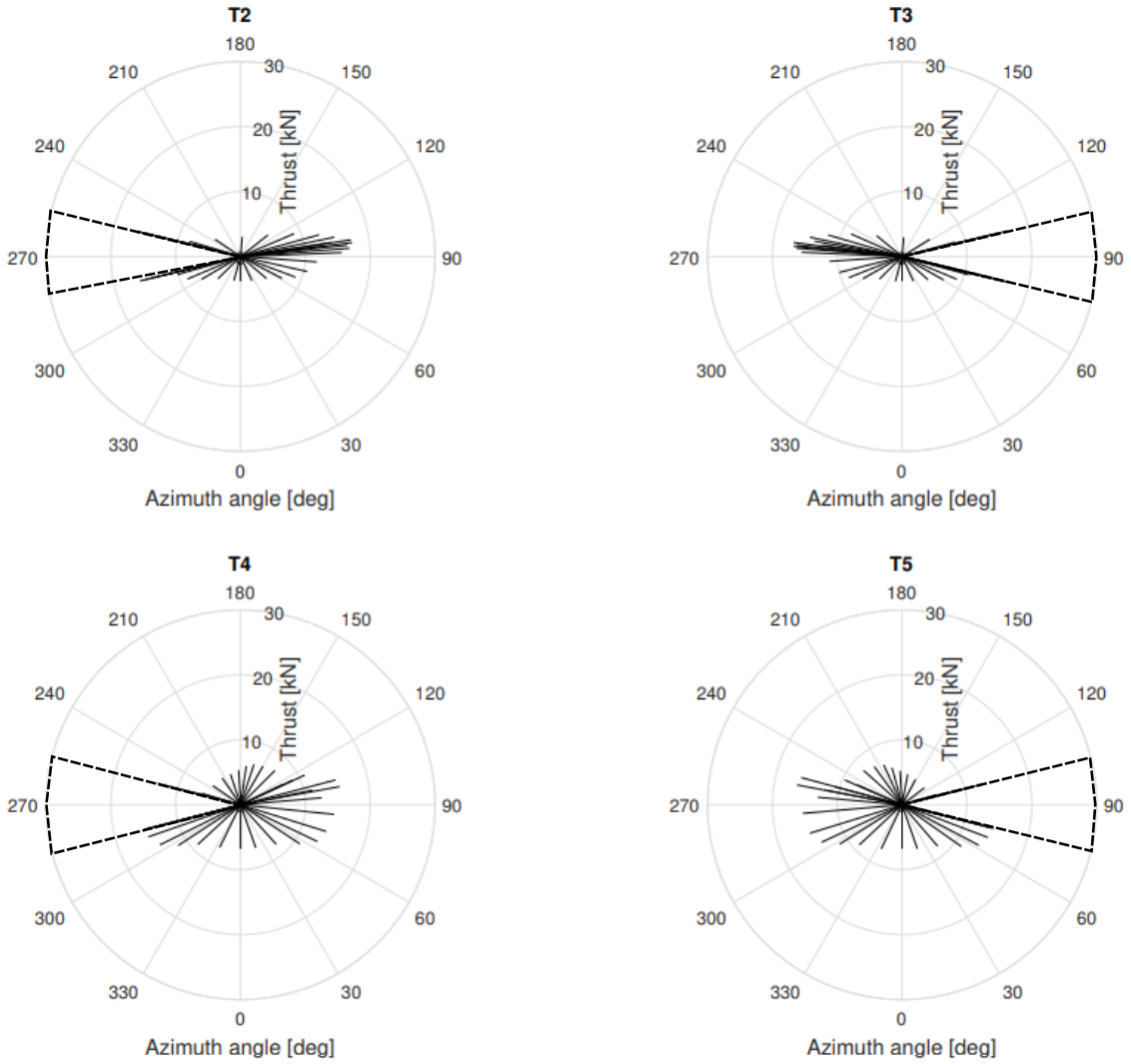

Figure C.3: Thrust magnitude and azimuth angles for different environmental directions, the forbidden zones are indicated by the dotted triangles

As can be observed from Figure C.3, the allocation algorithm does not result in azimuth angles within the forbidden zones. From this result is concluded that the allocation algorithm is performing as intended.

D
Appendix

D.1. Tuning coefficients of 3DP model

The tuning coefficients of the DP controller in the 3DP control system model are given in Table D.1.

DP Controller	Surge	Sway	Yaw
K_p	106.1	117.9	4932.2
K_i	0.25	0.30	0.01
K_d	1154.7	1388.2	34781.5
Q	1.00E-09	2.00E-09	1.00E-09
R	1.30E-04	6.50E-05	1.30E-04

Table D.1: Tuning coefficients of the DP controller and Kalman filter in the 3DP model

The controller coefficients as used in the 3DP control model for the roll controller, azimuth controller and shaft speed controllers are given in Table D.2.

Roll controller	
K_p	2.50E+06
Azimuth controller	
K_p	0.9
Shaft speed controller (TH1250)	
K_p	33.3
K_i	16.65
Shaft speed controller (TH1500)	
K_p	19.9
K_i	9.95

Table D.2: Tuning coefficients of the roll controller, azimuth controller and shaft speed controllers as implemented in the 3DP control model

D.2. Motion time traces

A typical simulation time trace of the horizontal motions surge, sway and when both the DP and the 3DP model are applied are given in Figure D.1.

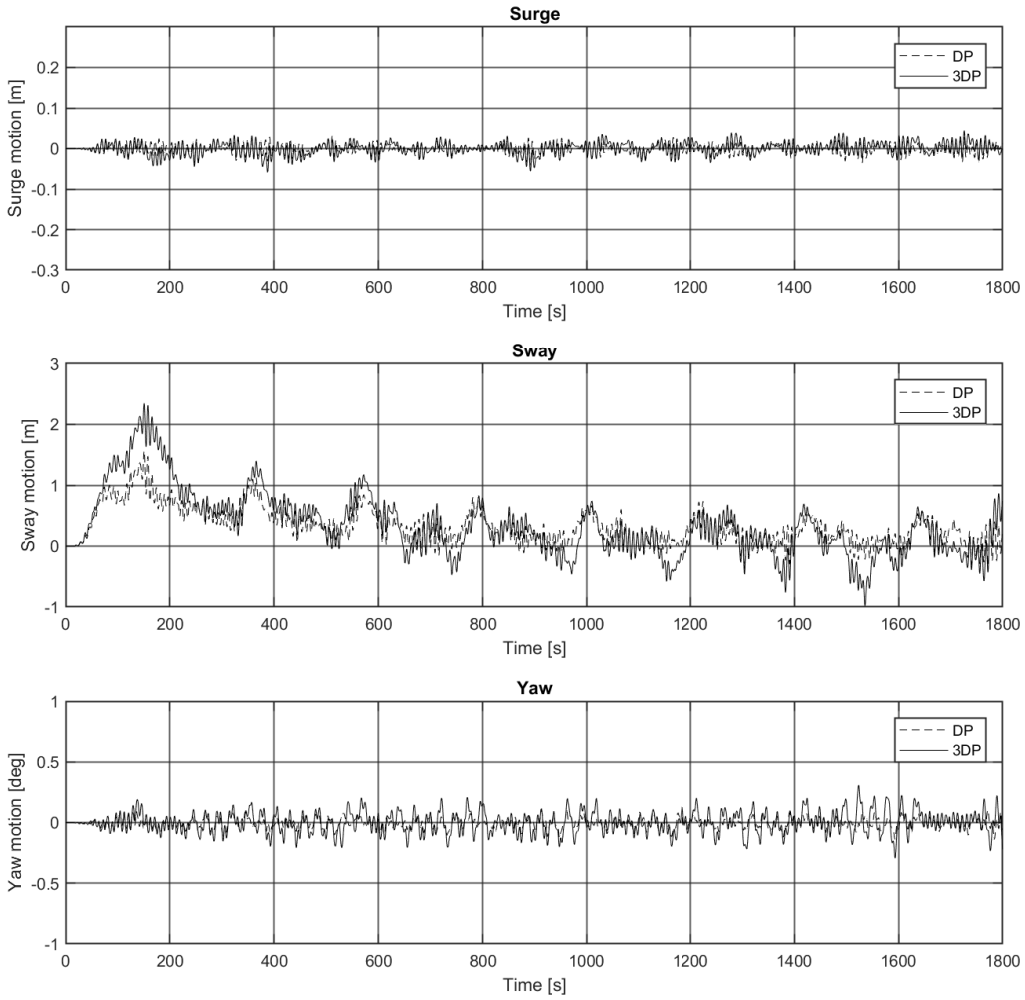

Figure D.1: Time traces of horizontal motions when both DP and 3DP model are applied (H_s=0.75m, T_p=8s

E

Appendix

E.1. Yearly wave scatter Borssele

In Table E.1, the complete yearly wave scatter of the Borssele field is given.

$\mathbf{T_p[s]/H_s[m]}$	**0.2**	**0.3**	**0.4**	**0.5**	**0.6**	**0.7**	**0.8**	**0.9**	**1.0**	**1.1**	**1.2**	**1.3**	**1.4**	**1.5**	**1.6**
1	1.0	0.0	0.0	0.0	0.0	0.0	0.0	0.0	0.0	0.0	0.0	0.0	0.0	0.0	0.0
1.5	2.3	2.6	1.3	0.1	0.0	0.0	0.0	0.0	0.0	0.0	0.0	0.0	0.0	0.0	0.0
2	0.6	3.6	3.5	1.4	1.1	0.2	0.0	0.0	0.0	0.0	0.0	0.0	0.0	0.0	0.0
2.5	1.0	0.8	2.6	3.5	1.7	0.4	0.1	0.1	0.0	0.0	0.0	0.0	0.0	0.0	0.0
3	1.3	1.8	0.9	1.2	1.5	1.6	0.5	0.3	0.1	0.0	0.0	0.0	0.0	0.0	0.0
3.5	0.5	1.7	0.8	0.7	0.7	0.8	0.8	0.6	0.3	0.2	0.1	0.0	0.0	0.0	0.0
4	0.4	1.0	1.3	1.0	0.7	0.4	0.5	0.7	0.7	0.5	0.4	0.2	0.1	0.0	0.0
4.5	0.5	0.9	0.9	0.9	0.4	0.3	0.4	0.4	0.5	0.3	0.4	0.4	0.2	0.1	0.0
5	0.8	0.6	0.6	0.3	0.4	0.8	0.5	0.5	0.4	0.3	0.2	0.2	0.1	0.1	0.1
5.5	0.3	0.8	0.7	0.4	0.4	0.6	0.4	0.4	0.3	0.2	0.3	0.3	0.2	0.1	0.1
6	0.2	1.1	1.1	0.8	0.6	0.3	0.3	0.3	0.4	0.2	0.2	0.1	0.2	0.0	0.0
6.5	0.3	1.3	1.3	1.3	1.1	0.7	0.2	0.2	0.3	0.1	0.1	0.2	0.2	0.2	0.0
7	0.2	0.8	1.1	0.9	1.0	0.7	0.2	0.1	0.1	0.0	0.1	0.1	0.0	0.0	0.1
7.5	0.0	0.5	1.2	1.0	0.9	0.4	0.3	0.2	0.1	0.1	0.0	0.0	0.1	0.0	0.1
8	0.0	0.2	0.2	0.5	0.4	0.3	0.2	0.1	0.1	0.1	0.0	0.0	0.0	0.0	0.0
8.5	0.0	0.1	0.2	0.2	0.2	0.1	0.1	0.1	0.0	0.0	0.0	0.0	0.0	0.0	0.0
9	0.2	0.1	0.1	0.1	0.2	0.0	0.1	0.0	0.0	0.0	0.0	0.1	0.0	0.0	0.0
9.5	0.1	0.0	0.1	0.0	0.1	0.0	0.0	0.0	0.0	0.0	0.0	0.0	0.1	0.0	0.0
10	0.1	0.1	0.0	0.0	0.0	0.0	0.1	0.0	0.1	0.1	0.1	0.0	0.0	0.1	0.0
10.5	0.1	0.0	0.0	0.0	0.0	0.0	0.0	0.0	0.0	0.0	0.0	0.0	0.0	0.0	0.0

Table E.1: Yearly wave scatter of the Borssele field, values are in percentage

E.2. Operability tables

In this section the operability tables for $\mu = 45°$ to $\mu = 135°$ are given with intervals of 15°.

$\mathbf{T_p[s]/H_s[m]}$	0.2	0.3	0.4	0.5	0.6	0.7	0.8	0.9	1.0	1.1	1.2	1.3	1.4	1.5
4														
4.5														
5														
5.5														
6														
6.5														
7														
7.5														
8												x	x	x
8.5											x	x	x	x
9											x	x	x	x
9.5													x	x
10														x

Table E.2: Operability table $\mu = 45°$. Light grey represents sea states at which the operability limit is exceeded for the DP model. Dark gray represents the 3DP model

$\mathbf{T_p[s]/H_s[m]}$	0.2	0.3	0.4	0.5	0.6	0.7	0.8	0.9	1.0	1.1	1.2	1.3	1.4	1.5
4														
4.5														
5														
5.5														
6														
6.5														x
7										x	x	x	x	x
7.5							x	x	x	x	x	x	x	x
8					x	x	x	x	x	x	x	x	x	x
8.5					x	x	x	x	x	x	x	x	x	x
9					x	x	x	x	x	x	x	x	x	x
9.5						x	x	x	x	x	x	x	x	x
10							x	x	x	x	x	x	x	x

Table E.3: Operability table $\mu = 60°$. Light grey represents sea states at which the operability limit is exceeded for the DP model. Dark gray represents the 3DP model

$\mathbf{T_p[s]/H_s[m]}$	0.2	0.3	0.4	0.5	0.6	0.7	0.8	0.9	1.0	1.1	1.2	1.3	1.4	1.5
4														
4.5														
5														
5.5														
6														
6.5										x	x	x	x	x
7							x	x	x	x	x	x	x	x
7.5					x	x	x	x	x	x	x	x	x	x
8				x	x	x	x	x	x	x	x	x	x	x
8.5				x	x	x	x	x	x	x	x	x	x	x
9				x	x	x	x	x	x	x	x	x	x	x
9.5					x	x	x	x	x	x	x	x	x	x
10					x	x	x	x	x	x	x	x	x	x

Table E.4: Operability table $\mu = 75°$. Light grey represents sea states at which the operability limit is exceeded for the DP model. Dark gray represents the 3DP model

$\mathbf{T_p[s]/H_s[m]}$	0.2	0.3	0.4	0.5	0.6	0.7	0.8	0.9	1.0	1.1	1.2	1.3	1.4	1.5
4														
4.5														
5														
5.5														
6													x	x
6.5									x	x	x	x	x	x
7						x	x	x	x	x	x	x	x	x
7.5				x	x	x	x	x	x	x	x	x	x	x
8			x	x	x	x	x	x	x	x	x	x	x	x
8.5			x	x	x	x	x	x	x	x	x	x	x	x
9			x	x	x	x	x	x	x	x	x	x	x	x
9.5				x	x	x	x	x	x	x	x	x	x	x
10				x	x	x	x	x	x	x	x	x	x	x

Table E.5: Operability table $\mu = 105°$. Light grey represents sea states at which the operability limit is exceeded for the DP model. Dark gray represents the 3DP model

$\mathbf{T_p[s]/H_s[m]}$	0.2	0.3	0.4	0.5	0.6	0.7	0.8	0.9	1.0	1.1	1.2	1.3	1.4	1.5
4														
4.5														
5														
5.5														
6														
6.5													x	x
7									x	x	x	x	x	x
7.5						x	x	x	x	x	x	x	x	x
8					x	x	x	x	x	x	x	x	x	x
8.5				x	x	x	x	x	x	x	x	x	x	x
9					x	x	x	x	x	x	x	x	x	x
9.5					x	x	x	x	x	x	x	x	x	x
10							x	x	x	x	x	x	x	x

Table E.6: Operability table $\mu = 120°$. Light grey represents sea states at which the operability limit is exceeded for the DP model. Dark gray represents the 3DP model

$\mathbf{T_p[s]/H_s[m]}$	0.2	0.3	0.4	0.5	0.6	0.7	0.8	0.9	1.0	1.1	1.2	1.3	1.4	1.5
4														
4.5														
5														
5.5														
6														
6.5														
7														
7.5												x	x	x
8									x	x	x	x	x	x
8.5								x	x	x	x	x	x	x
9									x	x	x	x	x	x
9.5										x	x	x	x	x
10											x	x	x	x

Table E.7: Operability table $\mu = 135°$. Light grey represents sea states at which the operability limit is exceeded for the DP model. Dark gray represents the 3DP model

F

Appendix

A commonly used method to passively damp the roll motion of a vessel is fitting bilge keels at the bilge radius of the vessel. To be able to quantify and compare the roll reduction resulting from fitting bilge keels at the *Ndurance*, a short study is carried out. It is assumed that the bilge keels are fitted on both sides of the vessel over a length of 54 meters, where $C_M = 0.99$. The bilge keel width is assumed 0.3 meters. A visualization of the bilge keel configuration at the starboard side of the vessel is given in Figure F.1.

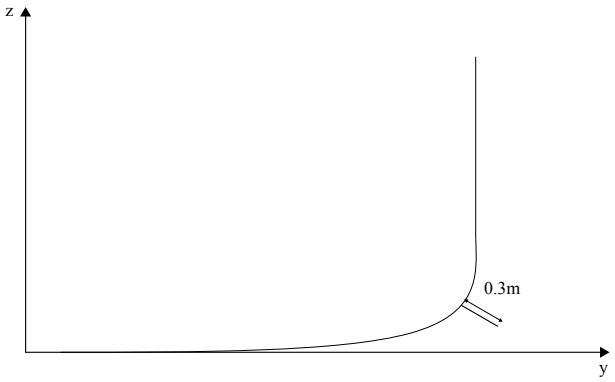

Figure F.1: Schematic visualization of bilge keel fitted at section

F.1. Empirical bilge keel damping model

According Chakrabarti [5], the viscous bilge keel damping consist out of two components. These components are damping terms due to the normal and hull pressure induced by the presence of the bilge keels:

$$B_{BK} = B_{BKN} + B_{BKH} \tag{F.1}$$

Bilge keel normal pressure damping
The normal component per unit length is defined by:

$$B_{BKN} = \frac{8}{3\pi}\rho r_{cb}^3 b_{bk}\omega R_0 f^2 C_D \tag{F.2}$$

ρ = sea water density
R_0 = roll motion amplitude
ω = wave frequency
b_{bk} = bilge keel width

The equivalent drag coefficient C_D is defined by:

$$C_D = 22.5\frac{b_{bk}}{\pi r_{cb} R_0 f} + 2.4 \tag{F.3}$$

where the factor f is included to account for the flow speed at the bilge keel. It is defined by:

$$f = 1 + 0.3\exp(-160(1-\sigma)) \tag{F.4}$$

where σ represents the area coefficient of a cross-section of the hull. The mean distance from the roll axis to the bilge keel r_{cb} is defined by:

$$r_{cb} = D((H_0 - 0.293R_b/D)^2 + (1 - OG/D - 0.293R_b/D)^2)^{0.5} \tag{F.5}$$

where

D	=	vessel draft
R_b	=	bilge radius
H_0	=	half the beam-draft ratio
OG	=	vertical distance from SWL to COG

Bilge keel hull pressure damping
The pressure damping component due to the hull surface is defined by:

$$B_{BKH} = \frac{4}{3\pi}\rho r_{cb}^2 D^2 \omega R_0 f^2 \left(-\left(-22.5\frac{b_{bk}}{\pi r_{cb} f R_0} - 1.2 \right) A_2 + 1.2B_2 \right) \tag{F.6}$$

where A_2 and B_2 are defined by:

$$A_2 = (m_3 + m_4)m_8 - m_7^2 \tag{F.7}$$

$$B_2 = \frac{m_4^2}{3(H_0 - 0.215m_1)} + \frac{(1-m_1)^2(2m_3 - m_2)}{6(1-0.215m_1)} + (m_3 m_5 + m_4 m_6)m_1 \tag{F.8}$$

The m-coeffients are given by:

$$m_1 = R_b/D \tag{F.9}$$

$$m_2 = OG/D \tag{F.10}$$

$$m3 = 1 - m_1 - m_2 \tag{F.11}$$

$$m_4 = H_0 - m_1 \tag{F.12}$$

$$m_5 = \frac{0.414H_0 + 0.0651m_1^2 - (0.382H_0 + 0.0106)m_1}{(H_0 - 0.215m_1)(1 - 0.215m_1)} \tag{F.13}$$

$$m_6 = \frac{0.414H_0 + 0.0651m_1^2 - (0.382 + 0.0106H_0)m_1}{(H_0 - 0.215m_1)(1 - 0.215m_1)} \tag{F.14}$$

$$m_7 = S_0/D - 0.25\pi m_1 \tag{F.15}$$

$$m_8 = m_7 + 0.414m_1 \tag{F.16}$$

where S_0 is defined by:

$$S_0 = 0.3\pi f r_{cb} R_0 + 1.95 b_{bk} \tag{F.17}$$

F.2. Bilge keel model implementation

The damping coefficients are calculated by using the roll motion amplitude estimates of the frequency domain model without the implementation of a viscous damping term. Subsequently, the viscous damping coefficients are calculated and implemented in the frequency domain model:

$$[\mathbf{M} + \mathbf{A}(\omega)]\ddot{\eta} + \mathbf{B}(\omega)\dot{\eta} + B_{eq}\dot{\phi} + \mathbf{C}\eta = \mathbf{F}(\omega)\cos(\omega t + \epsilon) \tag{F.18}$$

where B_{eq} is now defined by:

$$B_{eq} = B_e + B_f + B_{BK} \tag{F.19}$$

where B_e and B_f represent the eddy making and skin friction damping respectively. A similar iterative approach as described in Chapter 2 is used to obtain the converged viscous roll damping values.

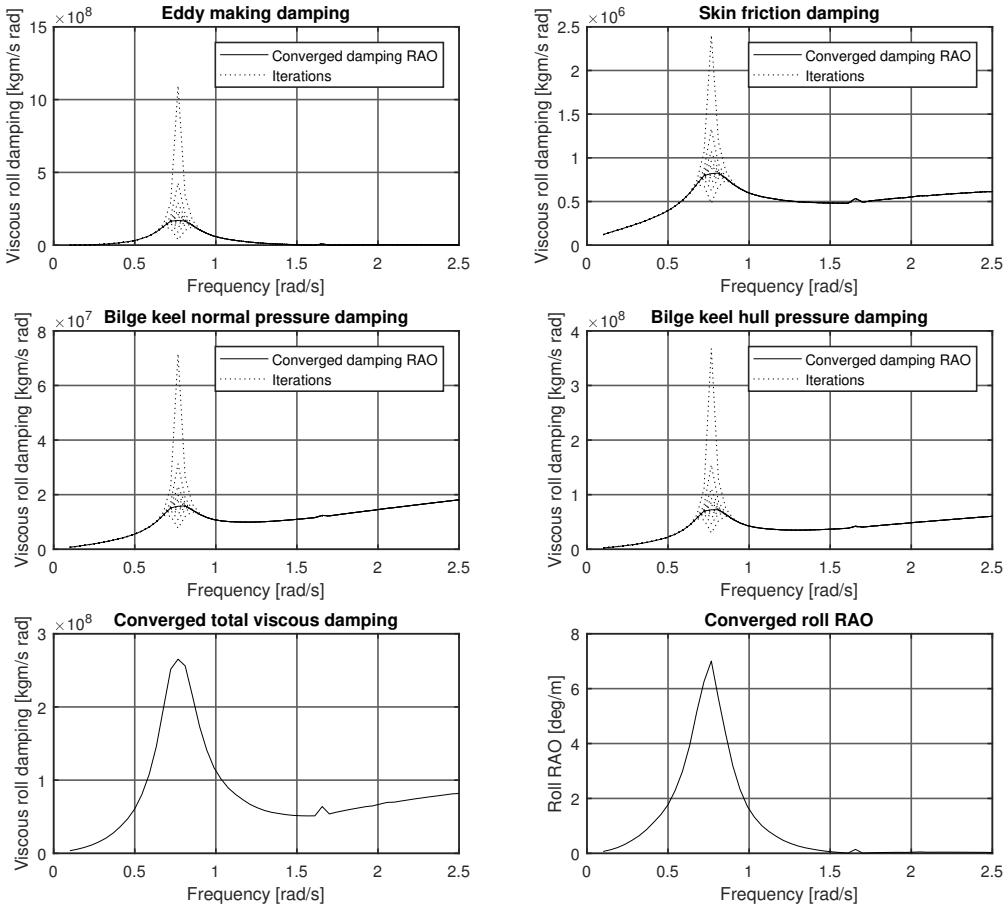

Figure F.2: Results of iterative calculation of viscous damping RAO's with bilge keel damping included and final roll motion RAO in the frequency domain model ($\mu = 90°$, T=4.7m, WD=1000m)

The results of the iterative procedure are visualized in Figure F.2.

In the time domain model the viscous damping term is included by a quadratic viscous damping term. This is considered a more physical approach, since it is known that drag forces have a quadratic relation with velocity, see for example Chakrabarti [5]. The quadratic viscous damping term is defined by:

$$B_{visc} = c_1|\dot{\phi}|\dot{\phi} \tag{F.20}$$

where c_1 is a fitting parameter. The value of this fitting parameter is obtained by fitting the time domain roll motion RAO to the frequency domain roll motion RAO with a linearized viscous roll damping term included. The time domain model with a viscous roll damping term included is now defined by:

$$[\mathbf{M} + \mathbf{A}_\infty]\ddot{\eta} + \mathbf{K}_{ss}\dot{\eta} + c_1|\dot{\phi}|\dot{\phi} + \mathbf{C}\eta = F(t) \tag{F.21}$$

By adjusting the value of c_1, the time domain roll motion RAO is fitted to the frequency domain roll motion RAO. The result is visualized in Figure F.3
The value of the tuning parameter is determined as $c_1 = 3.5 \cdot 10^9$. As can be derived from Figure F.3, the time and frequency domain model results match.

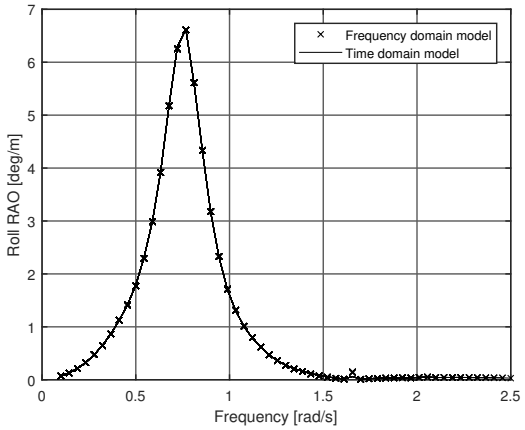

Figure F.3: Results of time domain model RAO fitting to frequency domain RAO with bilge keel damping included ($\mu = 90°$, T=4.7m, WD=1000m)

F.3. Bilge keel model results

The RMS of the roll motion amplitudes for different wave periods and wave heights are calculated when the bilge keels are applied. The result is given in Figure F.4. To enable comparison with the 3DP model and DP model, both results are also displayed in Figure F.4.

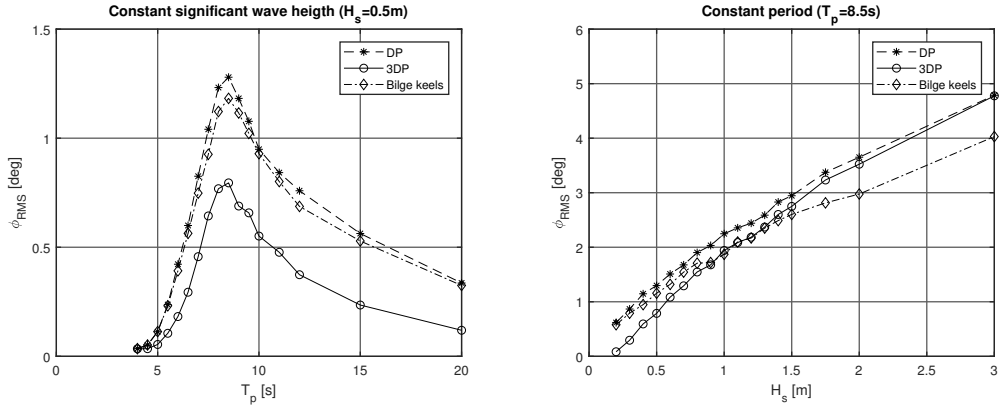

Figure F.4: Roll angle RMS as a function of wave period and significant wave height for both control models and when bilge keels are applied

From the results visualized in Figure F.4 can be observed that the relative roll reduction, at the roll natural frequency, realized by the 3DP is a factor 4 bigger compared to the roll reduction when the bilge keels are applied. It is also concluded that roll reduction by the bilge keels is more significant for wave heights greater than 1.5m. This can be explained by the increased roll velocities during these relative high sea states.

From this study is concluded that fitting bilge keels on the *Ndurance* reduces the roll motion amplitudes with a maximum of 10%, whereas the 3DP control model is able to realize a roll reduction of 40%. The bilge keel induced relative roll reduction increases to 15% for sea states exceeding significant wave heights of 1.5 meter.

List of Figures

List of Tables

Bibliography

[1] Jose A. Armesto, Raul Guanche, Fernando del Jesus, Arantza Iturrioz, and Inigo J. Losada. Comparative analysis of the methods to compute the radiation term in cummins' equation. *Ocean Engineering and Marine Energy*, 1:377–393, 2015.

[2] J. Bargmeyer. *Wetenswaardigheden over frequentieomvormers*. Danfoss, Nordborg, 2016.

[3] R.H. Byrd et al. A trust region method based on interior point techniques for nonlinear programming. *Mathematical Programming*, 89(1):149–185, 2000.

[4] O. Cadet. Introduction to kalman filter and its use in dynamic positioning systems. In *MTS Dynamic Positioning Conference September 16-17*, 2003.

[5] Subrata Chakrabarti. Empirical calculation of roll damping for ships and barges. *Ocean Engineering*, 28:915–932, 2001.

[6] J.G. Cooke. *Incorporating Thruster Dynamics in the Control of an Underwater Vehicle*. MIT, 1989.

[7] W.E. Cummins. The impulse response function and ship motions. In *Symposium Ship Theory Hamburg, Germany*, 1962.

[8] G. de Backer. *Hydrodynamic design optimization of wave energy converters consisting of heaving point absorbers*. PhD thesis, Ghent University, 2009.

[9] DNV-GL. St-0111 assessment of station keeping capability of dynamic positioning vessels. DNV-GL Standard, 2016.

[10] T. Duarte. *SS Fitting - Theory and user manual*. NWTC, 2012.

[11] T.I. Fossen. *Handbook of Marine Craft Hydrodynamics and Motion Control*. Wiley & Sons Ltd., Sussex, 2011.

[12] R. Habing. *Roll damping to improve the operational limits of existing barge-shaped vessels*. TU Delft, Delft, 2016.

[13] H. Hatecke. Robust identification of parametric radiation force models via impulse response fitting. *Proceedings in Applied Mathematics and Mechanics*, 15(1):593–594.

[14] Y. Himeno. Prediction of ship roll damping - state of the art. University of Michigan, 1981.

[15] Y. Ikeda, T. Fujiwara, and T.Katayama. Roll damping of a sharp-cornered barge and roll control by a new-type stabilizer. In *Proceedings of the Third International Offshore and Polar Engineering Conference, Singapore*, 1993.

[16] J.M.J. Journée. Hydromechanic coefficients for calculating time domain motions of cutter suction dredgers by cummins equation, 2000.

[17] Philipp Koschorrek et al. Dynamic positioning with active roll reduction using voith schneider propeller. In *10th IFAC Conference on Manoeuvring and Control of Marine Craft*, 2015.

[18] W. Leonhard. *Control of Electrical Drives 2nd edition*. Springer-Verlag, Berlin, 1996.

[19] Donald M. MacPherson, Vincent R. Puleo, and Matthew B. Packard. Estimation of entrained water added mass properties for vibration analysis. SNAME New England section, 2007.

[20] J.M.J. Journée & W.W. Massie. *Offshore Hydromechanics*. Delft University of Technology, Delft, 2001.

[21] J.N. Newman. *Marine Hydrodynamics*. MIT, Massachusetts, 1977.

[22] M.W.C. Oosterveld. *Wake Adapted ducted propellers*. PhD thesis, Delft University of Technology, Delft, 1970.

[23] Orcina. Orcaflex documentation. *https://www.orcina.com/SoftwareProducts/OrcaFlex/Documentation*, 2018.

[24] T. Perez. Parametric time-domain models based on frequency domain data, 2007.

[25] T. Perez. Practical aspects of frequency-domain identification of dynamic models of marine structures from hydrodynamic data. *Ocean Engineering*, 38(1):426–435, 2011.

[26] Ivan Pinéda. *The European offshore wind industry - key trends and statistics 2015*. EWEA, Brussel, 2015.

[27] P. Rici et al. Time-domain models and wave energy converters performance assessment. In *27th ASME Conference on Ocean, Offshore and Arctic Engineering OMAE2008*, 2008.

[28] Sigbørn Eng Rudaa. Use of tunnel thrusters and azimuthing thrusters for roll damping of ships, 2016.

[29] H.E. Saunders. *Hydrodynamics in Ship Design*. The Society of Naval Architects and Marine Engineers, New York, 1957.

[30] H. Schwanecke. Gedanken zur frage der hydrodynamisch erregten schwingungen des propellers und der wellenleitung. Jahrbuch der Schiffbauteschnischen Gesellschaft 57. Band, 1963.

[31] Jorrit Jan Serraris. Time domain analysis for dp simulations. In *28th ASME Conference on Ocean, Offshore and Arctic Engineering OMAE2009*, 2009.

[32] Øyvind Notland Smogeli. *Control of marine propellers*. PhD thesis, NTNU, Trondheim, 2006.

[33] Asgeir J. Sørensen and Jann Peter Strand. Positioning of small-waterplane-area marine constructions with roll and pitch damping. *Control Engineering Practice*, 8:205–213, 2000.

[34] H. Klein Woud & D. Stapersma. *Design of Propulsion and Electric Power Generation Systems*. IMAREST, London, 2002.

[35] Johan Wichers, Stephen Bultema, and Richard Matten. Hydrodynamic research on and optimizing dynamic positioning system of a deep water drilling vessel. In *Offshore Technology Conference*, 1996.

[36] Shengwen Xu et al. Mitigating roll-pitch motion by a novel controller in dynamic positioning system for marine vessels. *Ships and offshore structures*, 12:1136–1144, 2017.